Novel Handheld Sensors for In-Vivo Soft Tissue Tension Measurement during Orthopedic Surgery

A DISSERTATION
SUBMITTED TO THE FACULTY OF THE GRADUATE SCHOOL
OF THE UNIVERSITY OF MINNESOTA
BY

Kalpesh Singal

IN PARTIAL FULFILLMENT OF THE REQUIREMENTS
FOR THE DEGREE OF
DOCTOR OF PHILOSOPHY

Professor Rajesh Rajamani

December 2013

Acknowledgements

My journey as a graduate student at University of Minnesota has been an amazing and satisfying one. During this journey I have met some truly creative and smart people who have helped shape and guide me as a researcher on my path to a doctorate.

First and foremost, I would like to thank Dr. Rajesh Rajamani, my advisor, for his continual guidance and encouragement during my doctoral studies. He has helped me transition from a timid undergraduate to a confident researcher. The success of this project owes a lot to his patience, knowledge, support and enthusiasm. I feel immensely lucky and deeply honored to have him as my advisor.

I would also like to thank Dr. Joan Bechtold for her help identifying the unmet needs in the field of orthopaedic surgeries that this project has tried to address. In addition to Dr. Bechtold, I would like to thank Dr. Curtis Goreham-Voss and Andrew Freeman at Excelen Center for Bone & Joint Research and Education for their help and support in procuring the biological specimens for use during this study.

I am also grateful to Dr. Arthur Erdman and Dr. Snigdhansu Chatterjee for taking time out of their otherwise busy schedule to serve on my thesis committee. Their insightful observations have helped me improve the research described in this thesis.

I would like to thank Lee Alexander for his help and resourcefulness. He was always the go to person for all my design needs and has helped me design and fabricate a lot of fixtures used as a part of this project. I would also like to thank Dr. A. Serdar Sezen for taking time out of his busy schedule to provide me valuable guidance during the project.

I am thankful to all my labmates: Dr. Gurkan Erdogan, Dr. Shyam Sivaramakrishnan, Dr. Krishna Vijayaraghavan, Dr. Gridsada Phanomchoeng, Dr. Peng Peng, Shan Hu, Saber Taghvaeeyan, Garrett Nelson, Mahdi Ahmadi, Sean Pruden, Matthew Hildebrand and Song Zhang, for spending endless hours working together in the lab and helping me during different phases of my doctoral study. It was a truly pleasure working with you all. I would like to especially thank Dr. Peng Peng for the guidance he provided during the

initial phase of my doctoral studies and to Garrett and Mahdi for the countless discussions we had on various topics both related and unrelated to my research.

Last but not least, I would like to thank all my friends and especially my two roommates: Saurabh Tewari and Anupam Srivastava, for making my stay in Minneapolis a memorable one.

Abstract

This thesis focuses on the development of handheld sensors for *in vivo* measurement of soft tissue tension. The sensors will aid the surgeon in balancing forces in soft tissues during total knee arthroplasty, ACL repair, hip replacement surgeries, shoulder stabilization and other orthopaedic procedures by providing real-time measures of tension in soft tissue. The proposed method utilizes the application of an unknown transverse force on the soft tissue using a handheld probe. An array of miniature sensors on the probe is used to measure the resulting curvature of the soft tissue and tissue tension is estimated from this measurement.

The first generation sensor developed in the project utilized capacitive sensing units to measure the forces required to displace the ligament by a fixed amount determined by the pattern of bumps in the sensor. These force values were used to estimate the tension in the ligament. The sensing concept was experimentally demonstrated; however it was not found to be suitable for hand held applications due to restrictions involved with the point of the contact along the ligament and also due to unreliability associated with estimates in the presence of noise.

A second generation sensor design was developed to estimate the tension from displacements of three points on the sensor under three transverse loads. A sensor was fabricated using soft rubber bumps. The sensor works reasonably well for controlled orientations; however it is not suitable for hand held applications due to its sensitivity to orientation errors. Several challenges related to micro-fabrication also cause imperfections in the sensor and introduce variability in the results.

The third generation sensor utilized changes in magnetic field to measure the displacements and curvature of the soft tissue. Linear coil springs were used in the sensor to ensure accurate calculation of forces from force-displacement relations. The design allowed for higher displacements within the sensor and hence was found to be significantly less sensitive to orientation errors as compared to the second generation sensor. The experimental results both during controlled orientations and handheld

operation show that the sensor can measure tension values up to 100 N with a resolution of 10 N or better. The feasibility of the sensor to measure tension in biological tissues is also demonstrated using experimental tests with a turkey tendon.

The developed magnetic sensor was also reconfigured for use in two other medical diagnosis applications. The sensor was able to measure tissue elasticity with five times better resolution and four times the range of other elasticity sensors previously proposed in the literature. The sensor could also be used to measure compartment pressure for non-invasive diagnosis of compartment syndrome. In-vitro results using both a pneumatic compartment and an agarose-gel compartment showed that the sensor could accurately measure compartment pressure and could be a non-invasive alternative to invasive catheter based measurements for diagnosing compartment syndrome.

Table of Contents

List of Tables

List of Figures

Citations of Published Work

Some portions of this thesis have appeared in the following publications:

1. K. Singal and R. Rajamani, "Handheld magnetic sensor for measurement of tension," Applied Physics Letters, vol. 100, pp. 154105, 9 April 2012, 2012.
2. K. Singal, P. Peng, R. Rajamani and J. E. Bechtold, "Measurement of Tension in a String Using an Array of Capacitive Force Sensors," IEEE Sensors, vol. 13, pp. 792-800, 2013.
3. K. Singal, P. Peng, R. Rajamani and J. E. Bechtold, "A handheld device for measurement of tension: An aide to surgeons for soft tissue balance during orthopedic surgeries," Proceedings of the 2012 ASME 5th Annual Dynamic Systems and Control Conference, Joint with the JSME 2012 11th Motion and Vibration Conference, DSCC 2012-MOVIC 2012, 2012, pp. 403-409.
4. C. Flegel, K. Singal and R. Rajamani, "A handheld noninvasive sensing method for the measurement of compartment pressures," Proceedings of the 2013 ASME 6th Annual Dynamic Systems and Control Conference, DSCC 2013, October 2013.
5. C. Flegel, K. Singal, R. Rajamani, and R. Odland, "Development and Experimental Validation of A Handheld Noninvasive Sensor for the Measurement of Compartment Pressures," accepted for publication in the ASME Journal of Medical Devices, 2013.

CHAPTER 1

INTRODUCTION

1.1 MOTIVATION

The importance of balancing tension in soft tissues during various orthopedic procedures like total knee arthroplasty (TKA) [1-4], hip replacement surgeries [5], anterior cruciate ligament (ACL) repair [6] and shoulder stabilization [7, 8] has been well established. In these procedures, the surgeon has to not only handle and manipulate the bone but also the surrounding soft tissue, including muscle, fascia, tendon, ligament and capsule. Successful handling of these tissues and balancing of tensile forces in them is often the key to high reproducibility, good soft tissue healing, restoration of overall limb function in the patient, and a long lasting implant [1, 2, 5].

1.1.1 Total Knee Arthroplasty

Total knee arthroplasty (TKA) is a well-established procedure for restoring knee function in patients who suffer from degenerative disease of the knee joint. 402,000 primary TKAs were performed in the US alone in the year 2003 [9]. This number is expected to see an over 8 times increase in the next two decades, with the projections for 2030 predicted to be as high as 3.48 million procedures a year [9].

The anatomy of a human knee is shown in Figure 1-1. During the TKA surgery the surgeon not only has to deal with bone but also with the surrounding soft tissue. Several

complications that occur after TKA, such as misalignment, instability [10] and loosening, have been attributed to poor soft tissue balance.

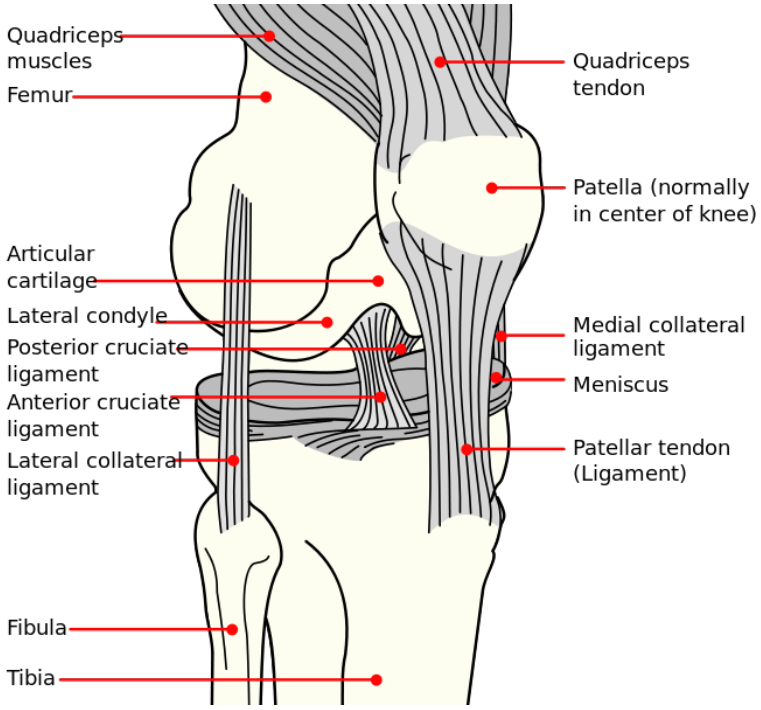

Figure 1-1: Anatomy of human knee

Even though many studies have been published attempting to improve the understanding of this part of the procedure and a few devices have been developed for assisting intraoperatively with soft tissue balancing, they have not been widely used and the soft tissue balancing still largely depends on the surgeon's subjective "feel" during surgery [1-4]. Studies show that conventional surgical techniques fail to restore neutral mechanical alignment in up to 30% of the cases [11-13] with a recent meta-analysis estimating the rate of misalignment in conventional TKA patients to be 31.8% [14].

Major deterring factors that prevent the widespread use of the devices developed for measuring tension in the past are cost, reliability or complexity involved [2, 15]. An inexpensive and easy-to-use device for measuring the tension in the soft tissues around the knee would not only help the surgeons in obtaining proper soft tissue balance during

TKA, potentially increase the survivorship of TKA; but would also serve as a useful tool for the instruction of orthopaedic residents in TKA surgical techniques.

1.1.2 Hip Replacement Implants

Over 200,000 Americans underwent hip replacement surgery in the year 2003 which is expected to grow to 570,000 in year 2030 [9]. The tension in the abductor muscles keeps the hip implant in position. The ability to measure the tension in the abductor muscles during surgery can quantify how securely the joint is established with the new hip implant and can significantly help improve surgical outcomes. Controlling the tensile forces in the abductor muscles would ensure that the hip prosthesis is in balance and has the right amount of normal force to prevent both hip dislocation as well as uneven gait [5].

1.1.3 ACL Injuries

Injuries to the anterior cruciate ligament (ACL) are one of the most commonly occurring sports-related knee ligament injuries, and more than 50,000 ACL reconstruction procedures are performed annually in the US [16]. Intraoperative control of tension in the ligament graft can dictate its eventual proper function [6]. If the ligament graft is fixed under a level of tension that is too low, postoperative instability with possible cartilage degeneration will result. If the ligament graft is fixed under a level of tension that is too high, reduced range of motion and possible ligament graft rupture or stretching may occur.

1.1.4 Shoulder Stabilization

The shoulder is the most frequently dislocated joint in the human body, especially in the younger population, and more than half of these patients will progress to recurrent episodes of symptomatic global instability. The main treatment for shoulder stabilization is reattachment or reefing (advancement of loose or attenuated tissue to tighten it) of the loose glenohumeral capsule and ligament complex [8, 17-19]. Insufficient tension in this capsule-ligament complex from surgery can be associated with recurrence of instability

episodes [7, 8, 20], whereas tighter than normal tension can lead to limited of range of motion and abnormal loading with subsequent arthritic changes [17, 18].

1.2 EXISTING MEASUREMENT TECHNOLOGIES

The existing transducers for in-situ measurement of soft tissue tension require significant dissection and handling of the tissue [21-23], making them infeasible for use during actual surgeries.

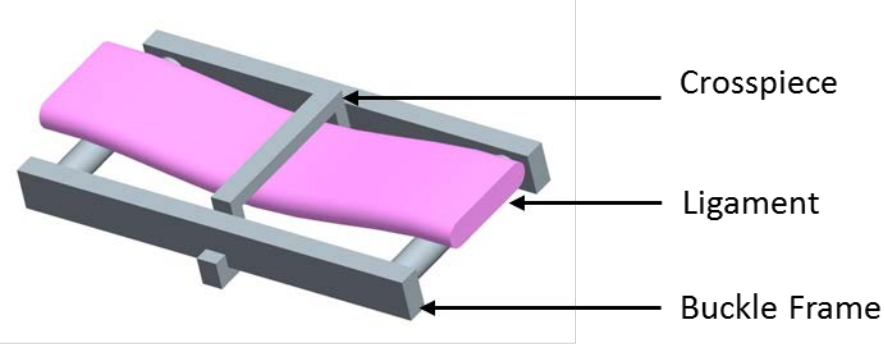

Figure 1-2: Buckle Transducer

The buckle transducer proposed by Salmons [24] in 1969 was one of the first devices to measure in vivo force measurement in animal tendons. It is one of the widely used transducers for research and has undergone several modifications to adapt it for ease of use. The measurement process involves drawing a loop of ligament through a rectangular frame and securing it in place using a rectangular crossbar as shown in Figure 1-2, resulting in an appearance similar to a buckle. The transducer works by measuring the deflection in the frame due to three point bending caused by its interaction with the ligament. The obtrusive shape of the transducer precludes its use in actual surgical applications [25]. The presence of buckle transducer causes a shortening in length and causes change in local stress at the site at which it is attached.

The liquid metal strain gauge (LMSG) [26, 27] is a mercury (or mixture of indium and gallium [28]) filled compliant capillary tube incorporated into electrical wire. The electrical resistance of this tube changes as a function of the applied strain, which is used

to indirectly calculate the tension. The gauge is attached to the ligament, as shown in Figure 1-3, by either using contact cement or by suturing the lead wires of the gauge to ligament itself [29]. Apart for involving significant amount of tissue handling and the need to attach the LSMG to the ligament itself, LSMGs are sensitive to temperature and present a risk of release of toxic substances [28, 29].

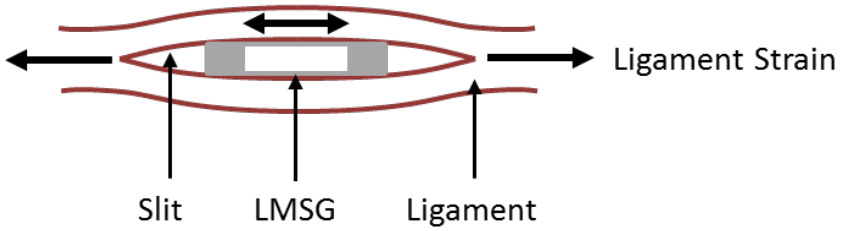

Figure 1-3: Liquid metal strain gauge

Several other devices have been proposed that employ Hall Effect transducers [21], implantable force transducers [30] or optic fibers [31] to measure strain or force in the ligament. However all of these devices have to be implanted onto the ligament and hence involves considerable amount of tissue handling [21, 22].

Krystal et al. [32] presented a method for measuring tension in small ligaments based on measuring tension in an axially loaded string by deflecting it laterally and measuring the load and deformation. The sensor employed a linearly variable differential transformer (LVDT) to measure deformations and a load cell to measure force. The proposed device was tested by Kristal et al. [32] and Weaver et al. [33] on small wrist ligaments. The sensor required an inertial reference, making it unsuitable as a handheld device; moreover it involves estimating the free length of the ligament [29], which would require an extra measurement not usually available.

1.3 THESIS CONTRIBUTIONS

This dissertation focusses on developing handheld devices for medical diagnosis, with a focus on measuring tension in soft tissues like ligaments and tendons. Major contributions of this dissertation include:

1) Development of a theoretical model and sensing principle for estimating tension in ligaments without the need for any inertial measurement, thus enabling handheld measurement of tension.
2) Development of capacitive-sensing based miniature sensors for measuring tension in tissues.
3) Development of a magnetic-sensing based sensor which can be reliably used for measurements in a handheld mode.
4) Experimental validation to confirm that the developed devices can successfully measure tension in short synthetic strings and in soft biological tissues.
5) Reconfiguration and evaluation of the developed magnetic device as a feasible tool for soft tissue elasticity measurement and non-invasive compartment pressure measurement.

1.4 THESIS OUTLINE

Chapter 2 describes a single-probe capacitive sensor to measure the tension in the ligaments. This chapter develops a theoretical formulation to estimate the tension in the string by measuring the force required to cause a fixed displacement. This chapter also discusses the design and fabrication methodology for a sensor based upon the developed theoretical formulation and concludes with the experimental verification of the estimation method.

Chapter 3 develops an improved sensing method based on application of multiple forces to the string. The chapter develops a theoretical framework to relate the magnitudes of

the three forces applied at locations whose positions relative to each other are known. The chapter also describes a capacitive sensing based sensor which was designed and fabricated to experimentally prove the developed theoretical framework. Compared to the single-probe capacitive sensor, the estimates from this sensor are based on a large number of observations and hence are relatively less prone to measurement noise.

Chapter 4 further develops the sensing methodology described in chapter 3 and describes a magnetic sensing based sensor. The magnetic sensor provides distinct advantages of being resilient to proximity noise, utilizing a more reliable fabrication method and having a better resolution over the capacitive based technique. The chapter presents extensive modeling of the sensor and presents both theoretical and experimental sensitivity analysis. It is further shown in this chapter that the sensor can measure tension with a resolution better than 10 N, and is a viable handheld tool for measuring tension in strings.

Chapter 5 discusses potential application of the multi-probe magnetic sensors for measuring quantities other than tension in a string. This chapter discusses two such variables - the elasticity of a soft material and pressure inside a compartment - and provides experimental results on measurements of both.

CHAPTER 2

SINGLE-PROBE CAPACITIVE SENSOR

2.1 THEORETICAL MODEL AND SENSOR DESIGN

The single-probe capacitive sensor was designed to measure tension by applying a single point transverse force to the string and measuring the magnitude of force required to cause a fixed amount of deflection.

Figure 2-1 shows the sensing mechanism. When a force (F) is applied to a string (shown as dotted line) under tension (T), it causes the string to deform as illustrated by the solid line.

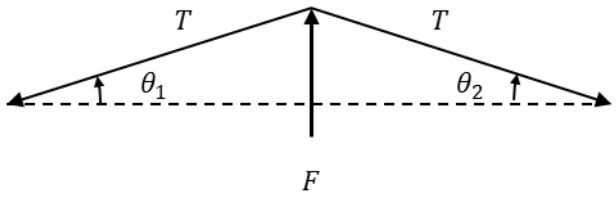

Figure 2-1: Sensing mechanism of the first generation sensor

The tension in the string as a function of F, θ_1 and θ_2 is given in equation (2.1)

$$T = F/(\sin(\theta_1) + \sin(\theta_2)) \tag{2.1}$$

Assuming that the force, F, acts at the midpoint of the string, and hence $\theta_1 = \theta_2 = \theta$, equation (2.1) can be written as equation (2.2).

$$T = \frac{F}{2\sin(\theta)} \tag{2.2}$$

The schematic of the first generation sensor is shown in Figure 2-2. The sensor consists of three cylinders, referred to as bumps. The center bump is taller than the two side bumps. Assuming that the height difference is X, the distance between the center bump and either of the side bumps is d and that the bumps are rigid, the angle made by the string when the side bumps just come into contact is given by equation (2.3).

$$\tan(\theta) = X/d \tag{2.3}$$

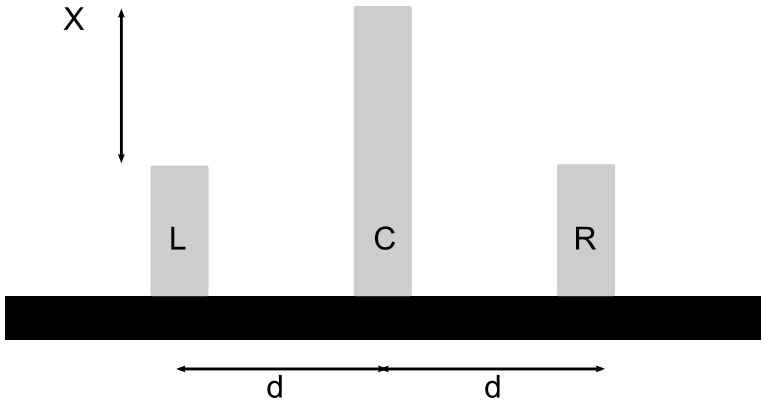

Figure 2-2: Schematic of the first generation sensor

During operation, the force (F) on the center bump is measured at the instant the two side bumps came into contact. The angle, θ, is known from design, hence the tension can be calculated using equation (2.2). The force under each of the bumps is measured using capacitive sensors that are placed under each of them.

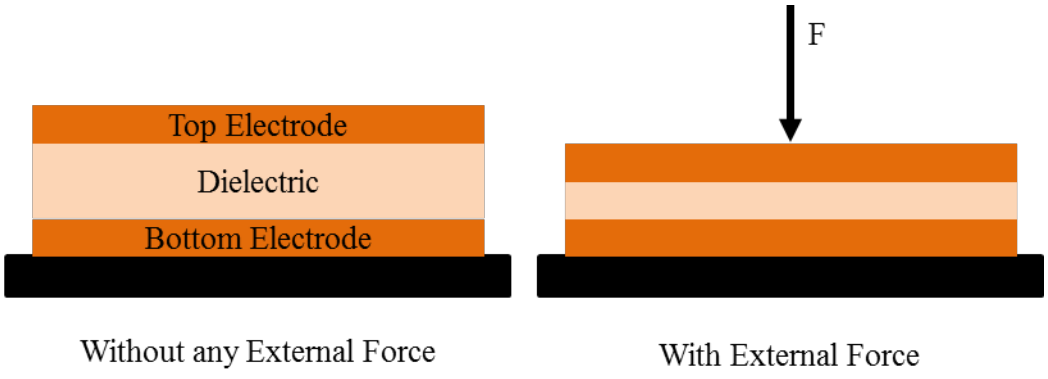

Figure 2-3: Principle of working of a capacitive sensor

Figure 2-3 shows the working mechanism of a capacitive sensor. A capacitive sensor consists of two electrodes, top electrode and bottom electrode, separated by a soft dielectric. The capacitance between the top and the bottom electrodes is given by equation (2.4).

$$C = \epsilon A/d \tag{2.4}$$

where ϵ is the dielectric constant for the dielectric material, A is the area of the electrodes and d is the separation between the two electrodes.

When a force is applied to the sensor, the dielectric deforms and the separation between the two electrodes decreases causing an increase in the capacitance. The change in capacitance is measured and is used to estimate the force.

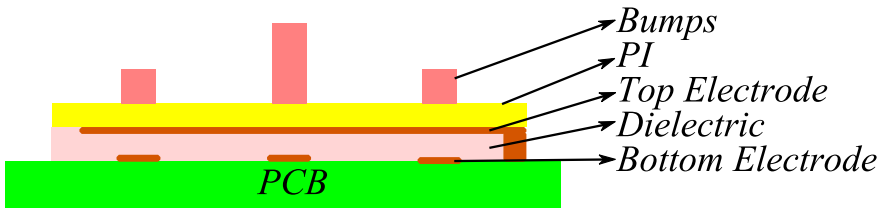

Figure 2-4: Cross sectional view of the sensor

A sensor was designed to realize the above sensing concept. Figure 2-4 shows a cross sectional view of the designed sensor. The sensor consists of two sets of electrodes; top

and bottom. The bottom electrodes were designed on a printed circuit board (PCB). The top electrodes were fabricated on a flexible copper clad polyimide (PI) layer (DuPontTM Pyralux® AC 182500R). The bumps were fabricated by molding urethane rubber compound (PMC-746, Smooth-On Inc.) into small cylinders. The shore hardness of the rubber was 60A which corresponds to a Young's modulus of approximately 3.5Mpa. A softer urethane rubber compound (PMC-724, Smooth-On Inc.) was used as the dielectric layer for the capacitor. The shore hardness of the dielectric material was 40A which corresponds to a Young's modulus of approximately 1.5Mpa.

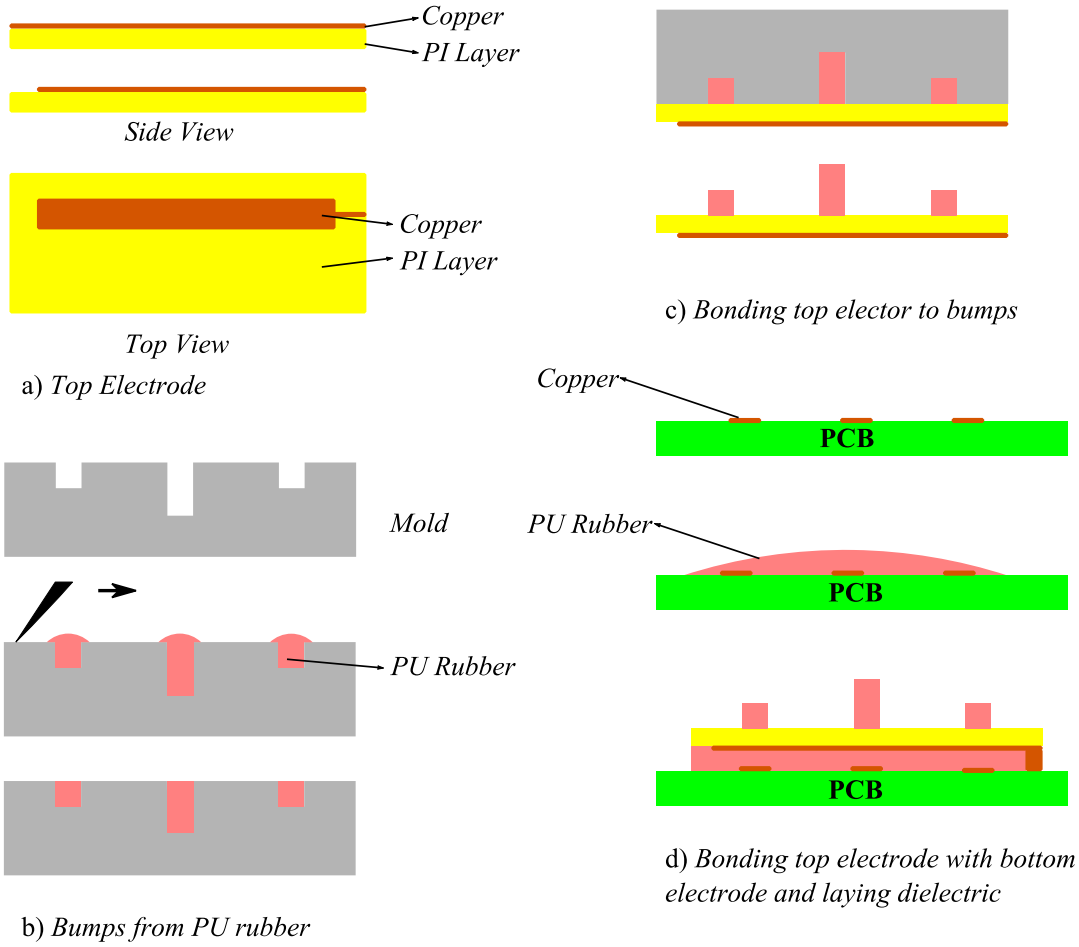

Figure 2-5: Fabrication process for the sensor

Figure 2-5 shows the steps required to fabricate the sensor. Each of the steps involved in the fabrication sequence is explained below:

2.1.1 Bottom electrode

Bottom electrodes are designed and fabricated on a printed circuit board (PCB).

2.1.2 Top electrode

A substrate of copper clad polyimide (PI) layer is taken, and electrode areas are masked on the copper using Kapton tape. The unwanted copper is then wet etched to get the desired pattern of top electrode.

2.1.3 Bumps

A mold is fabricated by drilling accurate holes in an acrylic sheet. The diameter of the holes was chosen to be 2 mm and the depth as 1.5 mm for the center bump and 1 mm for the side bumps. The center to center distance between the two adjacent holes is fixed to 3 mm. Urethane rubber is then filled in the three holes and the excess rubber is removed by using a blade as squeegee.

2.1.4 Bonding the top electrode to bumps

Within 30 minutes of filling the rubber, the mold is placed on top of the PI layer with top electrode so that the bumps are aligned with the patterned electrode. The mold is left undisturbed overnight to let the bumps cure on top of the PI layer. The PI layer then is peeled off the mold.

2.1.5 Bonding top and bottom electrode

A small amount of uncured urethane rubber was poured on the PCB. The top electrode and bottom electrodes were aligned and the setup was left undisturbed overnight for the rubber to cure. The top electrode was then soldered to the ground pad on the PCB.

A photograph of the sensor is shown in Figure 2-6. It can be seen that the side bumps are smaller in height than the center bump.

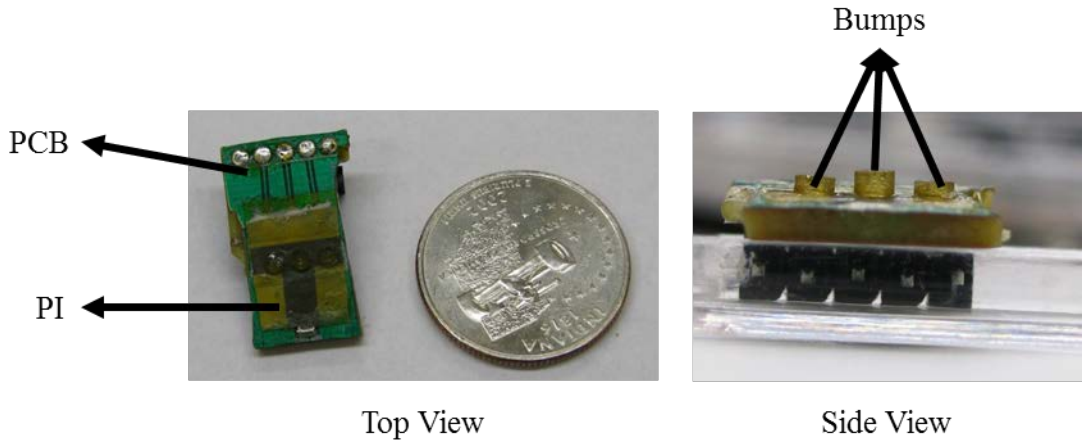

Figure 2-6: Photograph of the sensor

A 13 channel capacitance to digital conversion chip (AD7147) from Analog Devices is used to obtain the capacitance readout. Since the AD7147 can only communicate using either SPI or I2C protocol, the data from the chip is acquired using an Arduino Uno and transmitted in real time to a computer through serial port.

2.2 EXPERIMENTAL RESULTS

Each bump was first characterized to generate the force vs capacitance calibration curve for it. Figure 2-7 shows the schematic and photograph of the experimental setup. A force gauge of 5N range (Model HP-5 from Handpi TM) was mounted on a vertical test stand. The tip of the force gauge was used to apply known forces to the sensor and the sensor response was recorded. This process was repeated three times to test for the calibration repeatability.

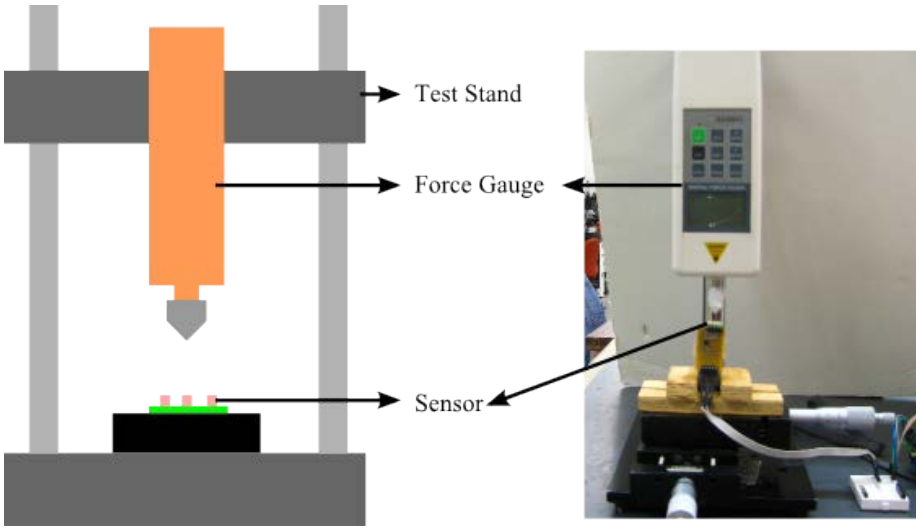

Figure 2-7: Schematic (left) and image (right) of the experimental setup used for characterizing the sensor

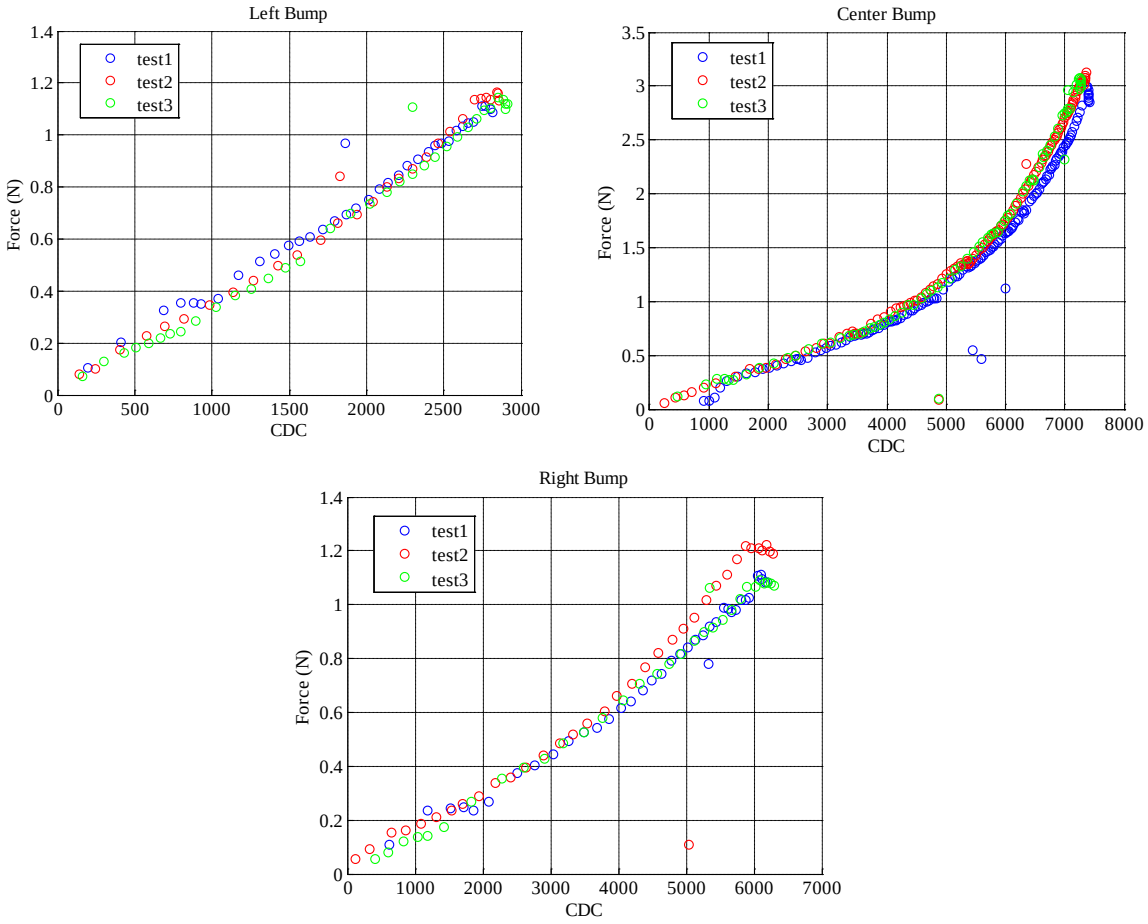

Figure 2-8: Calibration curves for the three bumps of the first generation sensor

Figure 2-8 shows the calibration curves for the three bumps. The tests were found to be repeatable for each of the bumps.

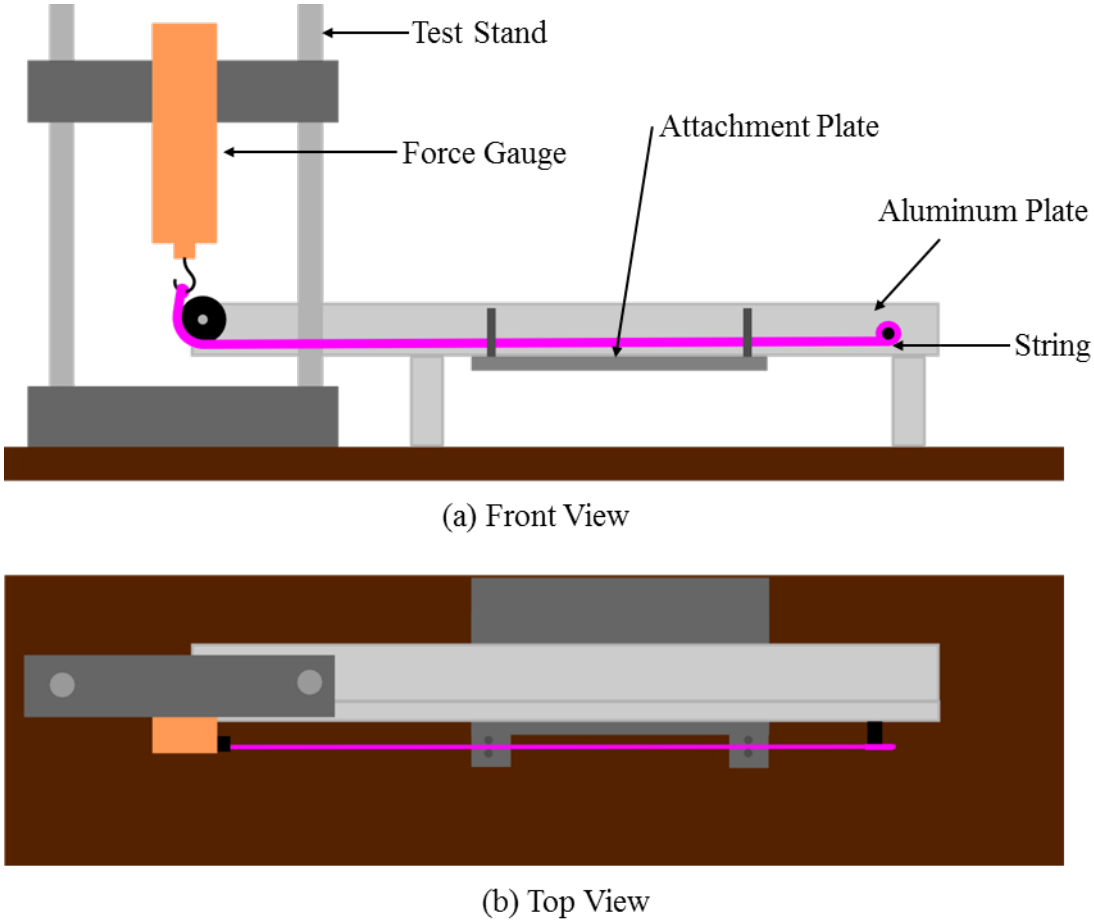

Figure 2-9: Schematic of the experimental setup for evaluating the sensor performance

An experimental setup was designed to apply known tensions to a nylon lace. Figure 2-9 shows the schematic of the setup which was used to test the sensor for known tension values. The setup consists of a force gauge of 200N range (HP-200 from Handpi TM) mounted on a vertical test stand. A flat nylon lace of width approx. 5mm is tied to one end of the setup and is routed through a pulley on the other side to the force gauge. The height of the test stand can be adjusted to change the tension in the lace. The sensor is fixed on a translation stage to control orientation. The photographs of the setup from two different views are shown in Figure 2-10. The sensor performance was evaluated at tensions between 20-120 N, which is the range of forces used by other studies [34, 35].

Five tests were conducted in quick succession at each tension value to evaluate the repeatability.

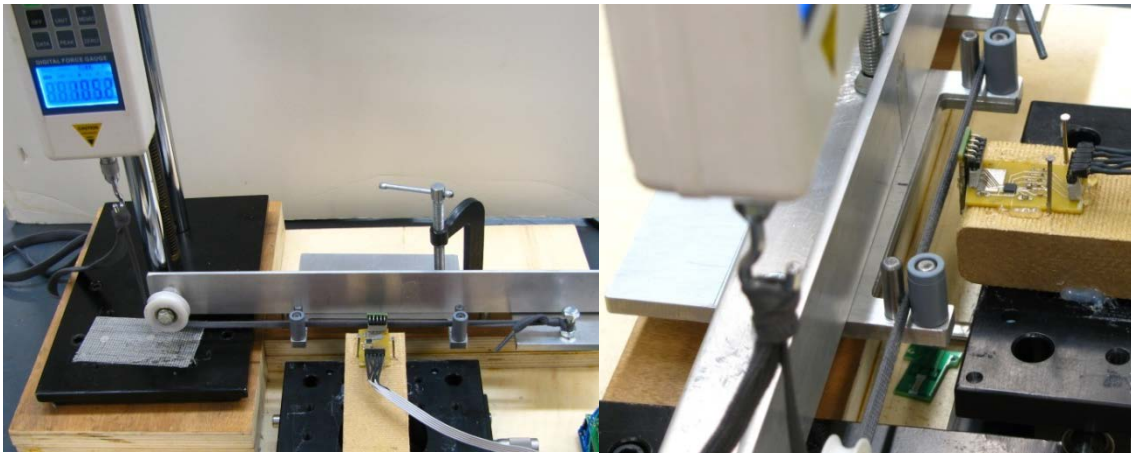

Figure 2-10: Photographs of the experimental setup for evaluating the sensor performance

Figure 2-11 shows the calibrated raw data from the three bumps for 60 N and 100 N tension values. It is evident that there is a delay between the instant when the center bumps come in contact and when side bumps come in contact. To determine the instant of contact a threshold of 0.01 N was chosen and when the readout from the left (or right) bumps exceeded the threshold it was assumed to be in contact. Since it is almost impossible to ascertain that the two bumps would come into contact at the same instant as that would involve approaching the exact middle point of the string with a perfect normal contact, the average of forces on the center bump when left bump came into contact and when right bump came into contact was treated as the sensor response.

The spread of the tests for different tensions is shown in Figure 2-12. As predicted by equation (2.2), the force experienced by the center bump for a constant displacement of the string is seen to be approximately proportional to the tension in the string.

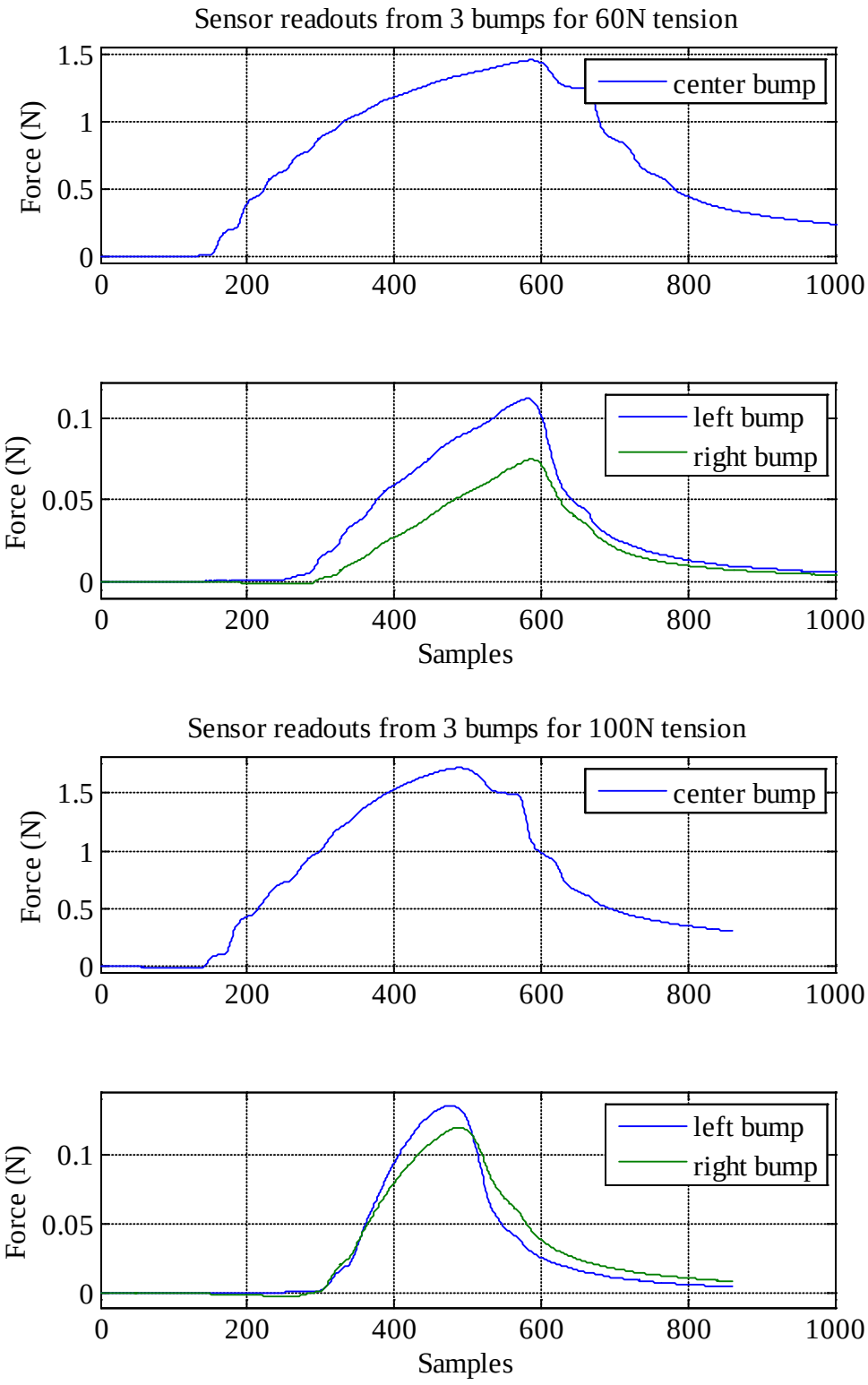

Figure 2-11: Calibrated raw data from three bumps for 60 N and 100 N tension values

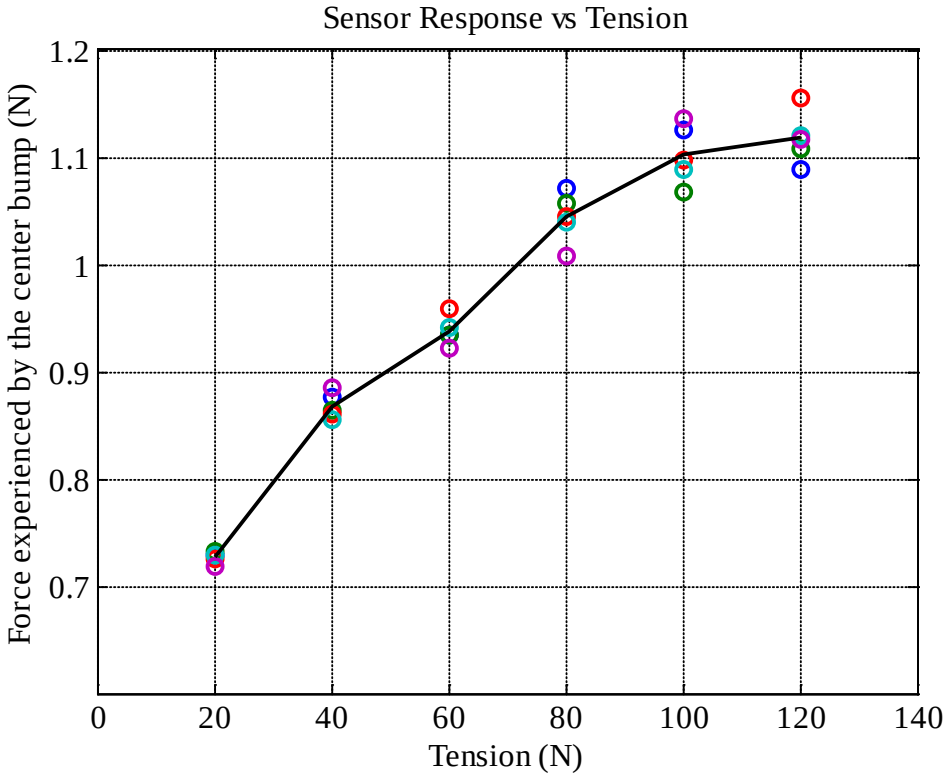

Figure 2-12: Spread of the sensor response of first generation sensor for 5 tests at different tension values

2.3 DISCUSSION

The single-probe capacitive sensor confirmed the sensing concept of using transverse forces required for causing a fixed amount of displacement in the string for the estimation of tension. However the sensor was found to be not suitable for handheld applications due to several reasons. The sensing concept relied on the fact that the sensor would come into contact with the exact midpoint of the string, otherwise the two angles would not be equal and equation (2.2) would no longer be valid. This restriction on contact at the midpoint would be difficult to enforce in a handheld sensor. Furthermore, the sensor derived its tension estimate from just two data points, the force values at the time of contact of left and right bump. Hence in a practical situation where multiple sources of noise would be present, the estimate would be highly unreliable.

CHAPTER 3

MULTI-PROBE CAPACITIVE SENSOR

The single-probe capacitive sensors measured the force on the middle sensing elements at the time instant when the other elements came into contact and relied on those force measurements to estimate the tension. The sensor had a restriction on the point of contact with the string which prohibited it from being used as a handheld sensor. Moreover the sensor relied on just two data points to estimate the tension which made the sensor response unreliable. To overcome these shortcomings a new sensing concept was developed which modeled the displacement of the string under three point contacts and used those displacements for estimating the tension in the string. A new theoretical model is presented below to model displacements of the string at three points under three point loads. As it models displacement of three points under the action of three loads, each triad of loads can be used to construct the estimator for tension and hence it eliminates the need for precise touch detection.

3.1 MODEL AND SENSOR DESIGN

The displacement (u) of a string under tension T stretched along x-axis between fixed points $x = 0$ and $x = l$, under a transverse per unit length force $f(x)$ is given by equation (3.1) [36].

$$T\frac{d^2u}{dx^2} = -f(x) \tag{3.1}$$

$$u\left(\frac{x}{x_i}\right) = \frac{F_i}{T} \times \begin{pmatrix} \frac{(l-x_i)x}{l} & ;0 \le x < x_i \\ \frac{(l-x)x_i}{l} & ;x_i \le x \le l \end{pmatrix} \tag{3.2}$$

Equation (3.1) can be solved for a point force F_i acting at point x_i as shown in Figure 3-1. The displacement of any point on this string is given by equation (3.2).

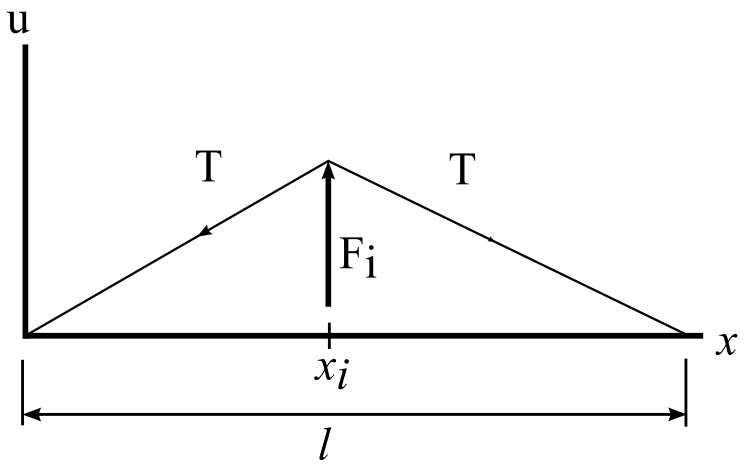

Figure 3-1: Model of a string under a transverse force

Assuming that the applied force and the displacement at that point could be measured, equation (3.2) consists of 3 unknowns, tension (T), point of application of force (x_i) and the length of the string (l). Since there are three unknowns, at least three equations are needed to solve for them, thus a sensor was designed with three sensing elements.

Each of the three sensing elements was modeled as a spring, referred to as bump, and a capacitance based force sensor was positioned under it. The bump is used to apply a point force, while the capacitive sensor is used to measure the magnitude of the applied force. The bump was assumed to have a linear displacement to force curve, thus the relationship between the displacement of the bump, y, and the normal force exerted on it, F, can be expressed by equation (3.3), where k is equivalent of the spring constant for the bump.

$$F = ky \tag{3.3}$$

The three bumps were placed along a straight line with a constant pitch, so that their relative positions with respect to each other are known. A schematic of the sensor is shown in Figure 3-2.

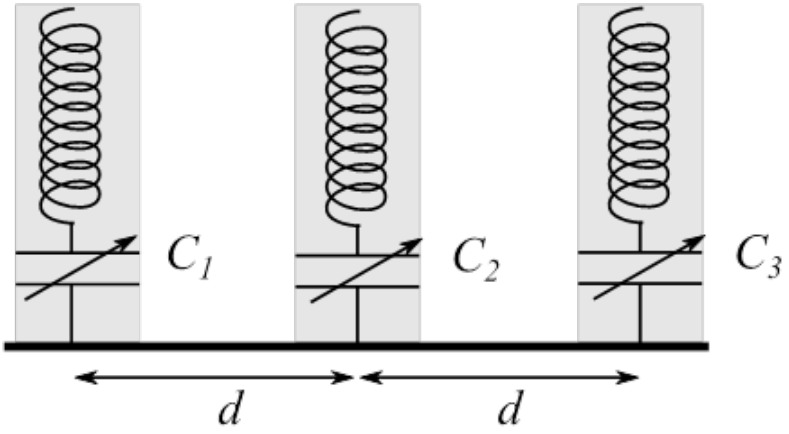

Figure 3-2: Schematic of the generation 2 sensor

For three point forces acting at points x_1, x_2 and x_3, by the superposition principle, the three displacements, u_1, u_2 and u_3 at the respective points, are given by equation (3.4).

$$\begin{bmatrix} u_1 \\ u_2 \\ u_3 \end{bmatrix} = \frac{1}{T} \begin{bmatrix} \frac{(l-x_1)x_1}{l} & \frac{(l-x_2)x_1}{l} & \frac{(l-x_3)x_1}{l} \\ \frac{(l-x_2)x_1}{l} & \frac{(l-x_2)x_2}{l} & \frac{(l-x_3)x_2}{l} \\ \frac{(l-x_3)x_1}{l} & \frac{(l-x_3)x_2}{l} & \frac{(l-x_3)x_3}{l} \end{bmatrix} \times \begin{bmatrix} F_1 \\ F_2 \\ F_3 \end{bmatrix} \tag{3.4}$$

By the geometry of the sensor the distance between the two adjacent points where the force is applied is known and is equal to d. These two additional constraints can be expressed as equation (3.5).

$$x_1 = x_2 - d \tag{3.5a}$$

$$x_3 = x_2 + d \tag{3.5b}$$

The equation (3.4), under the constraints expressed by equation (3.5), can be summarized in a matrix form, as given by equation (3.6), where A_1 is given by equation (3.7).

$$u = A_1(l, x_2, T) \times F \tag{3.6}$$

$$A_1(l, x_2, T) = \frac{1}{T}\begin{bmatrix} \frac{(l-(x_2-d))(x_2-d)}{l} & \frac{(l-x_2)(x_2-d)}{l} & \frac{(l-(x_2+d))(x_2-d)}{l} \\ \frac{(l-x_2)(x_2-d)}{l} & \frac{(l-x_2)x_2}{l} & \frac{(l-(x_2+d))x_2}{l} \\ \frac{(l-(x_2+d))(x_2-d)}{l} & \frac{(l-(x_2+d))x_2}{l} & \frac{(l-(x_2+d))(x_2+d)}{l} \end{bmatrix} \tag{3.7}$$

Figure 3-3 shows the schematic of the sensor before and after contact with the string. Since the displacements of the sensor and the bumps have to be compatible, the compression in the bump (y) can be modeled by equation (3.8), where z is the displacement of the base of the sensor.

$$y = z - u \tag{3.8}$$

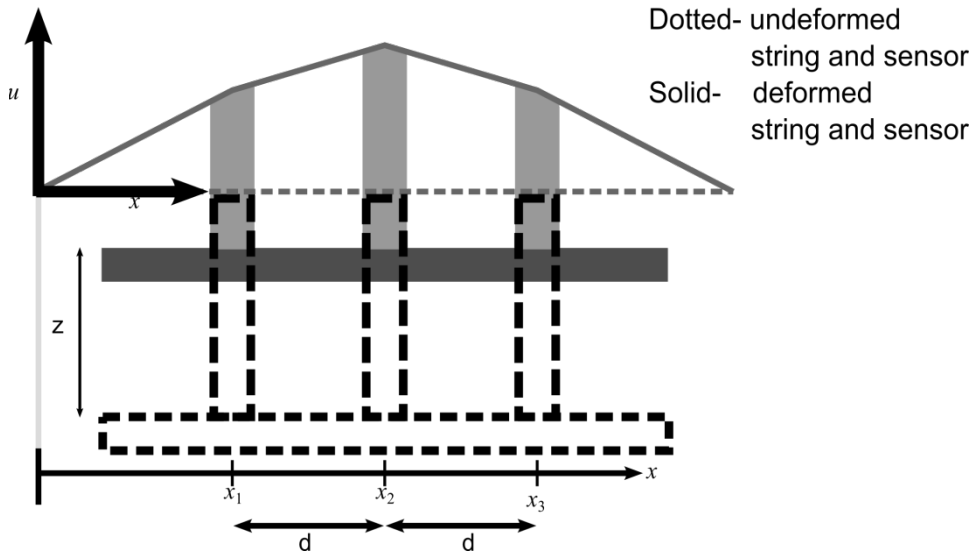

Figure 3-3: Sensor before and after contact with the string

Substituting y in terms F from equation (3.3) in equation (3.8), another relationship between u and F can be obtained. This relationship is given by equation (3.9).

$$u = z - F/k \tag{3.9}$$

Substituting equation (3.9) in equation (3.6) a relationship expressed by equation (3.10) can be obtained.

$$Z = (A_1 + \frac{1}{k} I)F \tag{3.10}$$

where Z is a vector containing the displacement of the base of the three bumps. Under assumption of a normal contact, the three displacements can be assumed to be same, z, hence Z can be represented as:

$$Z = \begin{bmatrix} z \\ z \\ z \end{bmatrix} \tag{3.11}$$

Equation (3.10) can be solved to find the three force values as a function of displacement of the sensor for given tension value. Assuming that $(A_1 + I/k)$ is non singular the solution to the above equation is presented in equation (3.12).

$$\begin{bmatrix} F_1 \\ F_2 \\ F_3 \end{bmatrix} = \frac{z}{\det(A_1 + I/k)} \begin{bmatrix} \frac{\left(-d^3k^2 + lT^2 + d^2k\left(-2T + k(l - \text{x2})\right) + 3dkT(l - \text{x2})\right)}{k^2lT^2} \\ \frac{(-2d^2k + dkl + lT)}{k^2lT} \\ \frac{\left(-d^3k^2 + lT^2 + 3dkT\text{x2} + d^2k(-2T + k\text{x2})\right)}{k^2lT^2} \end{bmatrix} \tag{3.12}$$

Since the force values are functions of z, x_2 and l,which are all unknown, a ratio of linear combinations of the force values was constructed that is independent of these variables. It was found that the expression given by equation (3.13) is dependent only on the tension, T, in the string.

$$R = \frac{F_2}{(F_1 + F_3)/2} = \frac{2T}{2T + kd} \tag{3.13}$$

The ratio, R, described in equation (3.13) will be referred to as the response of the sensor. This ratio is essentially a ratio of the force experienced by the center bump to the average

force experience by the side bumps. It is a monotonically increasing function of tension and approaches unity as the tension increases.

A sensor was designed to implement the above sensing concept. The basic structure of the sensor was similar to that of the single-probe capacitive sensor, however the bumps were made from a softer material in order to let them compress and were of equal height.

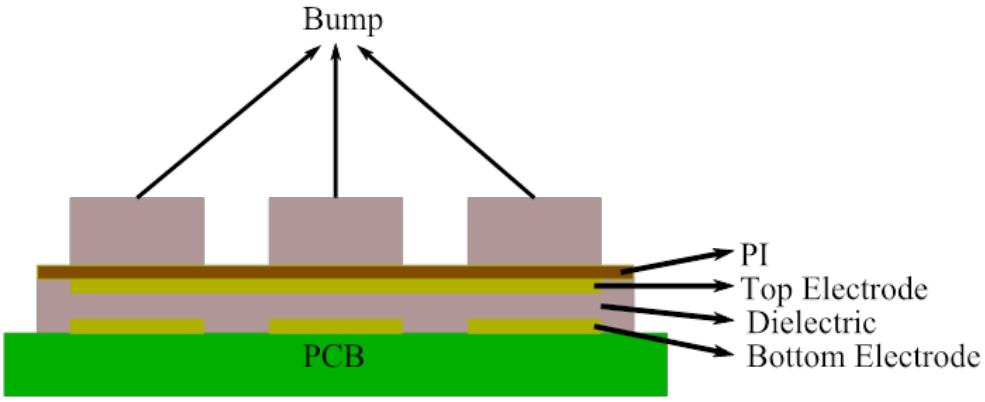

Figure 3-4: Design of the second generation sensor

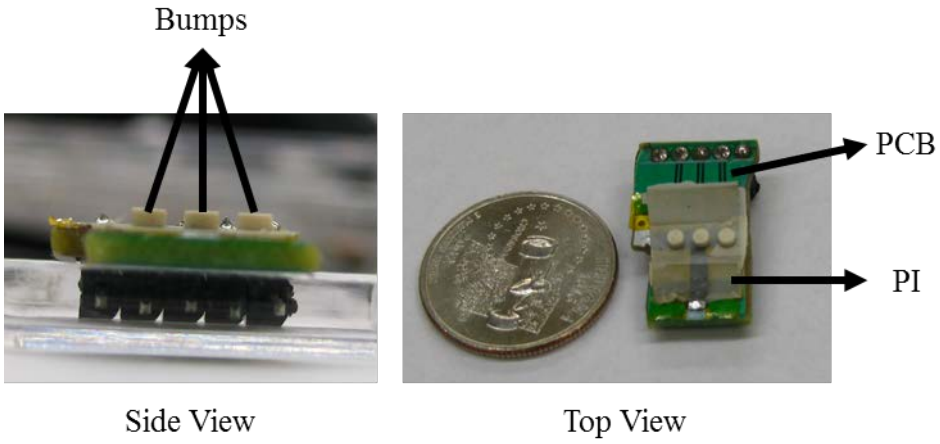

Figure 3-5: Photograph of the second generation sensor

Figure 3-4 shows the design of the proposed sensor. The sensor has three bumps of equal height made from urethane rubber (PMC-724 from Smooth-On Inc.). The durometer hardness of this rubber was 40A which translates to a young's modulus of approximately

1.54 MPa. The height of the bumps was chosen to be 1 mm. The center of center distance of the adjacent bumps was chosen to be 3 mm.

The fabrication process was identical to that used for the single-probe capacitive sensors except for a different mold and rubber. Figure 3-5 shows the photograph of the sensor after fabrication.

3.2 EXPERIMENTAL RESULTS

Since the measured output from the sensor was capacitance, each bump of the sensor was characterized to generate a capacitance to force calibration curve. The test was performed thrice for each bump to test for repeatability of the result. A setup described in section 2.2 and depicted in Figure 2-7 was used to characterize each bump of the sensor. Figure 3-6 shows the calibration curve for each of the three bumps. The tests were found to be repeatable for each of the bumps. Though a non-linear trend is present in the calibration curves, it was ensured that the forces on each bump are between 0.5-2.5 N during testing and a linear approximation was used to model the relationship between sensor response and force for this range.

The setup described in section 2.2 and shown in Figure 2-9 and Figure 2-10 was used to evaluate the performance of the current sensor. Figure 3-7 shows the calibrated raw data from the three bumps for 60 N and 100 N tension values. The side bumps experience more force than the center in both the cases, hence the ratio of center to average of side would be less than unity. This is as expected from equation (3.13).

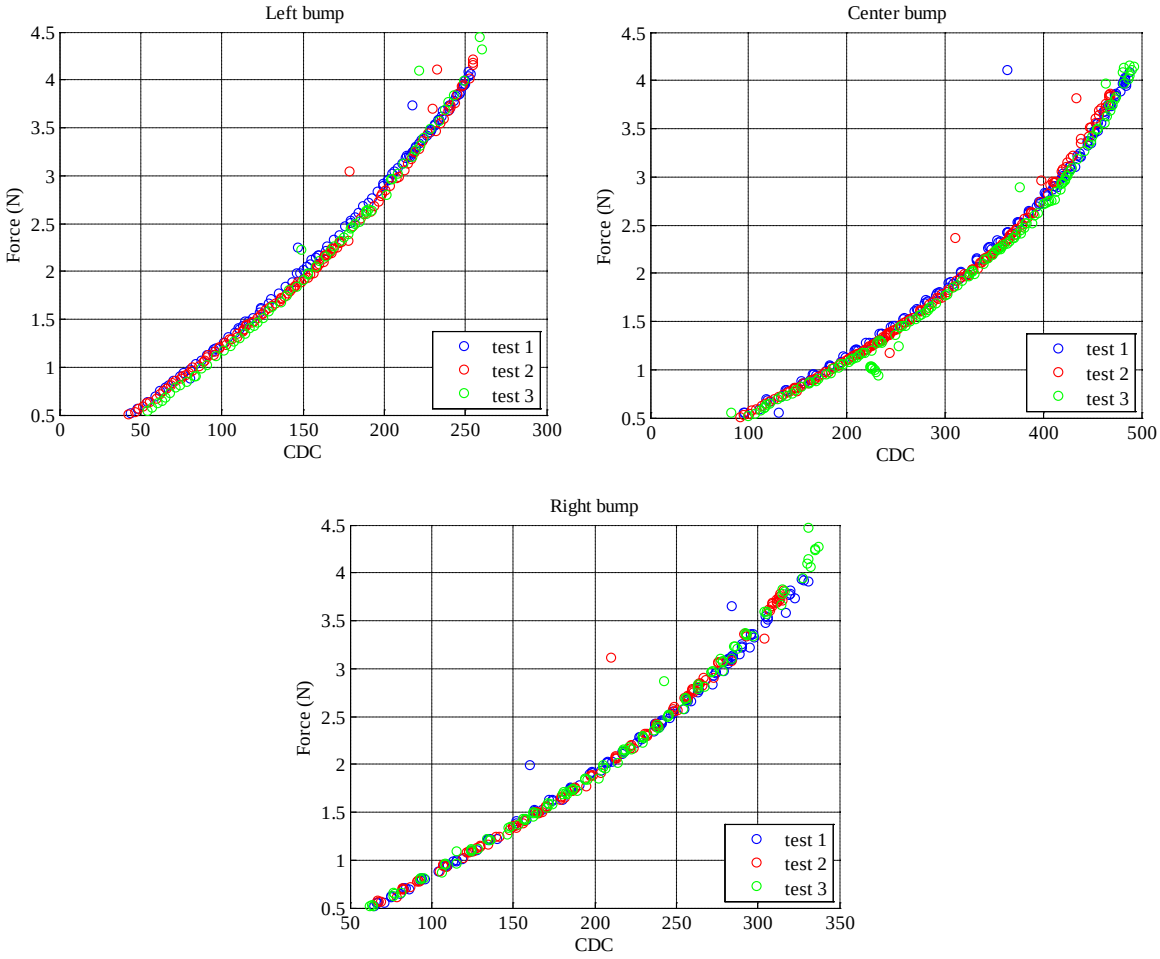

Figure 3-6: Calibration curves for the three bumps of second generation sensor

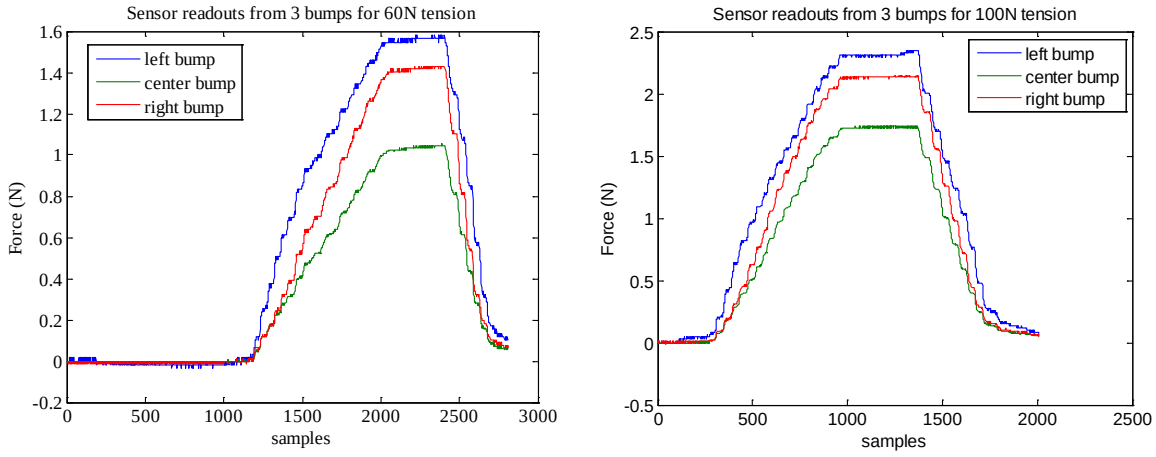

Figure 3-7: Calibrated raw data from three bumps for 60 N and 100 N tension values

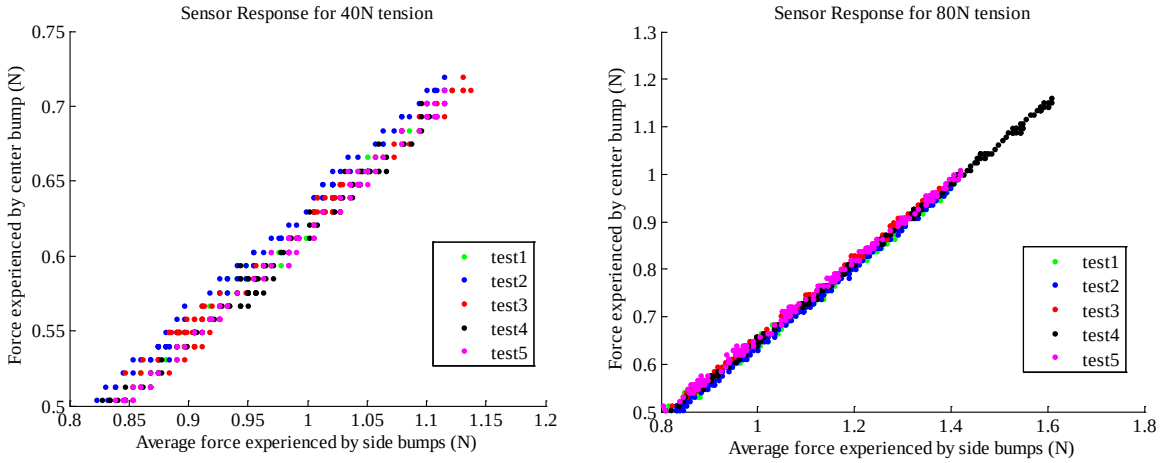

Figure 3-8: Force experienced by center bump vs. average for force experienced by side bumps for 40N and 80N tension values

Tests were performed for different tension values in the range 20 N - 100 N. Five tests were performed in quick succession at each tension values to test for repeatability. Figure 3-8 shows a plot of the force experienced by the center bump vs. the average of forces experienced by side bumps for 40 N and 80 N tensions. Again as predicted by equation (3.13), the slope of the line between force experienced by the center bump and the average of force experienced by the side bumps is independent of force levels. Also the output of the sensor is repeatable as shown by five tests. An ordinary least squares (OLS) line was fitted to the data for each test at each tension value, and the slope of that line was calculated. Figure 3-9 shows the fitted OLS line for one test at each tension value. It can be clearly seen that the slopes of the line increases with the increase in tension.

The estimated slopes from each of the five tests for each tension value are plotted against the respective tension value in Figure 3-10. From the graph it can be seen that the estimates are repeatable and the resolution of the current sensor is 10 N for lower values of tension and 20 N for higher values.

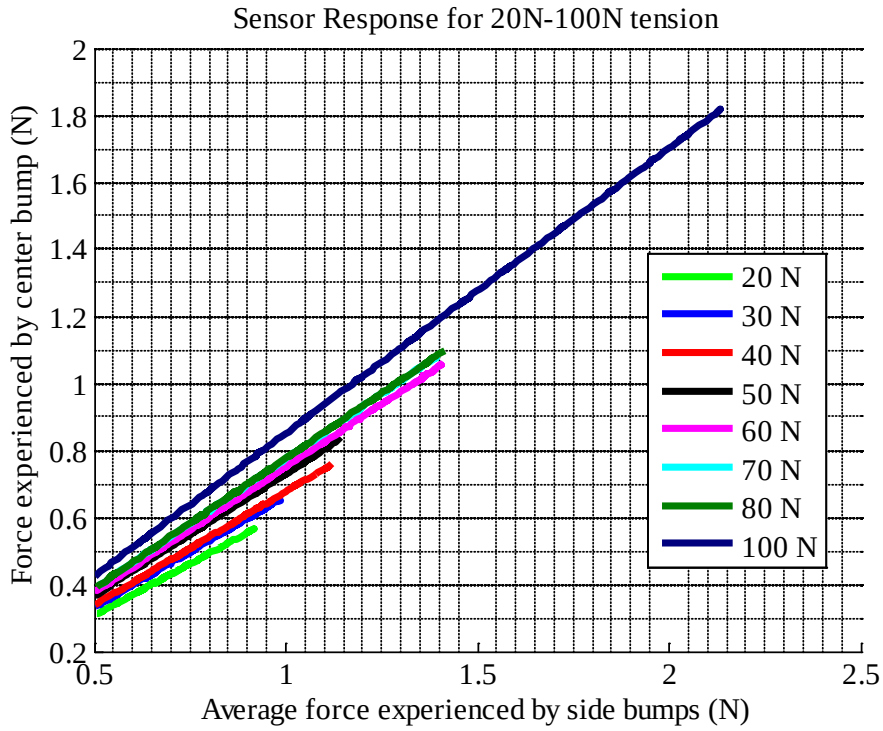

Figure 3-9: Fitted lines for one test for 20-100N tension

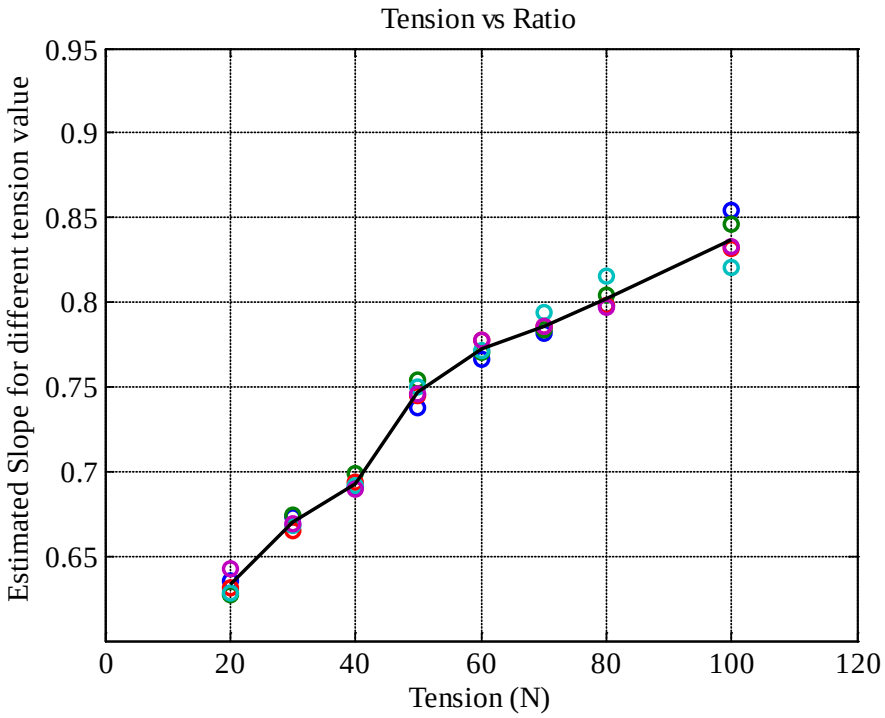

Figure 3-10: Summary of estimated slopes for five tests for 20N-100N tension

3.3 DISCUSSION

The multi probe capacitive sensor confirmed the sensing concept, but there were multiple challenges that thwart the successful implementation of the current sensor.

3.3.1 Challenge 1: Limited permissible displacement

The height of the bumps is restricted to 1mm because bumps taller than 1 mm tend to buckle upon contact with the string. This restriction in height translates to a restriction in the amount of allowed displacements before the edges of the PCB come into contact with the string.

3.3.2 Challenge 2: Day to day variability in results

The sensor results seems to be repeatable when performed in quick succession without removing the sensor from the translation stage, however when the sensor is remounted again after removal, the results are not consistent.

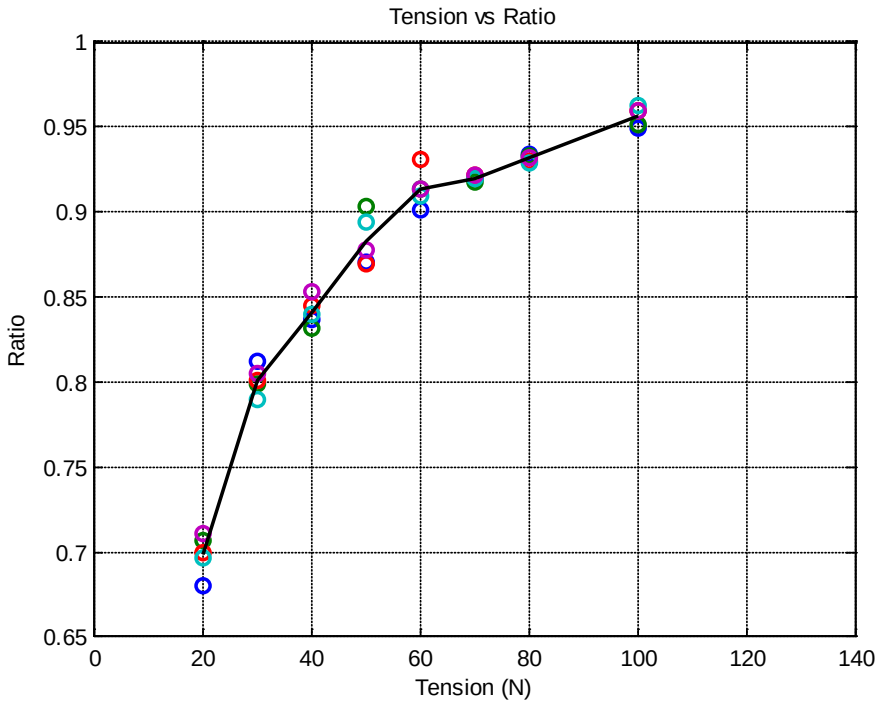

Figure 3-11: Summary of estimated slopes for five tests for 20N-100N tension

Figure 3-11 shows the results for a second set of tests. Again five tests were done in quick succession at each tension value to test the repeatability. Same values of threshold were used for calculating the slope of OLS line for both the tests. Although both the tests show good repeatability within the respective five tests done at quick succession, the results of the two tests are quite different. In fact, as shown in Figure 3-12, there is a big offset in the results from the two set of tests. This offset causes the achievable accuracy of the sensor to be poor.

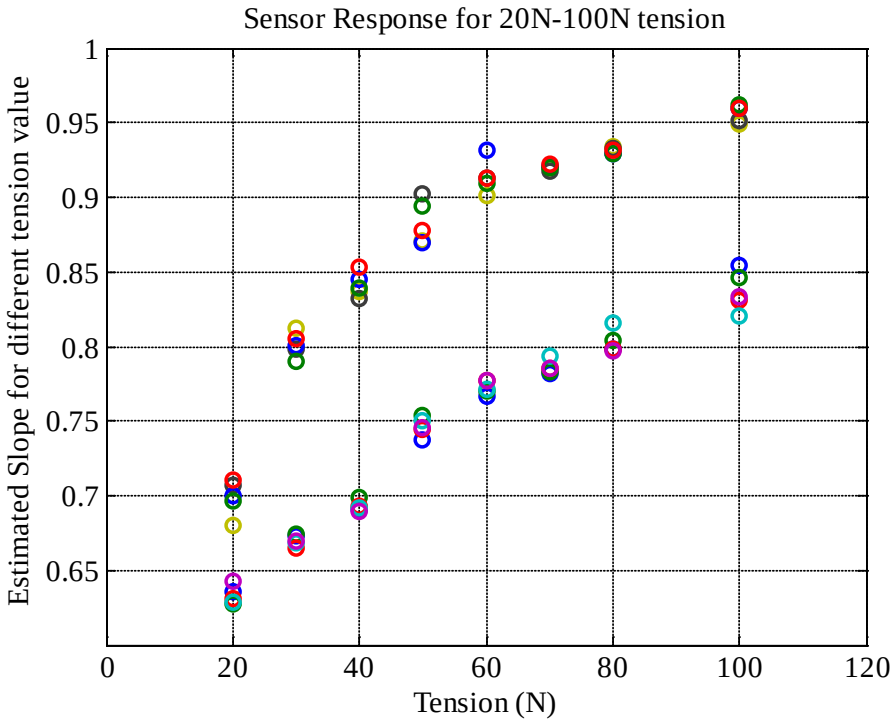

Figure 3-12: Summary of estimated slopes for 20N-100N tension for both set of tests

It is suspected that this offset from test to test is due to the departure from normal contact that occurs from test to test. The equations in section 3.1 were derived for a normal contact. Though the sensor was always visibly aligned to have approximately normal contact, even a slight departure from normality seems to cause big variations in the estimated values.

The issue could be possibly reduced by allowing higher displacements as then the orientation errors could have smaller influence in the readout. This influence might still

cause variation, but as the displacements would be large, it is suspected that the variation would be smaller.

3.3.3 Challenge 3: Fabrication challenges

The sensor also suffered from a lack of control in fabrication. The process of molding bumps tended to introduce air bubbles in the bump, which caused the force-displacement curve to further deviate from linearity and also made it unreliable as the curve depended upon the point of contact on the bump. Figure 3-13 illustrates the dependence of force-displacement on point of contact, due to the presence of bump directly under the point of contact, the same bump in scenario (A) will displace more than in scenario (B) for the same force.

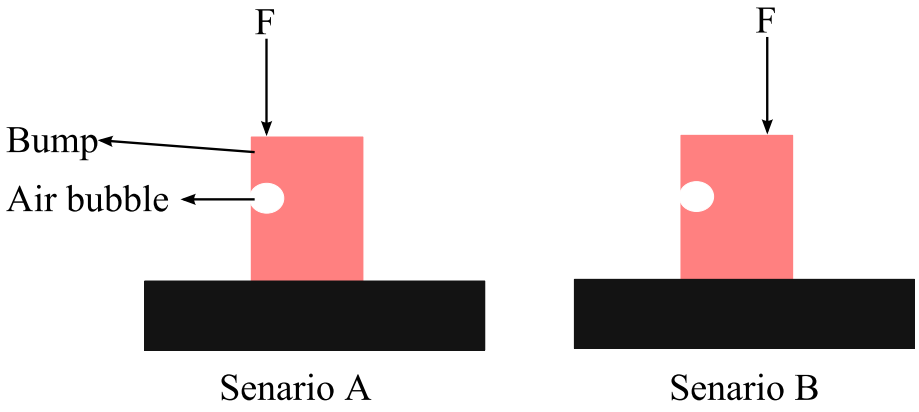

Figure 3-13: Different point of contact on bump with air bubble

The process of laying dielectric layer also did not ensure uniform dielectrics, causing the initial capacitances to differ from each other by an order of magnitude.

3.3.4 Challenge 4: Mechanical Crosstalk and Proximity effects

The sensor was based on the capacitive sensing approach and all the three sensors shared a common dielectric. The shared dielectric introduced mechanical crosstalk in the bumps, i.e. when force was exerted on one of the bumps some change in capacitance was observed not only in that sensor but also the adjacent sensors. Figure 3-14 shows the readouts of the three sensors when the force was exerted on the middle bump.

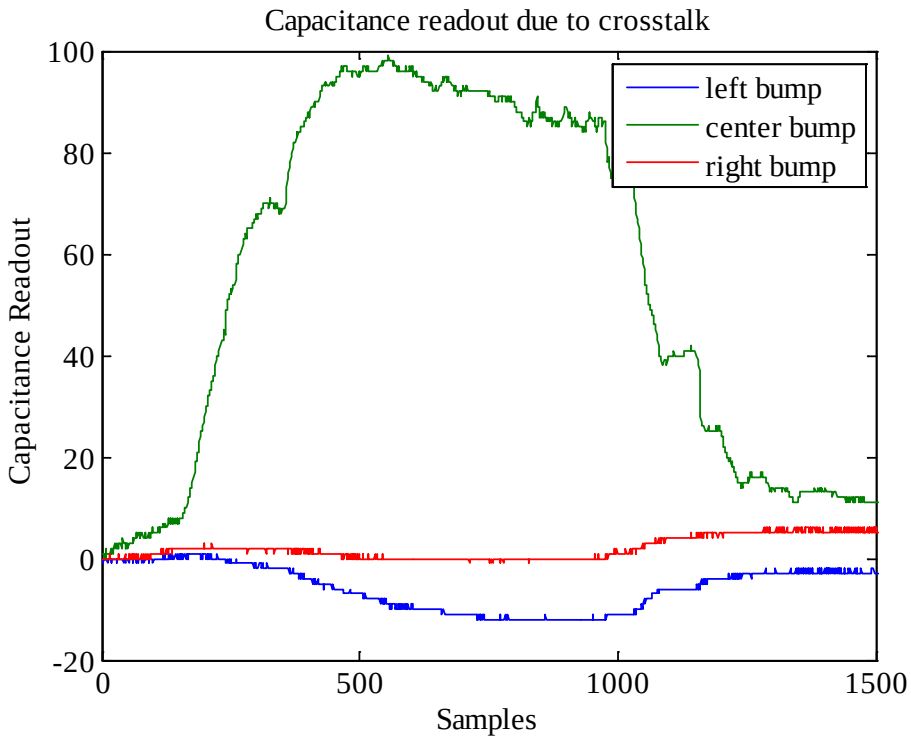

Figure 3-14: Capacitance readout of the three sensors when a force was exerted on the middle bump

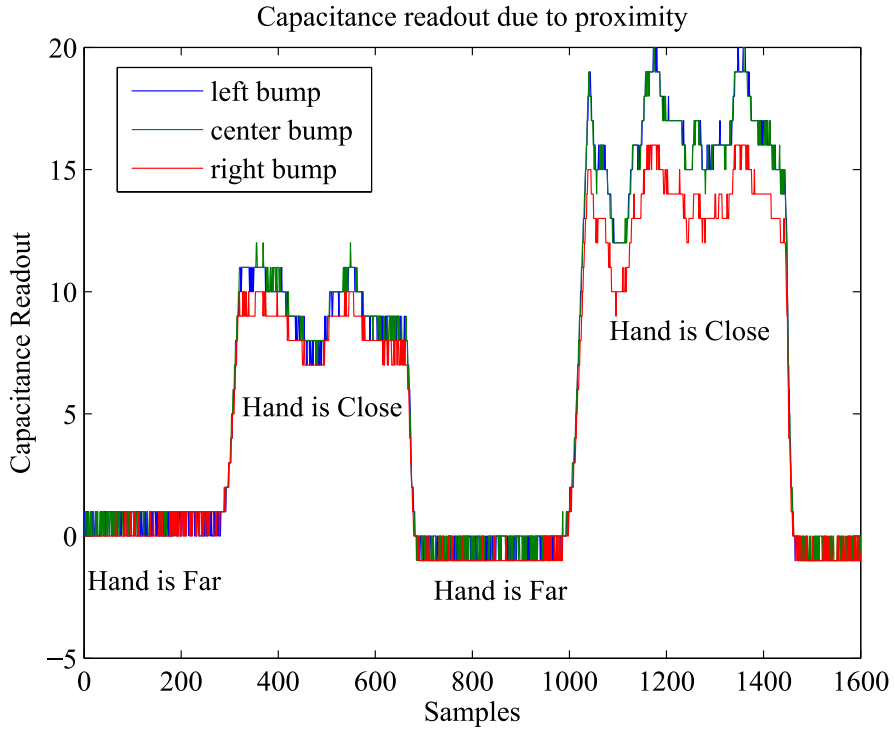

Figure 3-15: Capacitance change due to hand approaching the sensor

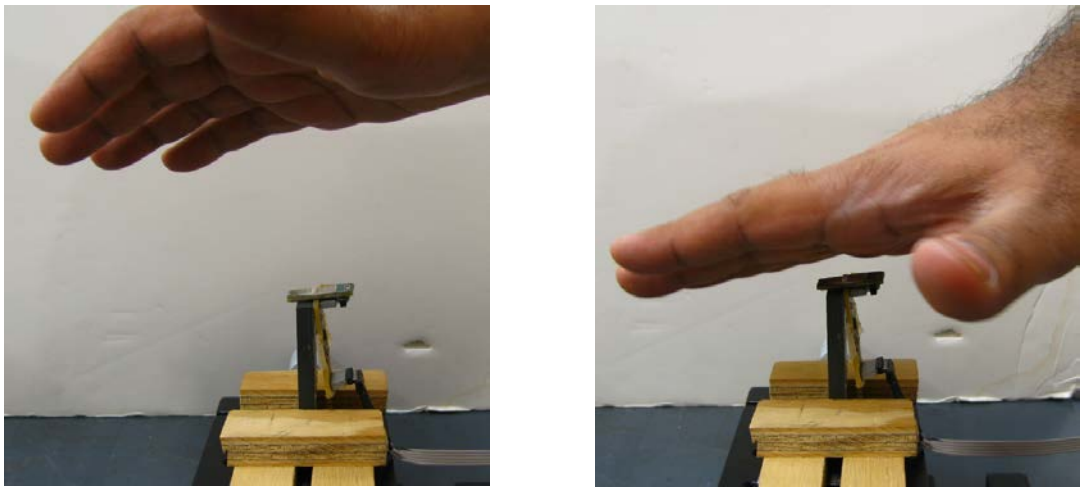

Figure 3-16: Position of hand while testing proximity effects

Since the sensors were designed to read the change in capacitance between a ground plate and a second plate, the sensor readout change when any other object that can act as ground approaches the sensor. Since the human body can act as a ground plate, the sensor readout changes when it approaches the body and the readout gets corrupted. Figure 3-15 shows the readout from the sensor for two different positions of the hand shown in Figure 3-16. As can be seen there is an increase in the sensor readout when the hand is close to the sensor as compared to when it is far away.

CHAPTER 4

MULTI-PROBE MAGNETIC SENSOR

This chapter presents a magnetic measurement based design for the multi-probe sensor. This design addresses the low repeatability of the estimate obtained from the multi-probe capacitive sensor described in the previous chapter. The main reasons of the low repeatability of the capacitive sensor were:

1. Noise due to proximity effects
2. Small range of permissible displacements
3. Suspected non-linear behavior between force and displacement of the rubber bumps due to rubber properties and fabrication issues.

This sensor is based on measurement of the change in magnetic field due to the displacement of a permanent magnet under force. The rubber bumps are replaced by a stainless steel piston in conjunction with coil springs that exhibit a linear force to displacement behavior. The coil springs also permit a higher range of displacements. To resolve the challenges of repeatable fabrication three dimensional printing methods are utilized.

4.1 SENSOR DESIGN

The measurement principle of the sensor is shown in Figure 4-1. The bump assembly of this sensor consists of a piston (P), a magnet (M) and a coil spring. A printed circuit board with AS5510 Hall-effect magnetic encoder chip (C) from ams AG is placed below the spring. When force (F) is applied on the piston (P), the spring under the piston compresses and allows the magnet (M) to come closer to the chip (C). The displacement of the magnet causes an increase in the density of magnetic field lines incident on the surface of the chip, thus causing an increase in the readout of the chip.

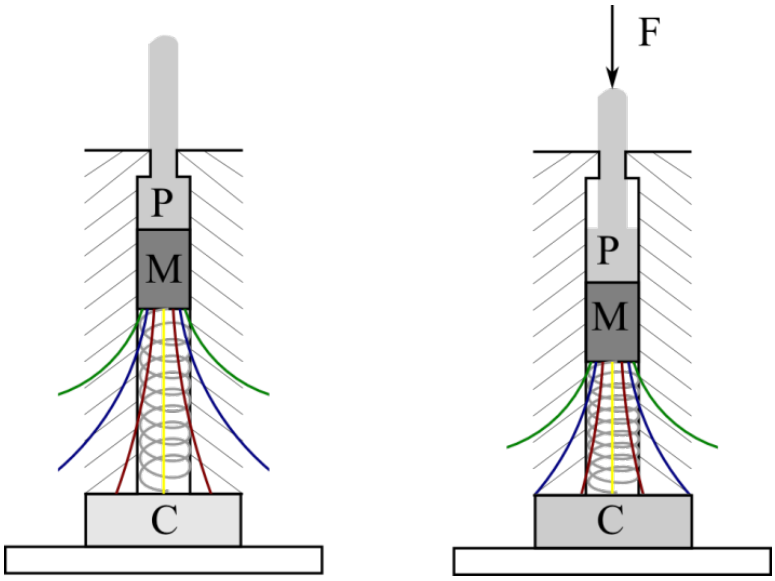

Figure 4-1: Bump assembly before and after application of force

Three such bump assemblies are arranged in a linear fashion similar to the multi-probe capacitive sensor. The cross section view of the model for the sensor assembly is shown in Figure 4-2 and a photograph of the actual sensor is shown in Figure 4-3

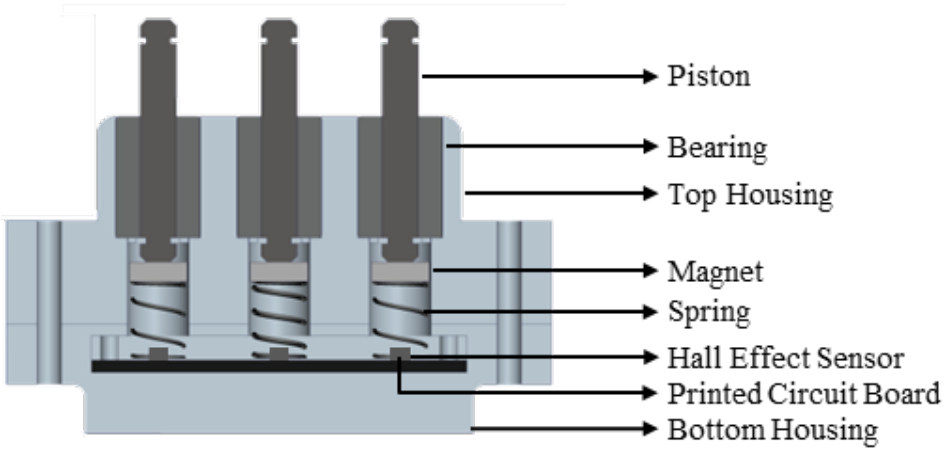

Figure 4-2: Cross section view of the model of the multi-probe magnetic sensor

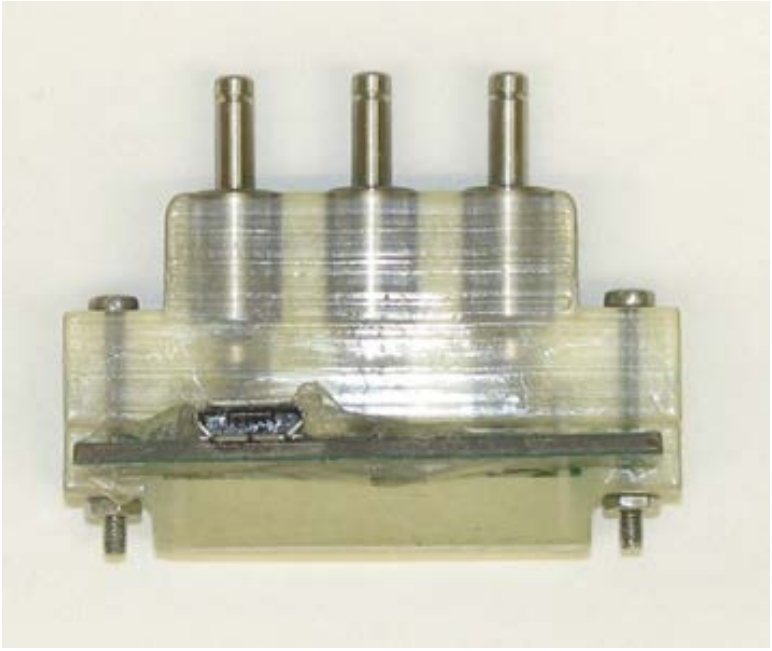

Figure 4-3: Photograph of the multi-probe magnetic sensor

The sensor assembly comprises of a housing which is printed using a transparent polyjet resin. For ease of assembly, the housing is split into two halves: top and bottom which can be joined together using a nut and bolt on either sides. There are three cylindrical slots in the housing. Each of the three slots are fitted with a linear bearing (SLMU3 from Misumi Inc) that allows the pistons of the bump assembly to move freely in the axial direction while constraining their motion in the radial direction. The center to center distance of these slots is 10 mm. The bump assembly comprises of a circular stainless

steel shaft of 3 mm diameter, a neodymium magnet and a spring of spring constant 1.96 N/mm. On the lower side, the spring is supported on a thin plastic laminate which is placed between the circuit board and the springs. The laminate is placed to avoid any shorts that might occur due to the spring coming into contact with the traces on the PCB. A printed circuit board (PCB) consisting of five AS5510 magnetic encoders, one under each slot and two for cancelling the magnetic coupling terms as described in section 4.3, is placed in the bottom housing and is aligned to the slots with the help of guide pins.

Since this sensor, similar to the multi-probe capacitive sensor, also relies on measuring the displacement of three points under an action of three point loads, the equation of displacements of the points under the action of three forces is still given by equation (3.6), which, for the sake of continuity, has been presented again as equation (4.1).

$$u = A_1(l, X_2, T) \times F \tag{4.1}$$

where,

$$A_1(l, x_2, T) = \frac{1}{T}\begin{bmatrix} \frac{(l-(x_2-d))(x_2-d)}{l} & \frac{(l-x_2)(x_2-d)}{l} & \frac{(l-(x_2+d))(x_2-d)}{l} \\ \frac{(l-x_2)(x_2-d)}{l} & \frac{(l-x_2)x_2}{l} & \frac{(l-(x_2+d))x_2}{l} \\ \frac{(l-(x_2+d))(x_2-d)}{l} & \frac{(l-(x_2+d))x_2}{l} & \frac{(l-(x_2+d))(x_2+d)}{l} \end{bmatrix} \tag{4.2}$$

The displacement (Δy_i) of piston i upon application of a force F_i is given by equation (4.3), where k_i is the stiffness of the coil spring under that piston.

$$F_i = k_i \Delta y_i \tag{4.3}$$

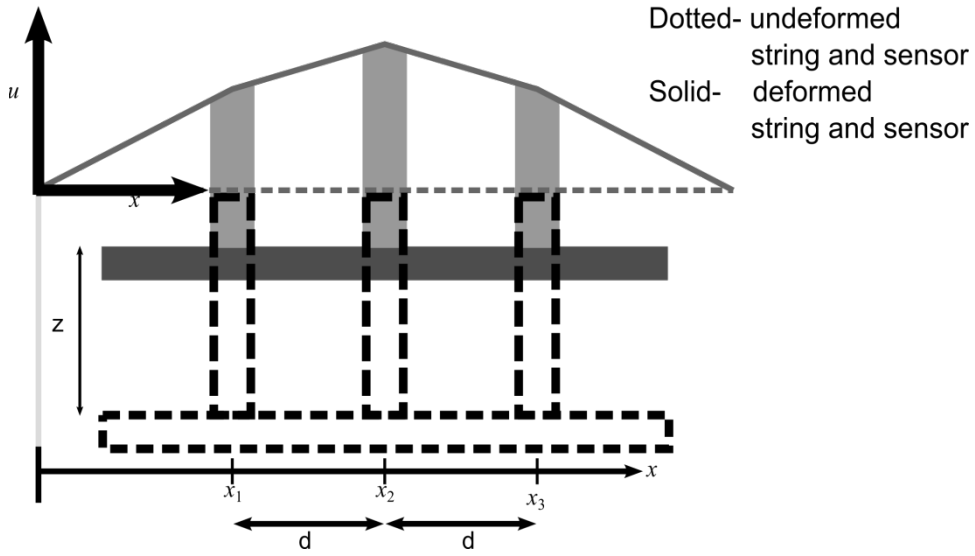

Figure 4-4: Sensor before and after contact with the string

Referring to Figure 4-4, under a normal contact assumption (the same displacement of the base of the three bumps) the compression of springs can be modeled as equation (4.4), where Z is the displacement of the base of three bump assemblies and for normal contact is given by equation (4.5).

$$\Delta Y = Z - U \tag{4.4}$$

$$Z = \begin{bmatrix} z \\ z \\ z \end{bmatrix} \tag{4.5}$$

Substituting F and U from equations (4.3) and (4.4) into equation (4.1), a relationship between the piston displacements (ΔY) and sensor displacement (Z) can be obtained. This relationship is given by equation (4.6), where K, given by equation (4.7), is the stiffness matrix of the combined system.

$$(I + A_1 K)\,\Delta Y = Z \tag{4.6}$$

Though the sensor has identical springs in the side and center slots, in the interest of generality, the stiffness of side spring is denoted by K_s while that of center spring is denoted by K_c.

$$K = \begin{bmatrix} K_s & 0 & 0 \\ 0 & K_c & 0 \\ 0 & 0 & K_s \end{bmatrix} \tag{4.7}$$

The displacements of the three pistons, given in equation (4.8), can be obtained by solving Equation (4.6).

$$\begin{bmatrix} \Delta Y_1 \\ \Delta Y_2 \\ \Delta Y_3 \end{bmatrix} = \frac{z}{\det(A_1 K + I)} \begin{bmatrix} \frac{\left(-d^3 K_c K_s + lT^2 + d^2 K_s(-2T + K_c(l - \mathrm{x2})) + Td(K_c + 2K_s)(l - \mathrm{x2})\right)}{lT^2} \\ \frac{(lT + K_s d(l - 2d))}{lT} \\ \frac{(-d^3 \mathrm{K_c} K_s + lT^2 + K_s d^2(K_c x_2 - 2T) + Td(K_c + 2K_s)x_2)}{lT^2} \end{bmatrix} \tag{4.8}$$

Since the displacement values are functions of z, x_2 and l, which are all unknown, an estimator, given by equation (4.9) can be constructed which depends only on the tension in the string. This ratio would be referred to as the response of this sensor.

$$R = \frac{\Delta Y_2}{(\Delta Y_1 + \Delta Y_3)/2} = \frac{2T}{(2T + K_c d)} \tag{4.9}$$

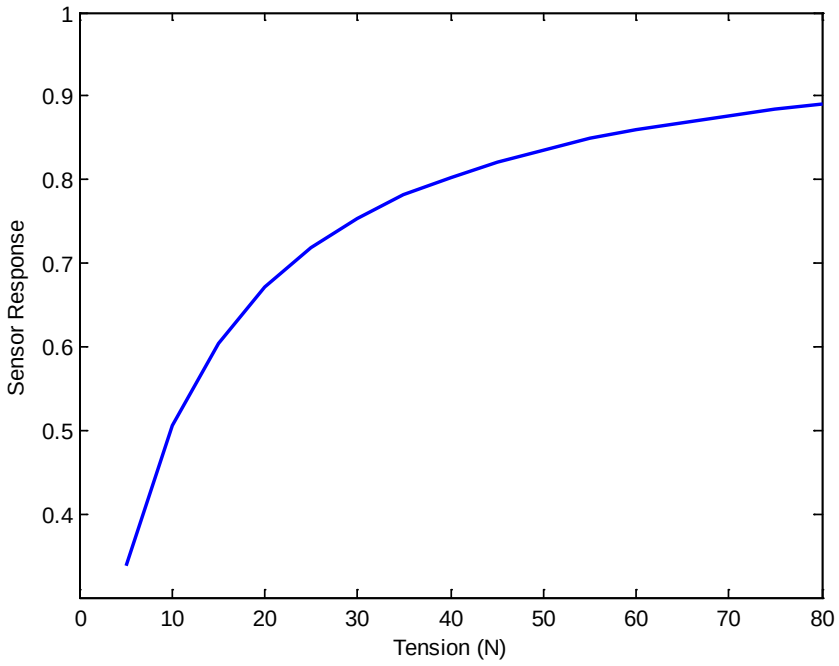

Figure 4-5: Theoretical plot of ratio as function of tension

Figure 4-5 shows a plot of the sensor response, described by equation (4.9), as a function of the tension using the design value of the spring stiffness (k_c) and the pitch (d). The sensor response is an injective function of the tension (T) and thus can be used to obtain an estimate of tension.

4.2 MODEL OF MAGNETIC FIELD IN SENSOR

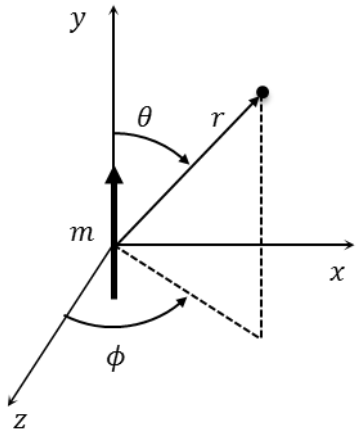

Figure 4-6: Magnetic dipole pointing in y direction place at origin

Figure 4-6 shows a magnetic dipole m pointing in y direction placed at the origin. The magnetic field at a point whose coordinates in polar coordinate system are given by (r, θ, ϕ) is given by equation (4.10) [37].

$$B(r,\theta) = \frac{\mu_0 m}{4\pi r^3}\left(2\cos(\theta)\,\hat{r} + \sin(\theta)\,\hat{\theta} \right) \tag{4.10}$$

If the point of interest lies in the $x-y$ plane, the magnetic field given by equation (4.10) can be represented in a Cartesian coordinate system by equation (4.11).

$$B(x,y) = \frac{\mu_0 m}{4\pi r^3}\left[3\sin(\theta)\cos(\theta)\,\hat{x} + (3\cos^2(\theta) - 1)\hat{y} \right] \tag{4.11a}$$

where,

$$r = \sqrt{x^2 + y^2} \tag{4.11b}$$

$$\theta = \tan^{-1}\left(\frac{x}{y}\right) \tag{4.11c}$$

Since the hall-effect sensors utilized in this sensor are unidirectional, due to the relative orientation of the permanent magnets and the hall-effect sensor they are limited to measuring magnetic field components in y −direction. The magnetic effect (B_{ij}) of the ith magnet on jth chip is given by equation (4.12), where y is distance of the magnet from the chip in vertical direction, x is offset (fixed by design) between the chip and the magnet under consideration in x direction and m is an equivalent dipole strength of the magnet. For axial ($x = 0$) and off-axial ($x \neq 0$) cases, equation (4.12) can be written as equation (4.13a) or (4.13b) respectively.

$$B_{ij} = B(x, y).\hat{y} = \frac{\mu_o m}{4\pi(x^2 + y^2)^{3/2}}\left(3\frac{y^2}{x^2 + y^2} - 1\right) \tag{4.12}$$

$$B_{ij} = k\, B_A(y) \tag{4.13a}$$

$$B_{ij} = k\, B_O(y, x) \tag{4.13b}$$

where,

$$B_A(y) = \frac{2}{y^3} \tag{4.13c}$$

$$B_O(y) = \frac{1}{(x^2 + y^2)^{3/2}}\left[3\frac{y^2}{x^2 + y^2} - 1\right] \tag{4.13d}$$

$$k = \frac{\mu_0 m}{4\pi} \tag{4.13e}$$

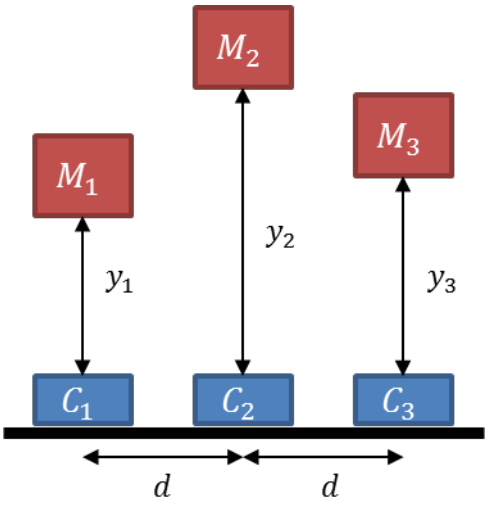

Figure 4-7: A sample sensor configuration

A typical sensor configuration is shown in Figure 4-7, where M_i represent the three magnets and C_i represent the three hall-effect sensor chips; using superposition principle the readouts (R_i) of the three sensors under each magnet are given by equation (4.14), where k_1, k_2 and k_3, as defined by equation (4.13e), are constants representing the magnetic strengths of the three magnets.

$$R_1 = k_1 B_A(y_1) + k_2 B_0(y_2, d) + k_3 B_0(y_3, 2d) \quad (4.14a)$$

$$R_2 = k_1 B_0(y_1, d) + k_2 B_A(y_2) + k_1 B_0(y_3, d) \quad (4.14b)$$

$$R_3 = k_1 B_0(y_1, 2d) + k_2 B_O(y_2, d) + k_3 B_A(y_3) \quad (4.14c)$$

4.3 MAGNETIC CROSS COUPLING

Since the sensor consists of three magnets placed in close proximity of each other, as can be seen in equations (4.14) , the readings of each of the magnetic encoders are affected by not only the magnet directly above it but also the adjacent magnets. This phenomenon is illustrated in Figure 4-8 through Figure 4-10 which shows the readout of the three hall-effect sensors placed when only one of the pistons is displaced.

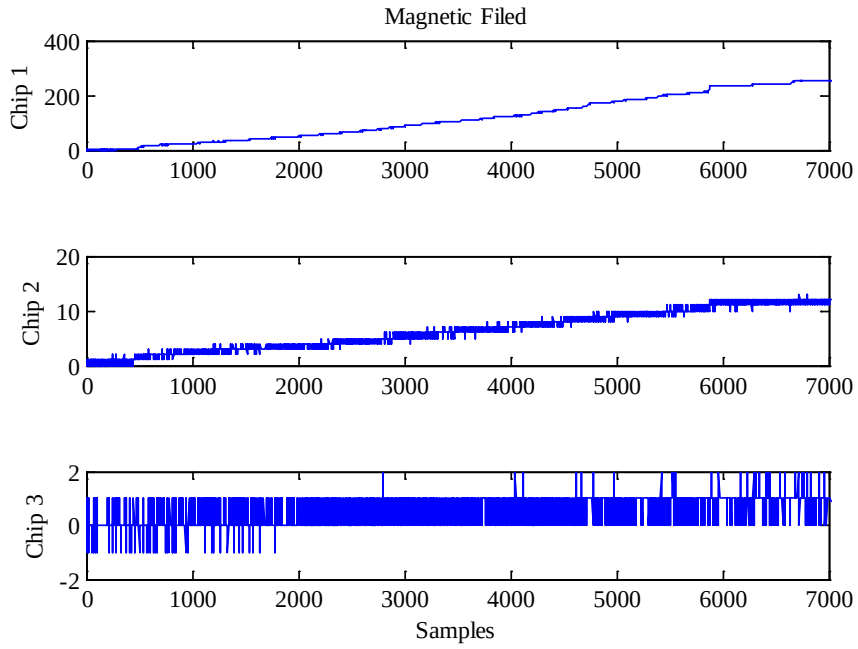

Figure 4-8: Readout of three chips when only piston 1 is displaced

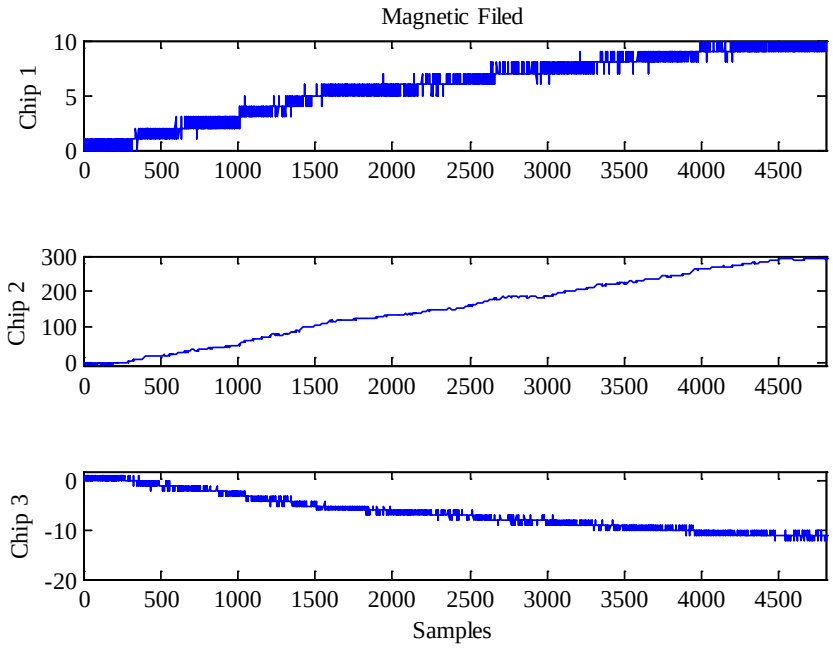

Figure 4-9: Readout of three chips when only piston 2 is displaced

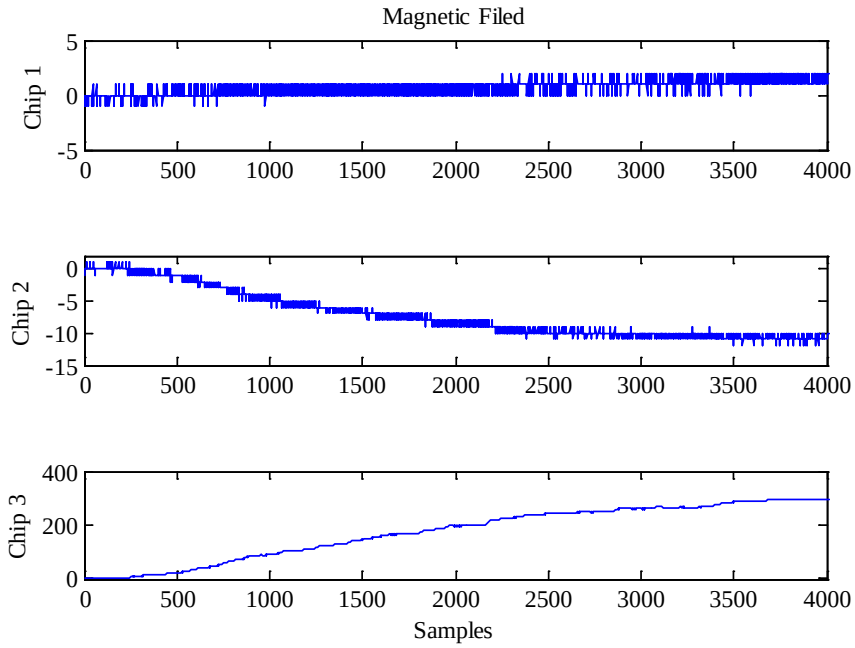

Figure 4-10: Readout of three chips when only piston 3 is displaced

For the distance between the two extreme slots equal to current design distance (= 20 mm), it was experimentally found that the cross coupling between the left (or right) magnet and the right (or left) chip is negligible. Further the direction of change depends on the relative polarity of the chip and the magnet. This section describes a method by which both numerator and denominator of the ratio, given by equation (4.9), can be estimated without any coupling terms

4.3.1 Elimination of coupling terms in the readout of center chip

Since magnetic field is additive, reading of chip 2 (R_2) is given by equation (4.14b), reproduced again in equation (4.15).

$$R_2 = k_1 B_0(y_1, d) + k_2 B_A(y_2) + k_3 B_0(y_3, d) \tag{4.15}$$

In order to eliminate the coupling terms from the readout, two additional magnetic sensing chips (Chip 4 and Chip 5) were placed on the circuit as shown in Figure 4-11. These chips were located so that the distance (d) between chip 1 (or chip 3) and chip 2 is same as that between chip 1 (or chip3) and chip 4 (or chip 5), however the distance

between chip 2 and chip 4 (or chip 5) is maximized to ensure that the effect of magnet 2 (located above chip 2) on chip 4 (or chip 5) is negligible.

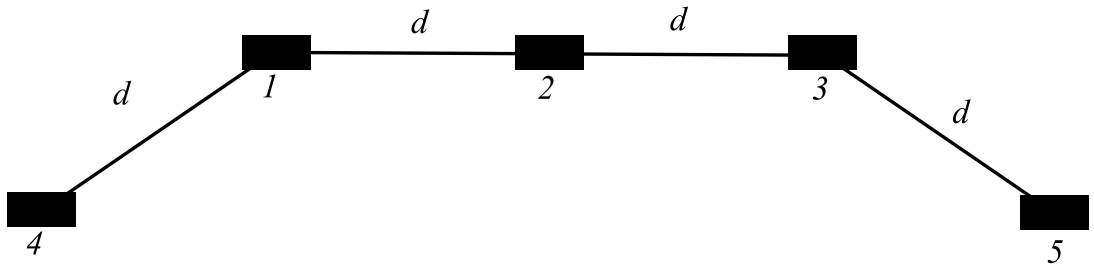

Figure 4-11: Modified circuit board to incorporate two additional magnets

Since by design, the additional chip 4 (chip 5) is only affected by magnet above chip 1 (chip 3), the readouts of these two additional chips (R_4 and R_5) are given by equation (4.16).

$$R_4 = k_1 B_0(y_1, d) \tag{4.16a}$$

$$R_5 = k_3 B_0(y_3, d) \tag{4.16b}$$

An estimate, expressed by equation (4.17), then provides the effect of magnet 2 on chip 2 without any coupling terms.

$$R_2 - R_4 - R_5 = k_2 B_A(y_2) \tag{4.17}$$

Figure 4-12 and Figure 4-13 provide an experimental verification of this methodology. When either of the side pistons is displaced, the reading of the center chip changes however there is no appreciable change in the readout of center after correction.

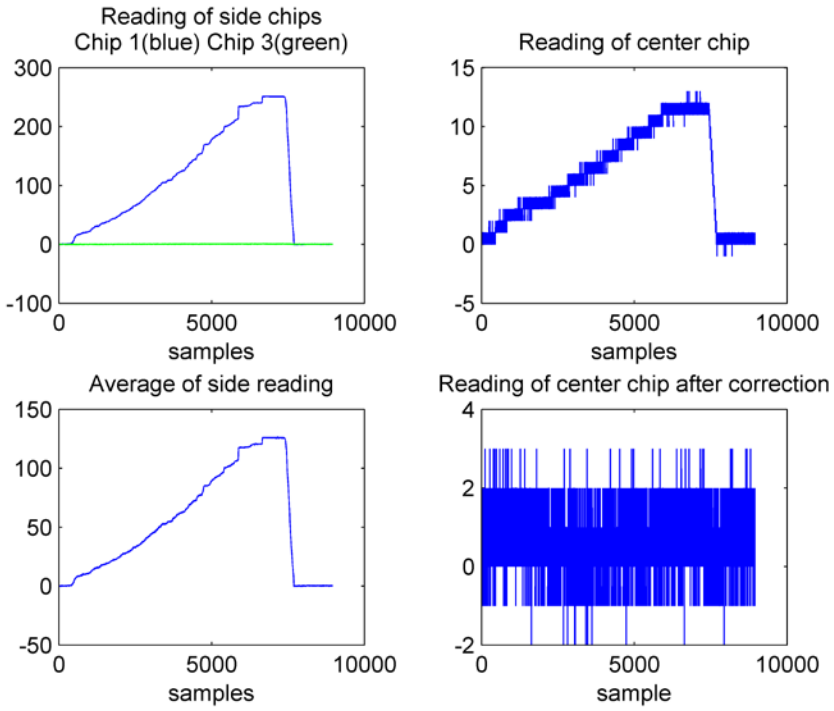

Figure 4-12: Corrected reading of center chip when piston 1 is displaced

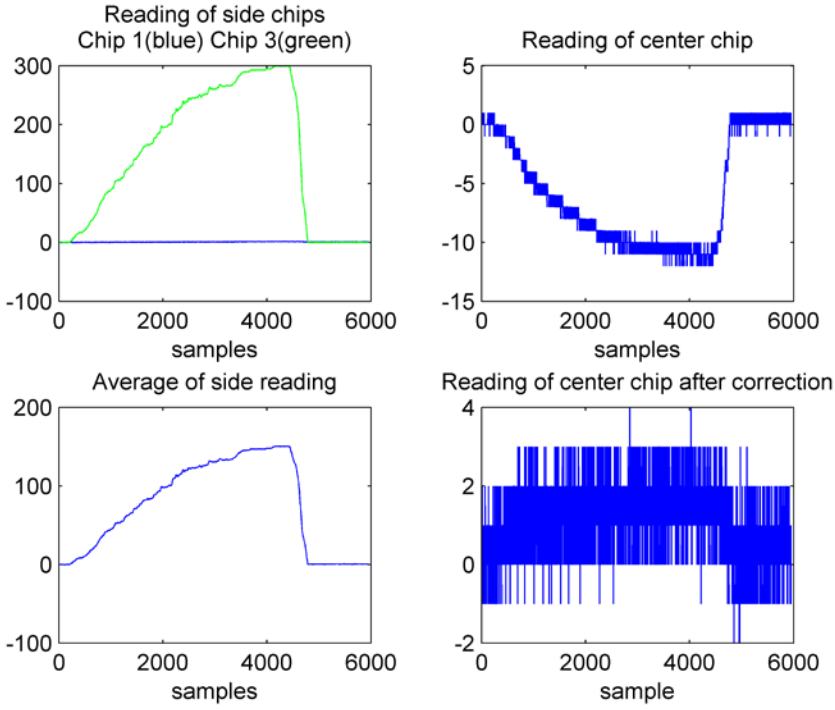

Figure 4-13: Corrected reading of center chip when piston 3 is displaced

4.3.2 Elimination of coupling terms in the readout of average of side chips

Equations (4.14a) and (4.14c), reproduced as equation (4.18), provide an expression for the reading of chip 1 and chip 3 respectively.

$$R_1 = k_1 B_{\mathrm{A}}(y_1) + k_2 B_0(y_2, d) + k_2 B_0(y_3, 2d) \tag{4.18a}$$

$$R_3 = k_1 B_0(y_1, 2d) + k_2 B_0(y_2, d) + k_3 B_{\mathrm{A}}(y_3) \tag{4.18b}$$

If sensors 1 and 2 are configured to read the proximity to south pole as positive and the magnet above them are positions so that the south pole of these magnets face these sensors, while the sensor 3 is configured to read the north pole as positive and magnet above it is positioned so that its north pole faces this sensor, then equation (4.18) can be modified and re-written as equation (4.19).

$$R_1 = k_1 B_{\mathrm{A}}(y_1) + k_2 B_0(y_2, d) - k_2 B_0(y_3, 2d) \tag{4.19a}$$

$$R_3 = -k_1 B_0(y_1, 2d) - k_2 B_0(y_2, d) + k_3 B_{\mathrm{A}}(y_3) \tag{4.19b}$$

The sum of these magnetic fields is given by equation (4.20).

$$\begin{aligned} R_1 + R_3 = {} & k_1 B_{\mathrm{A}}(y_1) + k_2 B_0(y_2, d) - k_2 B_0(y_3, 2d) - k_1 B_0(y_1, 2d) \\ & - k_2 B_0(y_2, d) + k_3 B_{\mathrm{A}}(y_3) \end{aligned} \tag{4.20}$$

It has been shown in Figure 4-8 and Figure 4-10 that there is negligible coupling between the extreme magnets; hence the terms involving $B_O(y_i, 2d)$ can be assumed as zero. Hence the equation (4.20) will be reduced to (4.21), which does not involve any coupling terms.

$$R_1 + R_3 = k_1 B_{\mathrm{A}}(y_1) + k_3 B_{\mathrm{A}}(y_3) \tag{4.21}$$

Figure 4-14 shows the readings of the different chips when the center piston is displaced, as can be seen that along with chip 2, the reading of chip 1 and chip 3 also change, however due to the opposite signs of the two changes, the change in average of the two is negligible as compared to the individual changes.

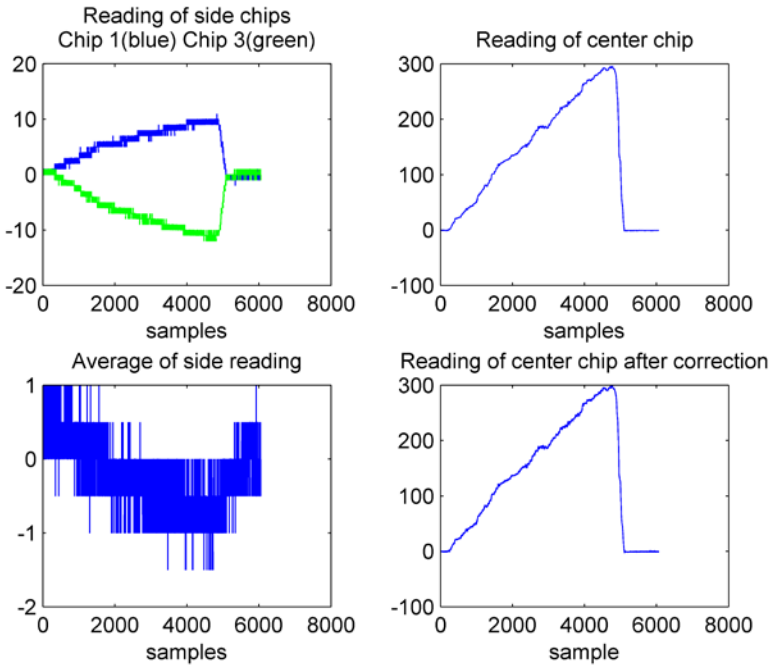

Figure 4-14: Average reading of side chips when piston 2 is displaced

The quantities given by equations (4.17) and (4.21) can be used as the numerator and denominator to estimate the ratio, given by equation (4.9), without any coupling terms.

This is a bold assumption which is not fully justifiable given the displacement and magnetic field has a non-linear relationship which is discussed in section 4.4.1 and is also shown in Figure 4-17. However given the complexity of non-linear relationship between the displacements of the three pistons and changes in magnetic field at the three sensors, it is not feasible to account for both the coupling effects and the non-linearity at the same time. A comparison between using displacement and magnetic field has been presented in section 4.3.3 using data generated by simulating the system in Matlab to illustrate that using magnetic field data instead of displacement still provides a similar monotonic relationship between the estimated ratio and the tension.

4.3.3 Simulated sensor response using magnetic field instead of displacement

A simulation study was conducted in Matlab to analyze the effect of using the change in magnetic field data obtained directly from the chip instead of using the displacement data.

At the start of the simulation, the sensor was assumed to be in contact with the string with no force being exerted on the string. During the simulation, the sensor was then moved forward in increments of 0.1 mm and the expected values of the compressions were calculated using equation (4.6). The expected compression values were then converted into expected change in magnetic field as obtained from the hall-effect sensors using equations (4.14) and (4.16). The sensor's forward movement was continued till the average of readings from side sensors exceeded 150 counts. The values of the various parameters used for this simulation are shown in Table 4-1, these values were the design values except for the strength of permanent magnets which was estimated by fitting a model to data presented in Figure 4-17.

Table 4-1: Parameter values used for simulation

Parameter	Description	Value
l	Length of string	76.2 mm (= 3 inches)
x_2	Position of center sensor from end of string	38.1 mm (=1.5 inches)
d	Pitch of hall effect sensors	10 mm
k	Strength of permanent magnets	40000
y_0	Initial distance between magnets and chips	6.3 mm

Figure 4-15 shows the expected values of displacement and change in magnetic field obtained for 40 N and 80 N tensions.

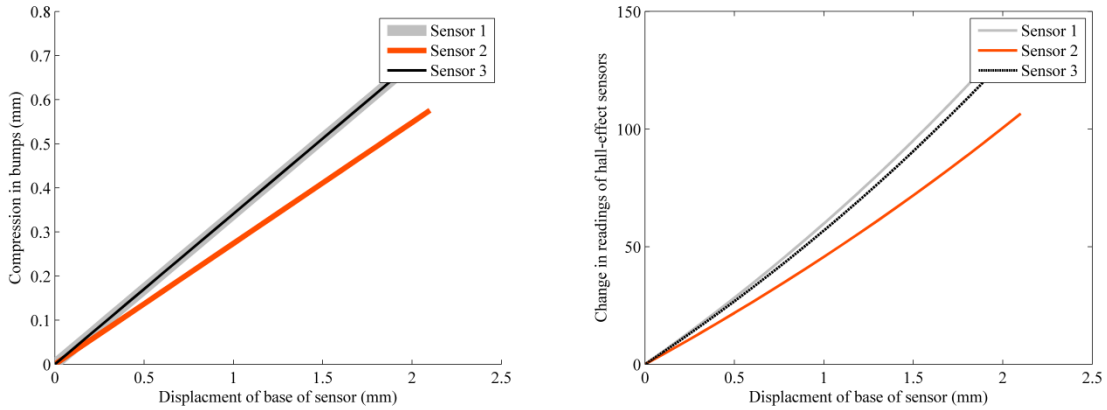

Simulated data for 40 N tension

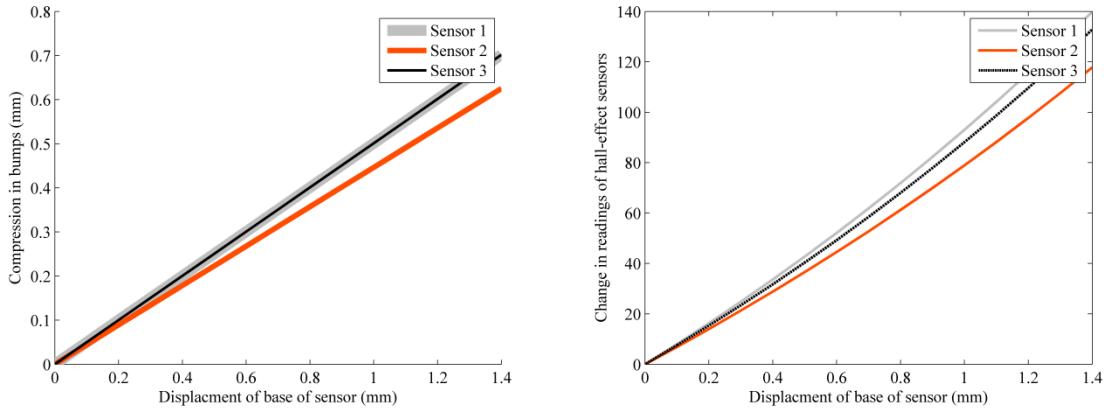

Simulated data for 80 N tension

Figure 4-15: Simulated compression and magnetic field data

An ordinary least square line, given by (4.22), was then fit using average of side readings as the x values and the center reading as y values. Such an exercise was conducted using both the expected displacement, given by equation (4.6) as the readings and also using change in magnetic field obtained using equations (4.14) and (4.16). The obtained value of the slope (β_1) was used as the response of the sensor in lieu of the ratio described by equation (4.9). Figure 4-16 shows the response of the sensor obtained for different tension values in both the case. Using change in magnetic field in place of displacements results in a very similar response curve and hence justifies the use of magnetic field to eliminate the cross coupling effects of the different magnets as described in section 4.3.2.

$$y = \beta_0 + \beta_1 x \tag{4.22}$$

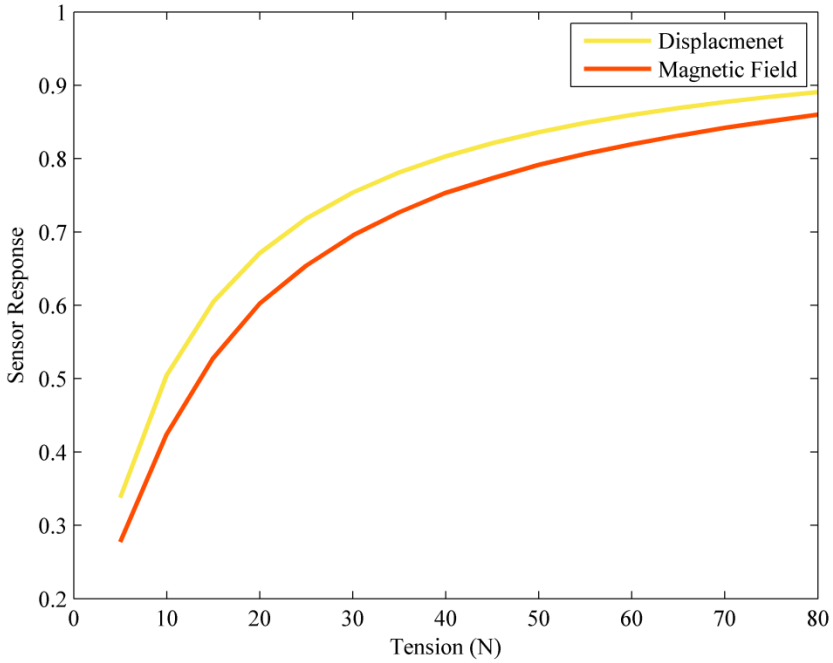

Figure 4-16: Simulated comparison of sensor response when using magnetic field data

4.4 CHARACTERIZATION OF SENSOR ELEMENTS

The characterization of each bump assembly of the sensor was performed by applying known displacement (or force) to one piston at a time and measuring the change in the readout of the Hall-effect sensor under that piston.

4.4.1 Characterization under known displacement

To characterize the response of the bump assemblies as a function of compression, known displacement, varying between 0 mm to 3 mm, were applied to each of the pistons (one at a time) using a micrometer screw gauge in steps of 0.254 mm (.01 inch). The process was repeated thrice to test the repeatability.

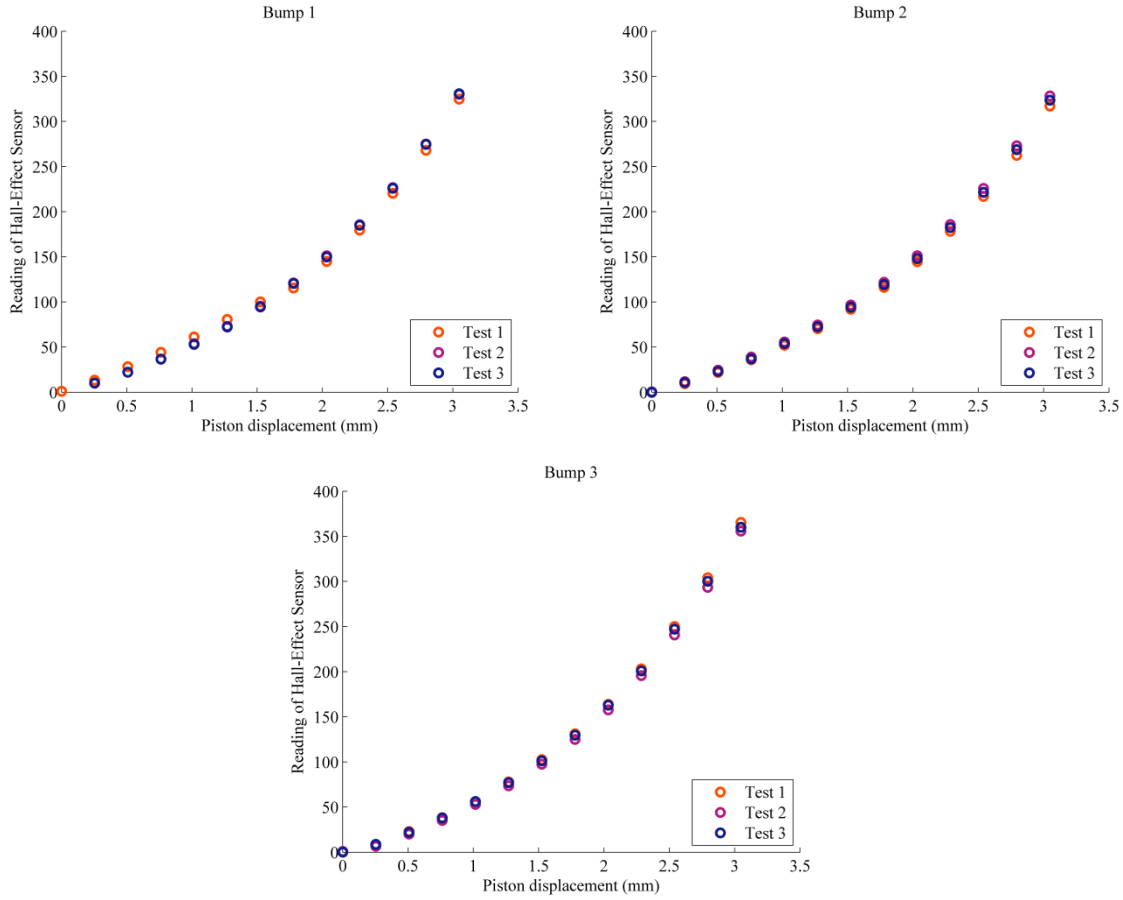

Figure 4-17: Displacement vs Magnetic field calibration curves for magnetic sensor

Figure 4-17 show the response of the three bump assemblies. It can be seen from the three curves that the response of the bump assemblies to the compression was repeatable, however as expected was nonlinear.

4.4.2 Characterization under known force

To characterize the response of the bump assemblies as a function of applied force, known forces, in the range 0 N to 5 N, were applied to each of the pistons using a force gauge of 5N range (Model HP-5 from Handpi TM) as shown in Figure 4-18. The process was repeated thrice to test the repeatability.

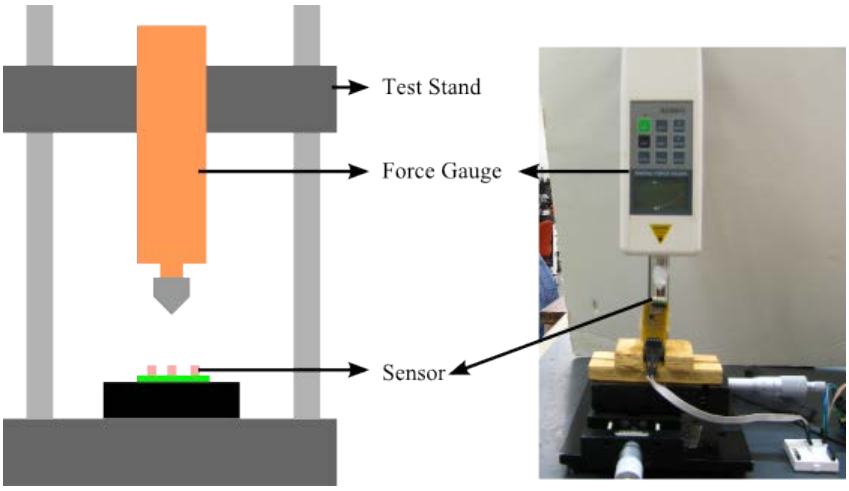

Figure 4-18: Setup used for calibrating magnetic sensor for known forces

Figure 4-19 show the response of the three bump assemblies. It can be seen from the three curves that the response of the bump assemblies to the applied force was repeatable.

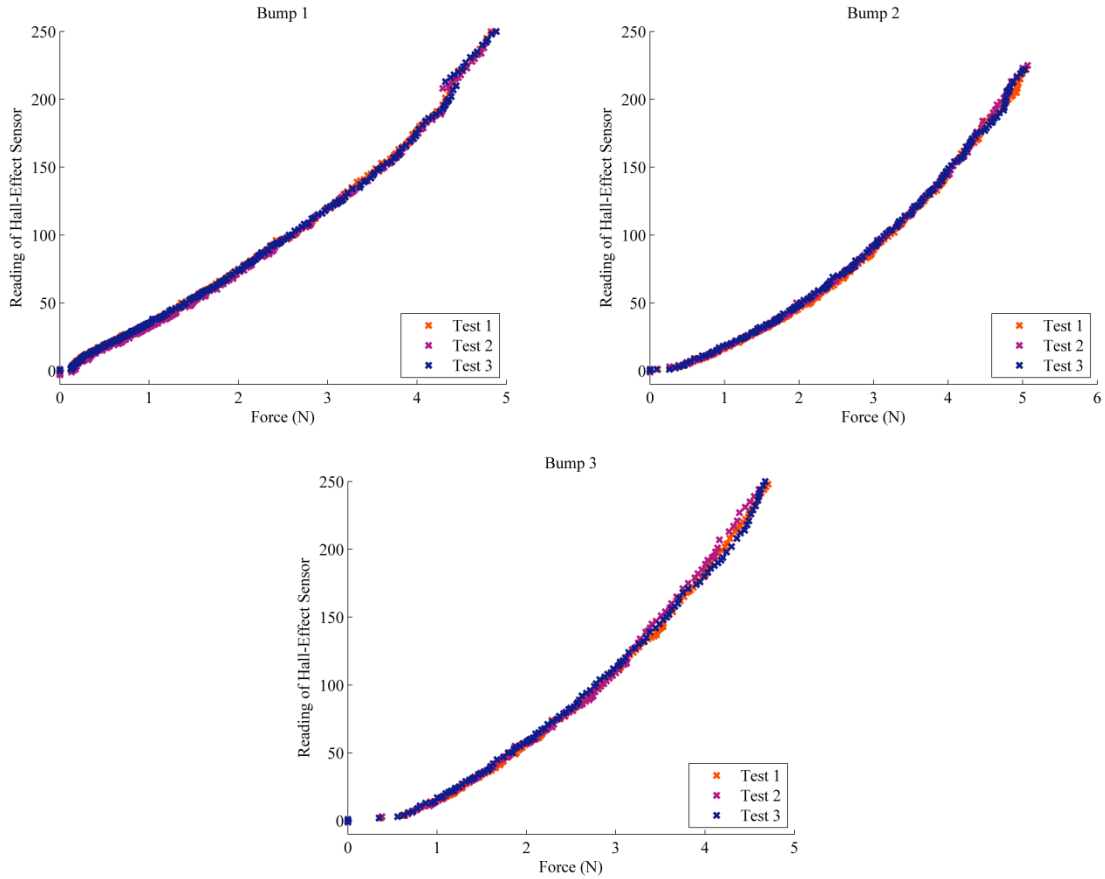

Figure 4-19: Force vs Magnetic field calibration curves for magnetic sensor

4.5 EXPERIMENTAL RESULTS WITH SYNTHETIC STRING

A nylon lace of width 1 cm was used to test the performance of the sensor. A photograph of the lace is shown in Figure 4-20.

Figure 4-20: Photograph of the lace

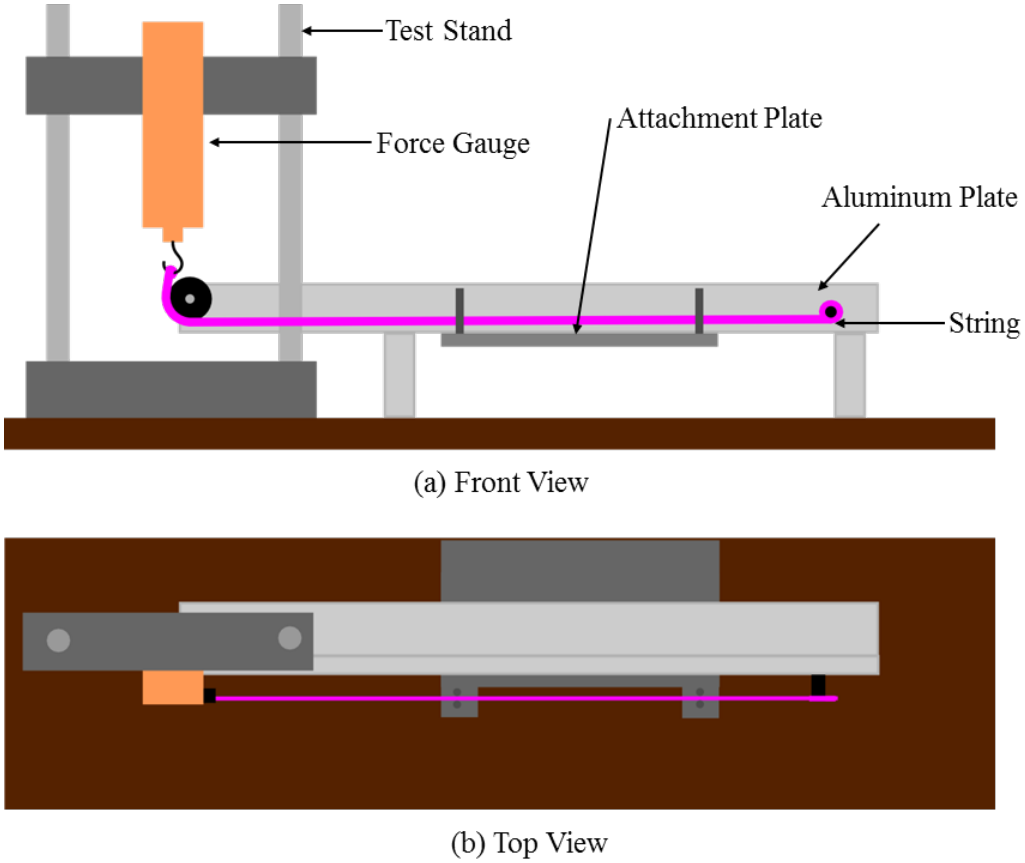

Figure 4-21: Schematic of Test Setup

An experimental setup was designed to apply known tensions to this nylon lace. Figure 4-21 and Figure 4-22 shows the schematic and photograph of the setup which was used to test the sensor for known tension values. The setup consists of a force gauge of 200 N range (HP-200 from Handpi TM) mounted on a vertical test stand. The nylon lace was tied to one end of the setup and was routed through a pulley on the other side to the force gauge. The height of the test stand was adjusted to change the tension in the lace. The string was routed through an attachment plate as shown in Figure 4-23 to control the free length of the string against which the sensor was pushed. The attachment plate shown in this figure constraints the free length of the string to 3 inches (= 76.2 mm).

Figure 4-22: Photograph to experimental setup

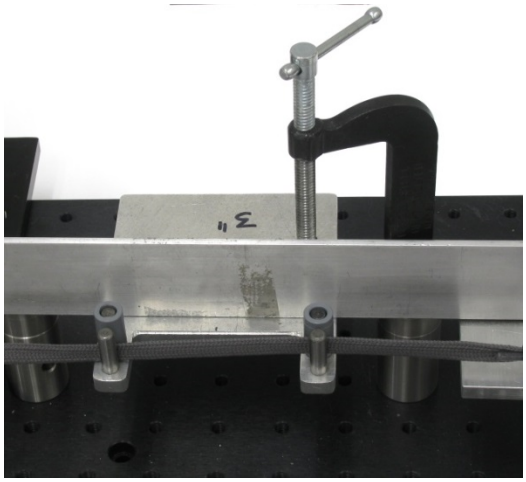

Figure 4-23: Attachment plate for setting free length

4.5.1 On-stage testing with fixed orientation

For the initial set of testing, the sensor was mounted on a $x-y$ translation stage as shown in Figure 4-24. The translation stage was used to ensure that the orientation of the sensor with respect to the lace remains constant. It was ensured that a normal contact occurs between the sensor and the string by visually adjusting the angle of the attachment plate and sensor. Furthermore the sensor was positioned so that the center piston comes into contact with the free length of the string at approximately its mid-point.

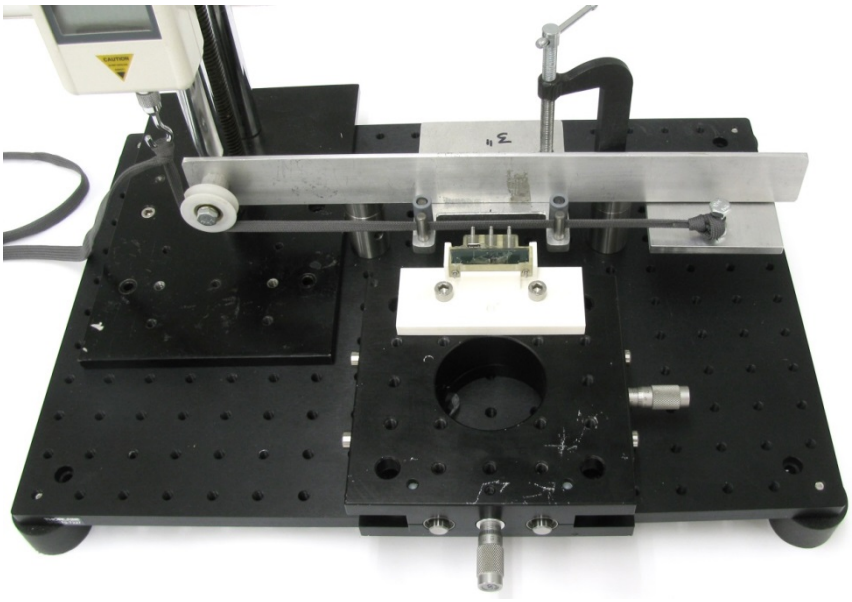

Figure 4-24: Magnetic sensor mounted on a translation stage

Figure 4-25 shows the plot of center bump reading vs. the average of readings from side bumps for three different tension values. The center and side readings show a linear trend for each tension as predicted by the equation (4.9). Also the slope of the line increases with increase in tension.

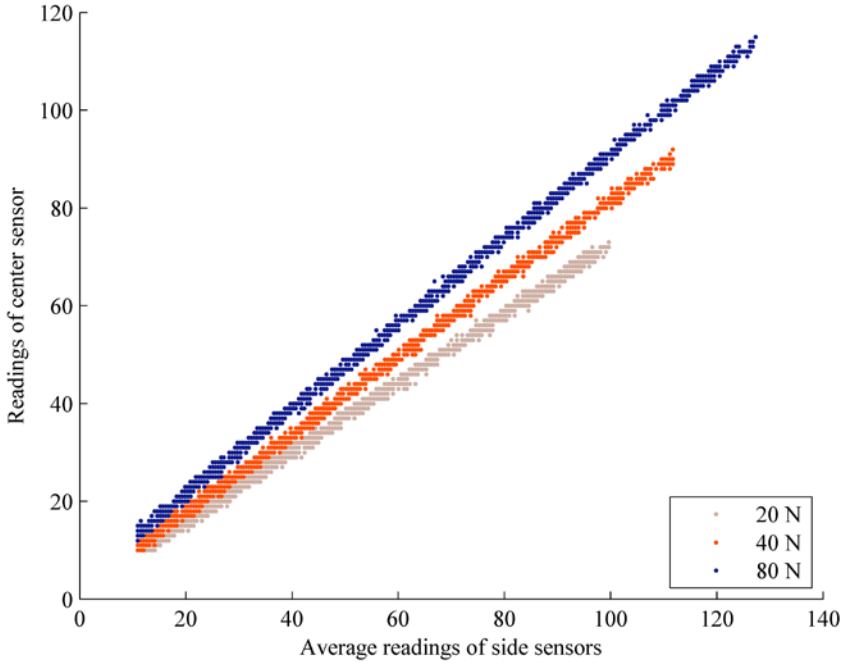

Figure 4-25: Sensor response for three different tension values

The slope of that line was estimated by fitting an ordinary least squares (OLS) line to the data. The equation of the OLS line is given by equation (4.23), where x the average readings of the side sensors, y is the reading of the center sensor and ϵ is the error.

$$y_i = \hat{\beta}_0 + \hat{\beta}_1 x_i + \epsilon_i \tag{4.23}$$

Figure 4-26 shows the OLS fitted line for different tension values. It can be seen that the slope of the line consistently increases with the increase in tension as predicted by equation (4.9). The R^2 values for the OLS fit were typically found to be greater than 0.995.

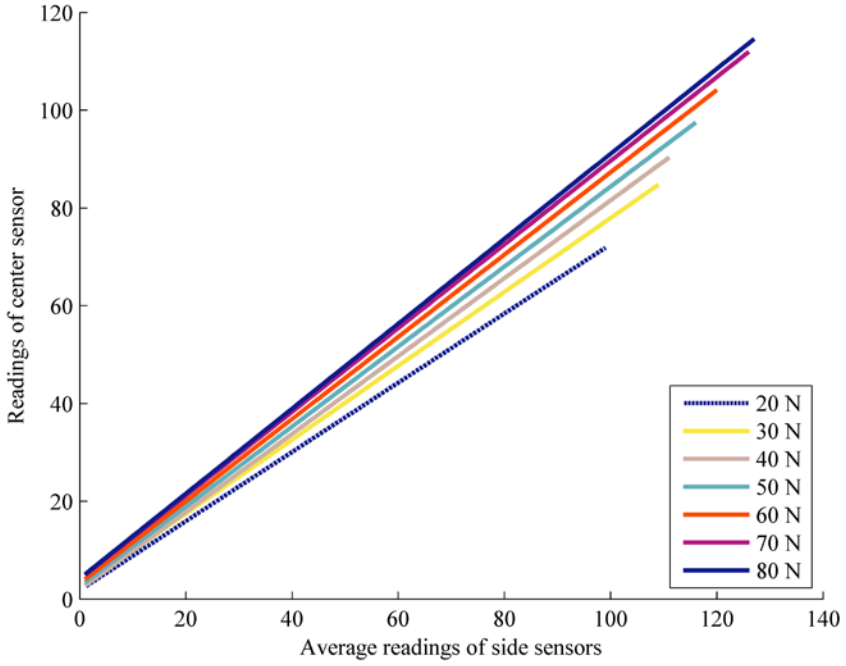

Figure 4-26: Fitted line for different tension values

The OLS line fitting using equation (4.23) assumes that the values of x are observed without any error, however in this case since both x and y are the readings obtained from similar sensors there error variances could be of same order. It can be shown that the slope estimate obtained from OLS of y on x ($\hat{\beta}_{yx}$) and that obtained by OLS of x on y ($\hat{\beta}_{xy}$) follow a relationship given by equation (4.24), where R^2 is the coefficient of determination. Furthermore all the available solutions would lie within the interval $[\hat{\beta}_{yx}, 1/\hat{\beta}_{xy}]$ (or $[1/\hat{\beta}_{xy}, \hat{\beta}_{yx}]$) [38]. Since the observed R^2 values were found to be large (typically > 0.995), the error in x was ignored and OLS estimate slope of equation (4.23) was assumed to be the sensor's response.

$$\hat{\beta}_{yx}\,\hat{\beta}_{xy} = R^2 \tag{4.24}$$

To further evaluate the OLS fitting, the residuals of the fitted line were analyzed. Figure 4-27 shows a plot of the residuals against the fitted y values for a one test conducted at different tension values, since the magnitude of the residuals does not show any systematic dependence on the fitted values; we can conclude that the system is homoscedastic. Figure 4-28 and Figure 4-29 shows the q-q plot and histograms of the residuals for the same tests, these two plots visually confirm the normality of the residuals.

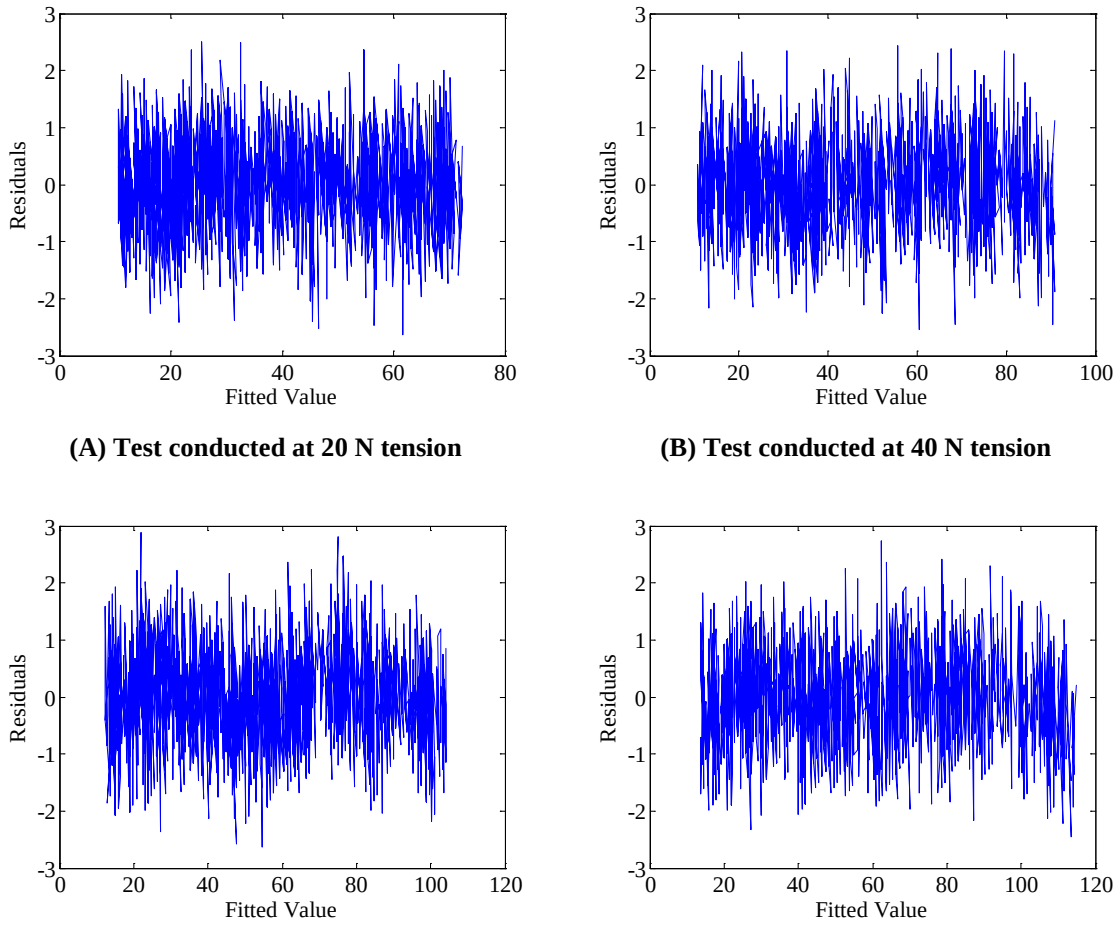

(A) Test conducted at 20 N tension

(B) Test conducted at 40 N tension

(C) Test conducted at 60 N tension

(D) Test conducted at 80 N tension

Figure 4-27: Residuals vs fitted values

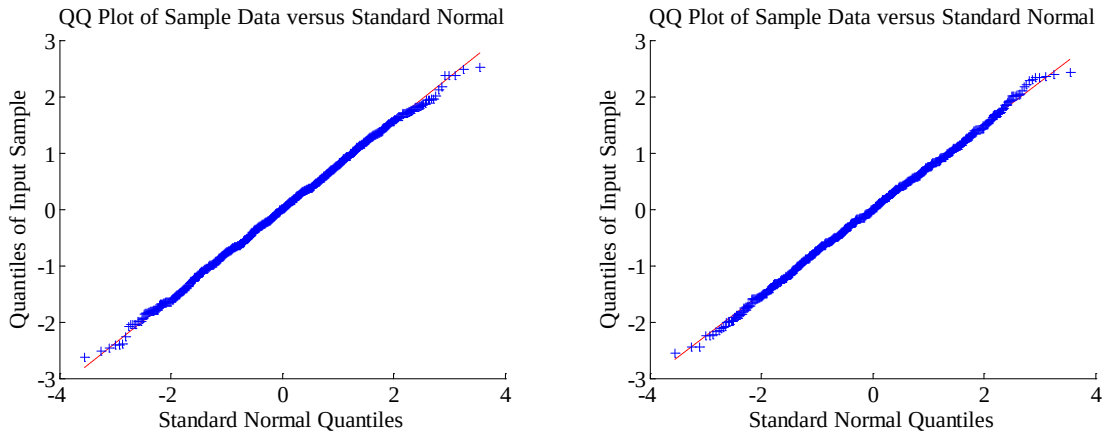

(A) Test conducted at 20 N tension **(B) Test conducted at 40 N tension**

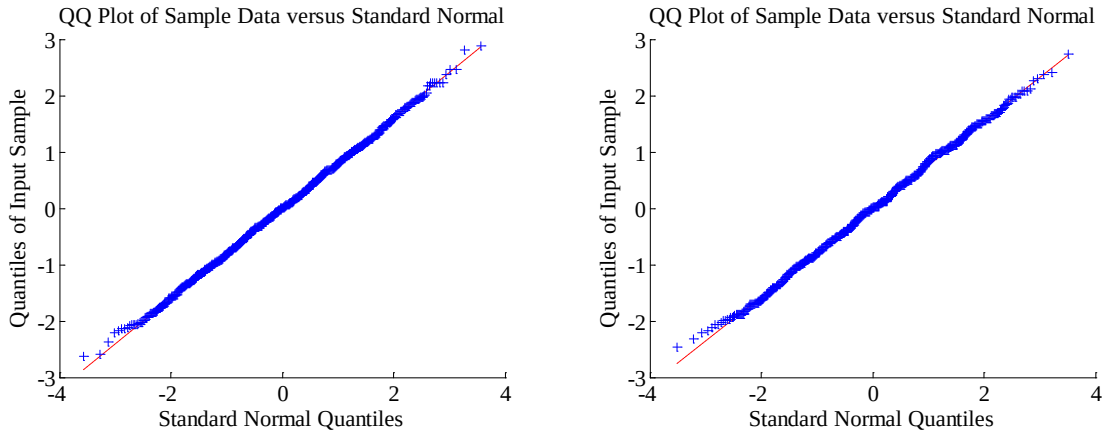

(C) Test conducted at 60 N tension **(D) Test conducted at 80 N tension**

Figure 4-28: QQ plot of residuals

The sensor was tested at various tension values varying between 20 N to 80 N in increments of 10 N. Each set of test consists of 10 individual tests at each tension value, where each test comprises of one push of the sensor against the string using the setup shown in Figure 4-24. Three such sets (a total of 30 individual tests at each tension) are shown in Figure 4-27. The plot shows a good agreement between the three sets.

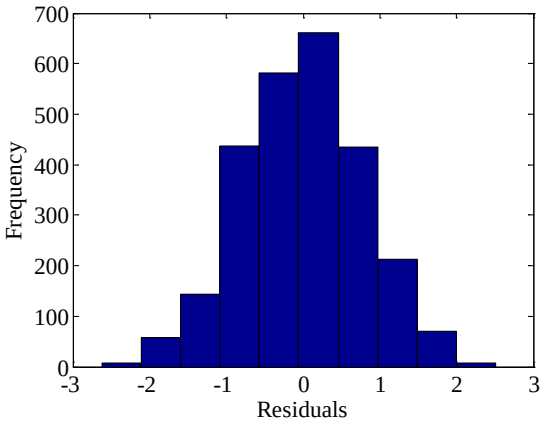

(A) Test conducted at 20 N tension

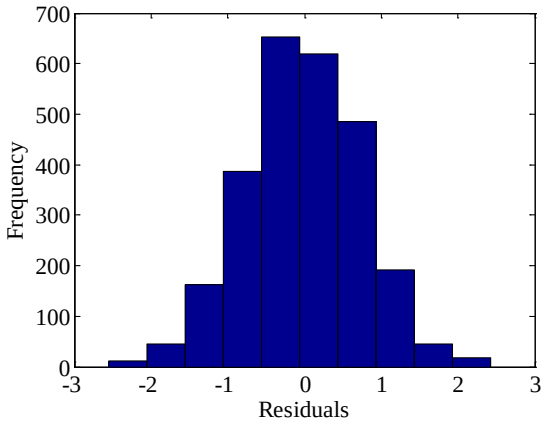

(B) Test conducted at 40 N tension

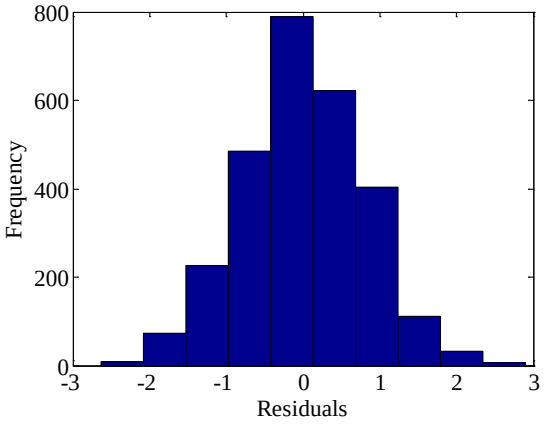

(C) Test conducted at 60 N tension

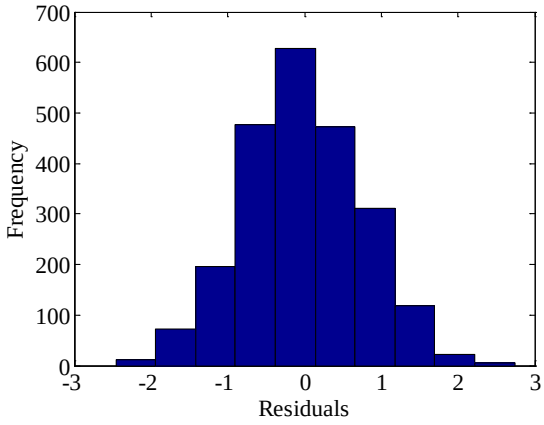

(D) Test conducted at 80 N tension

Figure 4-29: Histogram of residuals

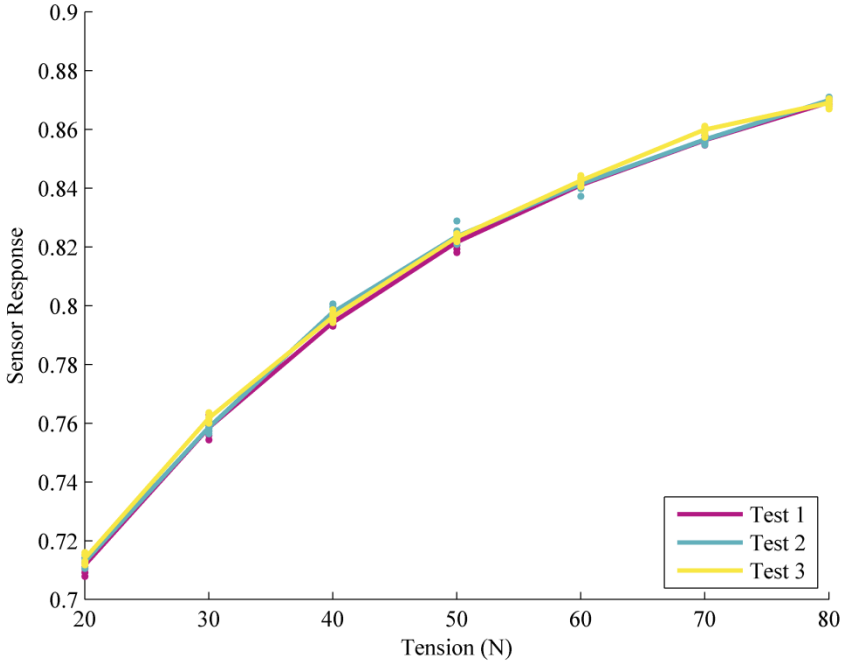

Figure 4-30: Sensor response for controlled orientation

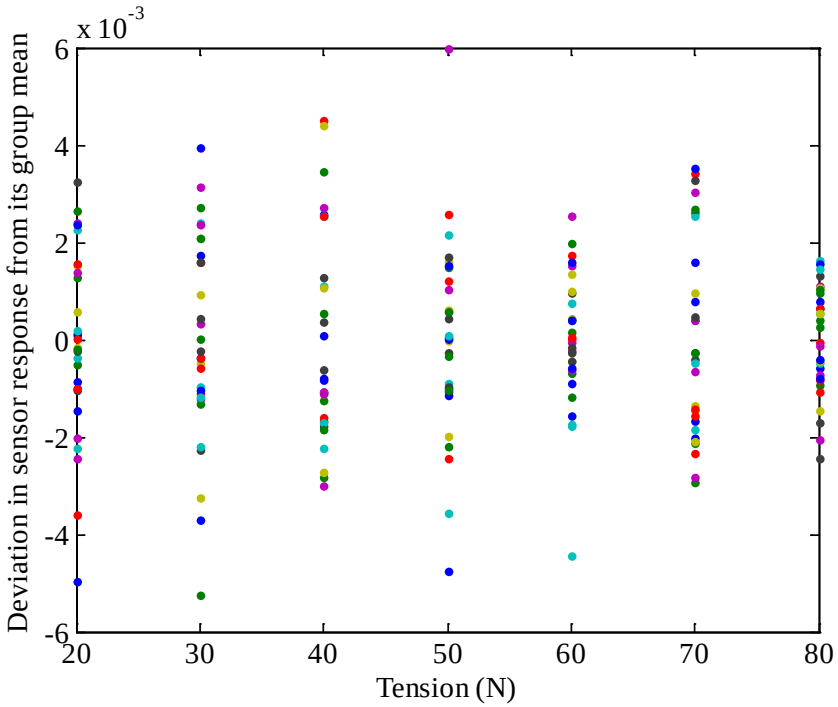

Figure 4-31: Deviation in sensor response from its group mean for controlled orientation

The deviation of the sensor responses from the mean response for that particular tension values is shown in Figure 4-31. On visual inspection, the plot does not reveal any systematic change in variance of the deviations with the tension, indicating a homoscedastic system. The overall standard deviation of these errors was found to be 0.0018.

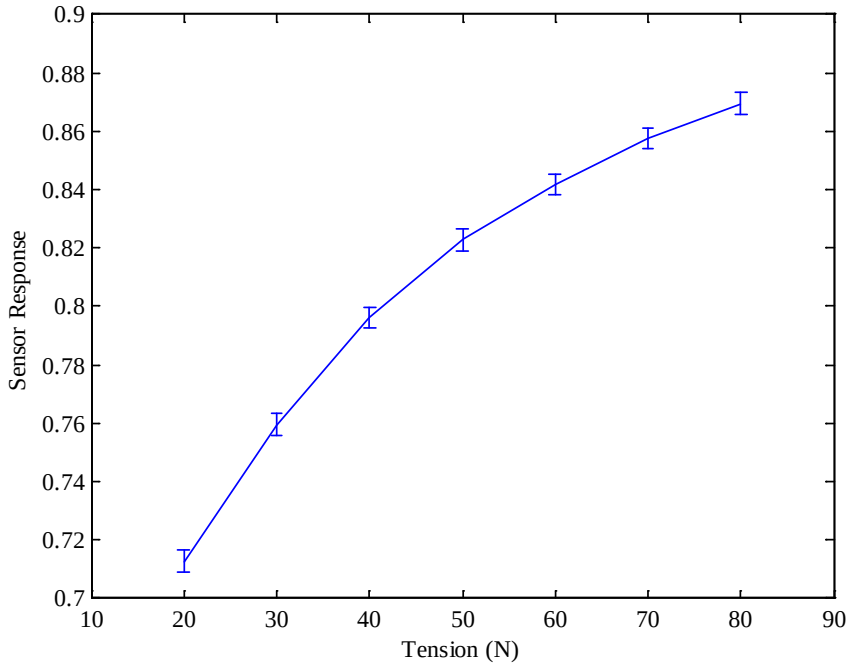

Figure 4-32: Mean response of sensor for controlled orientation

Figure 4-32 shows the mean value of the sensor response along with an error bar corresponding to the expanded uncertainty with a coverage factor of 1.96 (corresponding to 95% level of confidence) as defined by National Institute of Standards and Technology (NIST) [39]. The expanded uncertainty (U), defined by equation (4.25), is a value such that it can be confidently believed that the measured value Y lies between $y \pm U$, where y is the measurement result, k is the coverage factor chosen on the basis of the desired level of confidence and u_c is a reliable estimate of the standard deviation of y. With the desired level of confidence as 95%, the sensor was found to have a resolution better than 10 N, i.e. there was no overlap between the error bars shown in Figure 4-32.

$$U = k\,u_c \tag{4.25}$$

4.5.2 Handheld testing

A handle was designed and fabricated using 3-D printing for ease of holding the sensor while handheld testing. Figure 4-33 shows a photograph of the sensor attached to the handle. The sensor was tested at various tension values varying between 20 N to 100 N in increments if 10 N. Each set of test consists of 10 individual tests at each tension value, where each test comprises of one push of the sensor against the string using the setup shown in Figure 4-22. The mean of three such sets (a total of 30 individual tests at each tension) along with the mean of the three tests from section 4.5.1 are shown in Figure 4-34. The responses were found to be in agreement with each other, thus making the sensor a viable tool for handheld tension measurement.

Figure 4-33: Photograph of handheld magnetic sensor

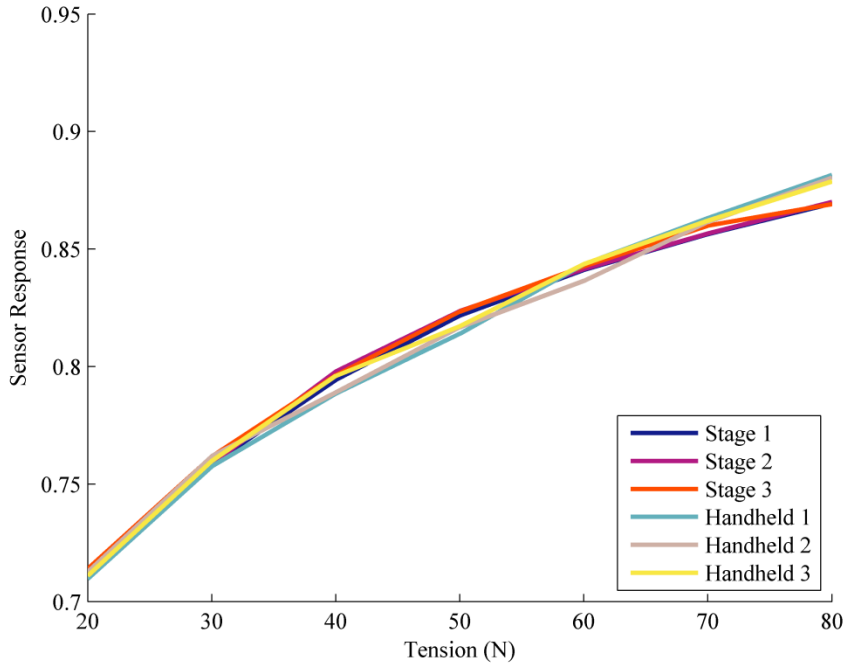

Figure 4-34: Comparison of Sensor response for handheld and on-stage testing

Figure 4-35 shows the mean response of the ten tests in each handheld group along with the spread in the response for tensions varying between 20 N and 100 N. The deviation of the sensor responses from the mean response for that particular tension values is shown in Figure 4-36. On visual inspection, the plot does not reveal any systematic change in variance of the deviations with the tension, indication a homoscedastic system. The overall standard deviation of these errors was found to be 0.0066, which is approximately 3.6 times that found for controlled orientation in section 4.5.1.

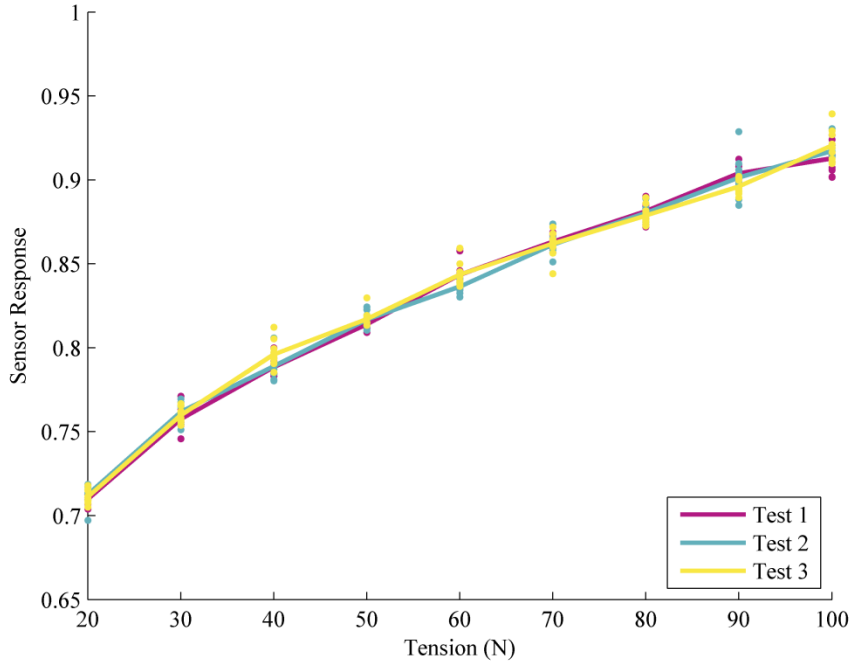

Figure 4-35: Sensor response for handheld testing

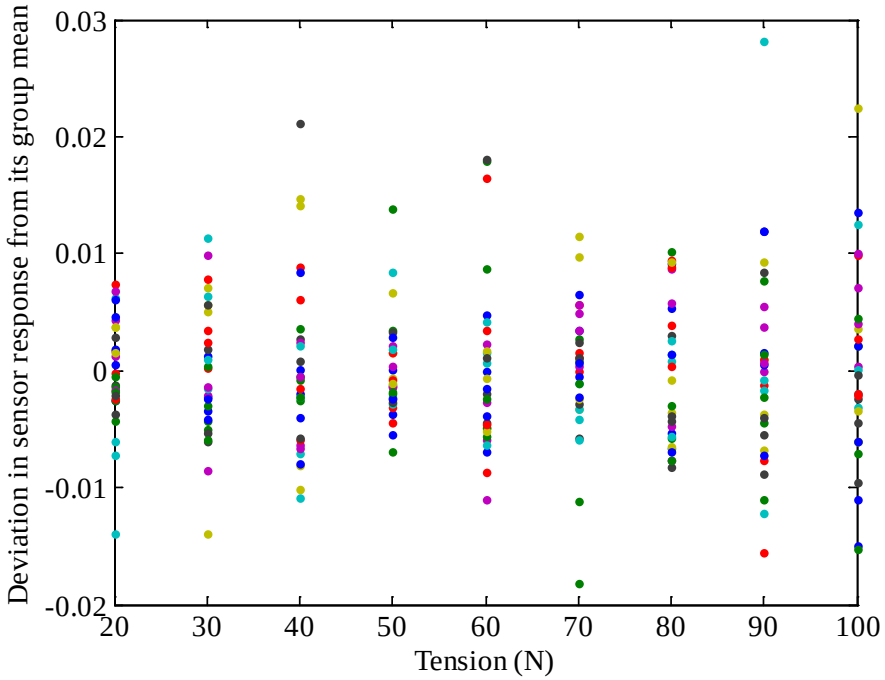

Figure 4-36: Deviation in sensor response from its group mean for handheld testing

Figure 4-37 shows the mean value of the sensor response along with an error bar corresponding to the expanded uncertainty with a coverage factor of 1.96 (corresponding to 95% level of confidence) as defined in section 4.5.1. With the desired level of confidence as 95%, the sensor did not have a resolution of 10 N for tension values greater than 40 N.

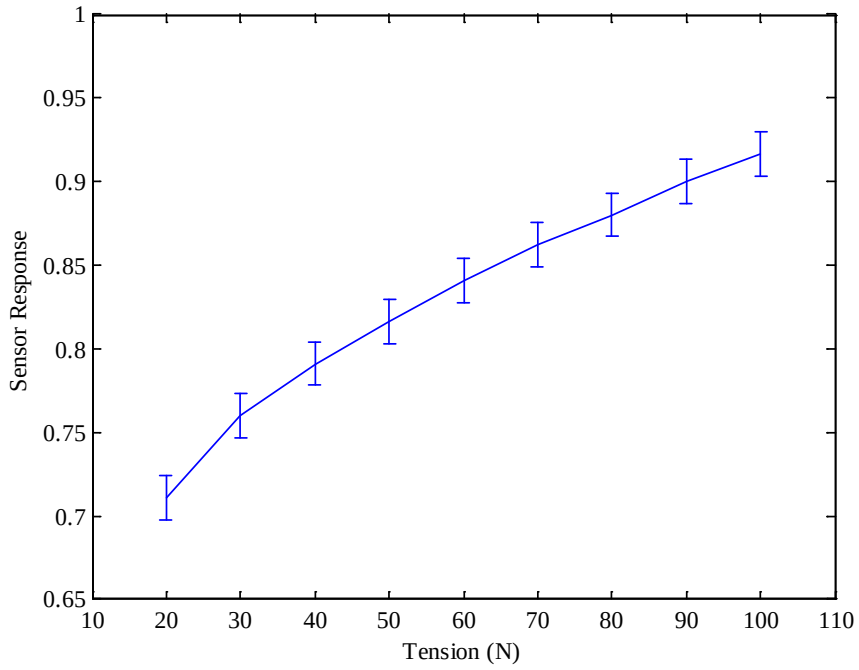

Figure 4-37: Mean response of sensor for handheld tests

In order to achieve a 10 N resolution throughout the range, the expanded uncertainty, as defined by equation (4.25), for 95% level of confidence should be less than the difference between the mean readouts of each pair of consecutive group. Table 4-2 list the mean sensor response for different tension values. The minimum difference between consecutive values occurs between 90 N and 100 N and is equal to 0.0163. An expanded uncertainty of less than 0.0163 at 95 % level of confidence corresponds to a required standard deviation of less than 0.0042.

Table 4-2: Mean sensor response for different tensions

Tension (N)	Mean sensor response
20	0.7111
30	0.7597
40	0.7912
50	0.8160
60	0.8412
70	0.8623
80	0.8802
90	0.9005
100	0.9168

The temporal trend of the deviations of the sensor response from the mean response for that particular tension is shown in Figure 4-38, since there is no observable temporal trend, the individual tests can be assumed to be independent of each other.

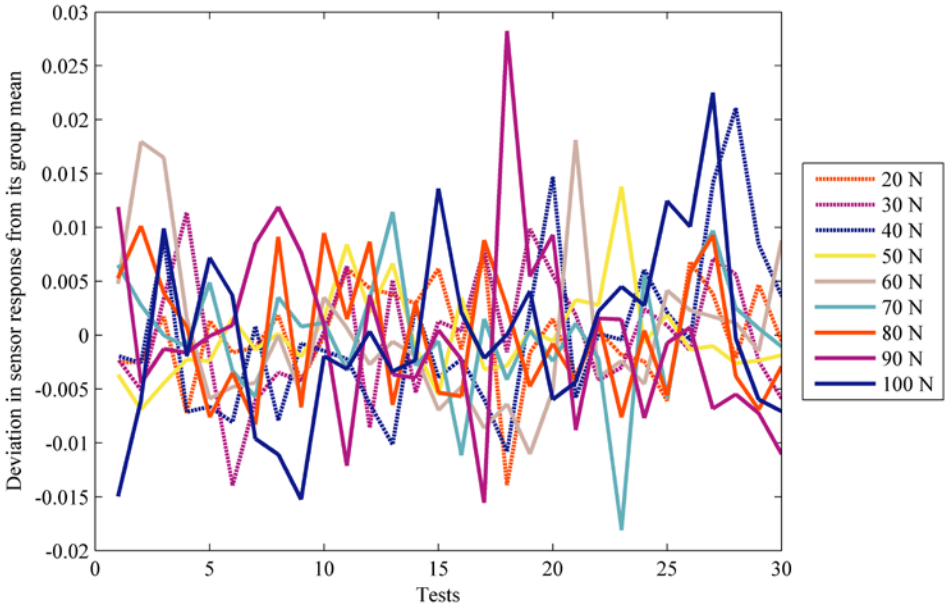

Figure 4-38: Temporal trend of the deviations of the sensor for hand held sensor

For independent observations of a random variable X, the relationship between the standard deviation of X (σ_X) and the standard deviation of the mean of n independent

observations $\bar{X}$ ($\sigma_{\bar{X}}$) is given by equation (4.26). Thus one method of obtaining the desired resolution could be to take an average of n handheld readings such that the standard deviation of the mean of those readings is less than the required threshold.

$$\sigma_{\bar{X}} = \frac{\sigma_X}{\sqrt{n}} \tag{4.26}$$

For the observed data it was found that the expected standard deviation of the mean of 3 observations would be 0.0038 which is less than the standard deviation required for a 10 N resolution. The actual standard deviation for a mean of three consecutive tests for the observed data was found to be 0.0043, which leads to a 10 N resolution for tension values up to 90 N.

Table 4-3: Sensor response for three users

Tests	User 1	User 2	User 3
1	0.8593	0.8296	0.8287
2	0.8373	0.8287	0.8542
3	0.8388	0.8274	0.8318
4	0.8367	0.8365	0.8272
5	0.8454	0.8364	0.8424
6	0.8435	0.8419	0.8346
7	0.8429	0.8486	0.8351
8	0.8423	0.8541	0.8434
9	0.8397	0.8435	0.8653
10	0.8500	0.8438	0.8439
Mean	**0.8436**	**0.8390**	**0.8407**
$\boldsymbol{\sigma}$	**0.0068**	**0.0086**	**0.0119**

It should however be noted that the value of n depends upon the standard deviation of individual tests. The standard deviation of individual tests depends upon the multiple factors like change of relative orientation between the sensor and string from test to test, which would depend upon the experience of the user with the sensor. Table 4-3 shows the sensor responses for ten tests conducted by three different users at a tension of 60 N.

User 1 is the author of the dissertation, and can be considered to have prior experience with the sensor; the other two users were first time users of the sensor with no prior experience.

As can be seen from the table, the means of the ten responses for all the three users are similar; however the standard deviations of the responses are different. For the three users listed below, the number of tests required will be 3, 5 and 8 respectively, thus for practical implementation the number of tests required would have to be an adaptive parameter. One such adaptive technique could be to ask users to take data till the standard deviation of their readings divided by the square root of the number of tests becomes less than a certain threshold, as the same time a level of confidence associated with the tests could be presented to the user after each individual test so that user has an option to stop testing once he/she is satisfied by the level of accuracy.

4.6 EXPERIMENTAL RESULTS WITH BIOLOGICAL TISSUE

The performance of the sensor was evaluated on tendons acquired from turkey euthanatized for causes unrelated to this study. The specimen was wrapped in saline soaked gauge and was stored frozen (at -20°C) until dissection prior to testing. Figure 4-39 shows the tendon/bone preparation for testing. The claw of the turkey along with some residual bone was casted using a casting resin.

The prepared sample was mounted on an optical table as shown in Figure 4-40(a). The casted bone was clamped down on the table, while the free end of the tendon was held in a serrated grip attached to a force gauge. The force gauge was mounted on a test stand whose height could be adjusted to adjust tension in the tendon. The sensor was mounted on a translation stage which was fixed on the optical table such the orientation of the sensor with respect to the tendon was approximately normal, as shown in Figure 4-40(b).

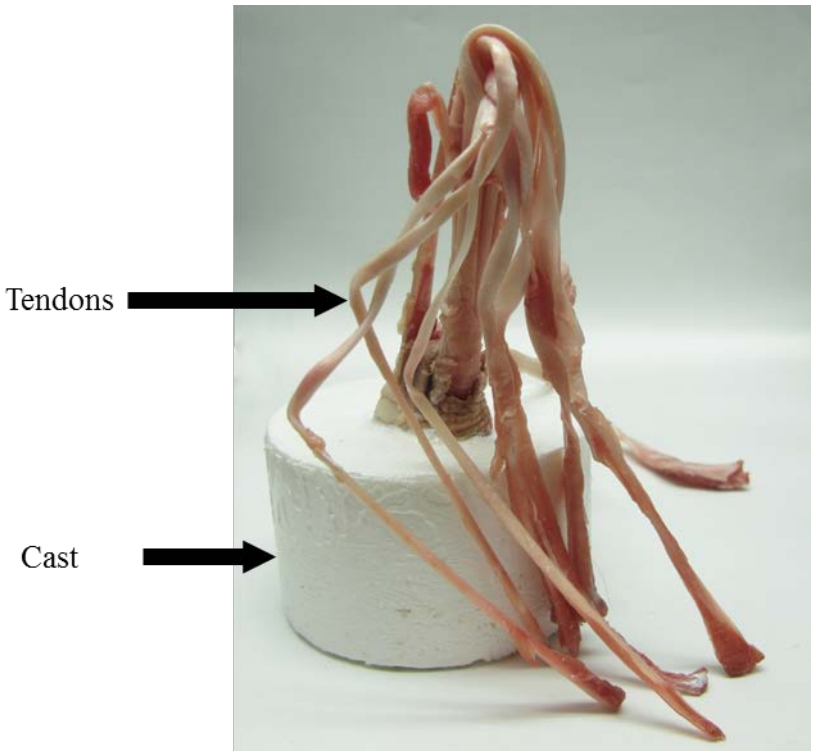

Figure 4-39: Casted turkey foot for testing

(a) Experimental setup with turkey tendon (b) Zoomed in sensor

Figure 4-40: Experimental setup with turkey ligament

The tendon was pre-stretched to a 100 N tension and the tension was slowly lowered to 20 N in 10 N intervals. Ten tests were performed at each tension value by pushing the sensor against the tendon till the average of side readings exceeded 100 counts. Two such set of experiments were conducted with the same ligament one after the other. Figure 4-41 shows the mean sensor response for the ten tests at each tension values for both set of tests. A good agreement was observed between the two set of experiments.

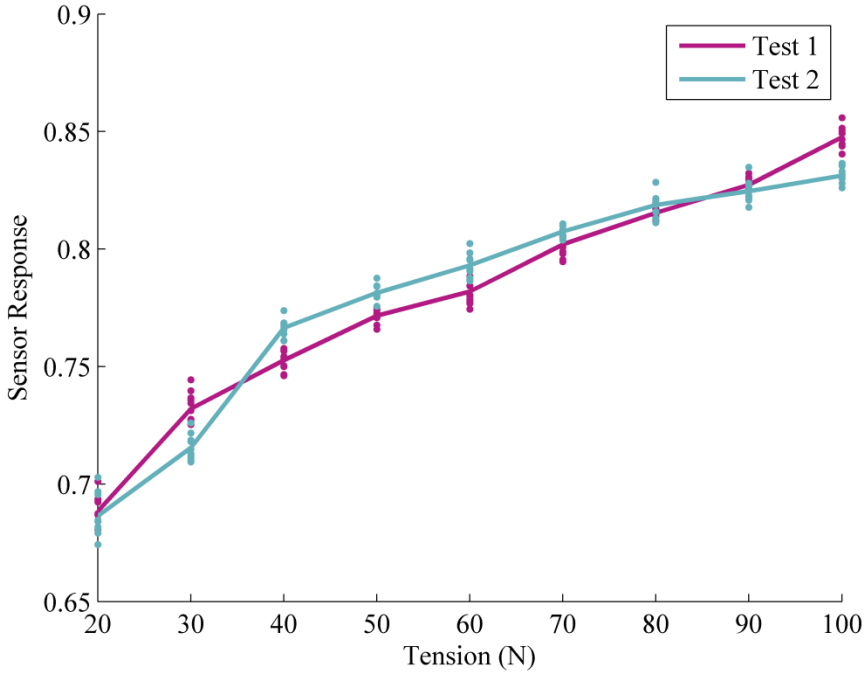

Figure 4-41: Sensor response vs applied tension for turkey tendon

4.7 SENSITIVITY ANALYSIS OF THE SENSOR

A theoretical and experimental sensitivity analysis was performed to evaluate the effects of length of the string and position of contact of the sensor along the string on the sensor response. For the purpose of theoretical sensitivity analysis, a simulated sensor response was obtained using a process similar to the one used in section 4.3.3.

4.7.1 Length of string

The simulated response of the sensor for three different free length of the string is shown in Figure 4-42. While estimating the simulated response, it was assumed that the middle bump of the sensor makes contact at the mid-point of the string. As predicted by equation (4.24) it does not depend upon the length of the string.

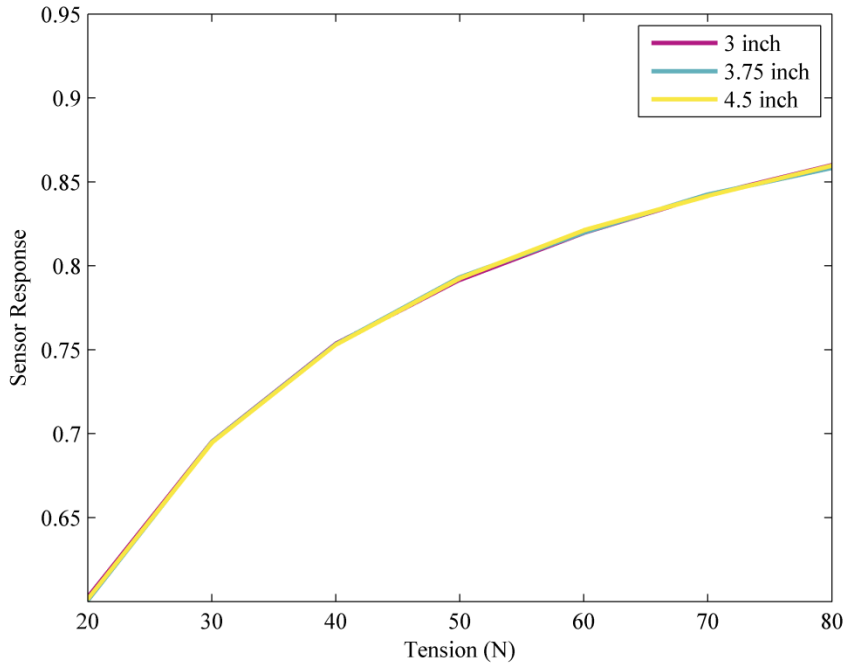

Figure 4-42: Simulated response of the sensor for three different free lengths

An experiment was conducted to verify the simulation. Three attachment plates, similar to the one shown in Figure 4-23, were designed for the three lengths. The mean of ten tests conducted at different tensions are shown in Figure 4-43. Unlike the simulated results, experimental sensor response show monotonic increase with increase in length.

In order to explain the variation in the sensor response due to change in length, the theoretical model was further improved to take into account the increase in tension due to transverse force applied by the sensor. The change in tension in the string was modeled using equation (4.27), where K_T is a gain dependent on the material properties of the string and $u(x_2)$ is the displacement of the string at the point of contact of the middle

bump of the sensor, as shown in Figure 4-4. This updated estimate of tension was used when calculating the expected values of the compressions using equation (4.6) at each z value.

$$\Delta T = K_T\, u(x_2) \tag{4.27}$$

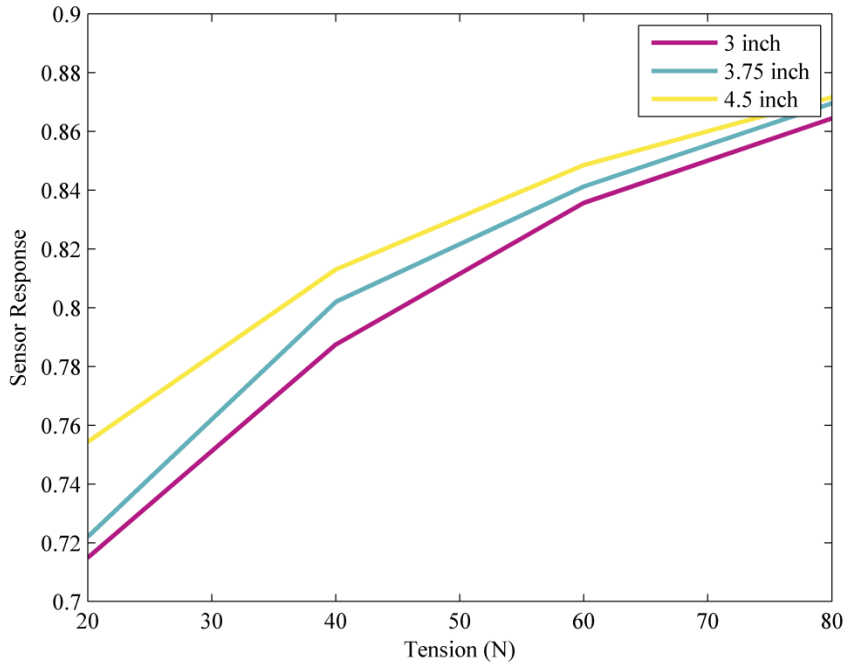

Figure 4-43: Experimental response of the sensor for three different free lengths

The simulated response of the sensor using the improved model for a K_T of $6\ \mathrm{N/mm}$, shown in Figure 4-44, agrees with the experimentally observed responses shown in Figure 4-43.

The effect of the length on the sensor response could potentially limit the sensor's applications when the value of K_T is unknown. However in situations when K_T is small, i.e. when the change in tension due to the transverse force applied by the tension is small, or when the value of K_T can be estimated, the sensor can still be utilized.

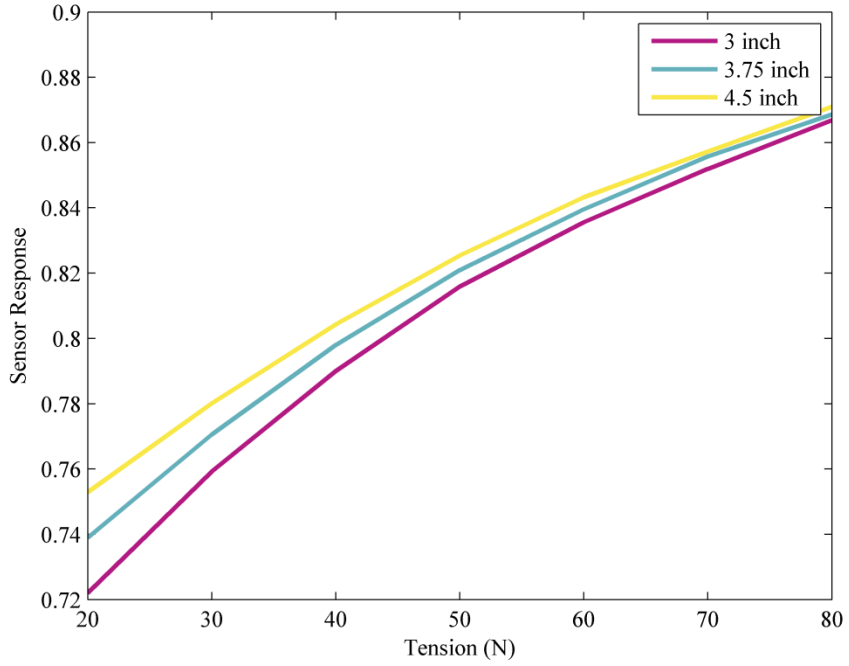

Figure 4-44: Simulated response of the sensor for different free lengths with an improved model

4.7.2 Location of contact

The effect of position of contact of the sensor along the string on the sensor response was analyzed by simulating the sensor response at 5 positions along the length of the string spanning a length equal to 20 % of the string length. The simulation was conducted using the improved model described in section 4.7.1 which takes into account the change in tension due to pushing. Figure 4-45 shows the simulate response for string of length 3 inches.

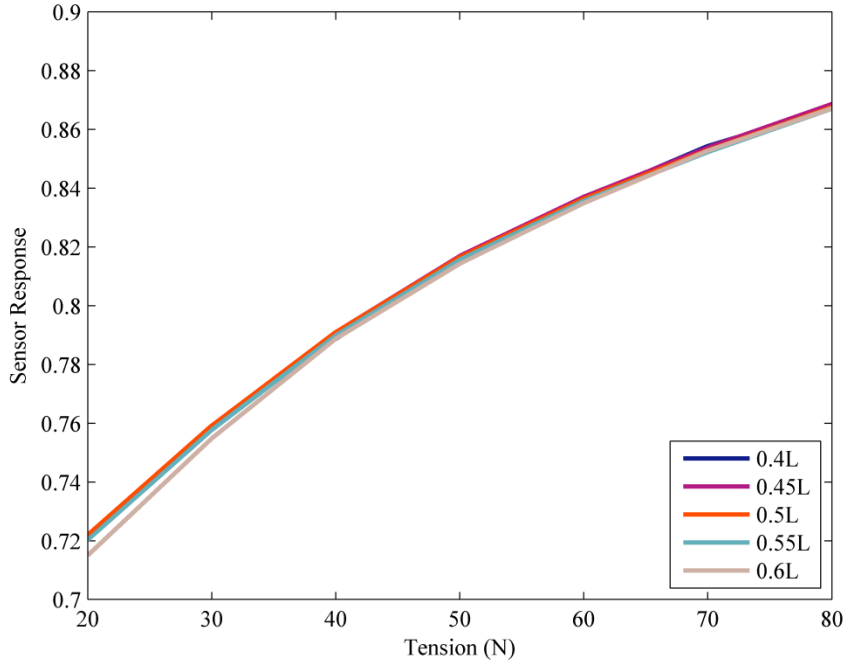

Figure 4-45: Simulate response for string of length 3” at five contact locations

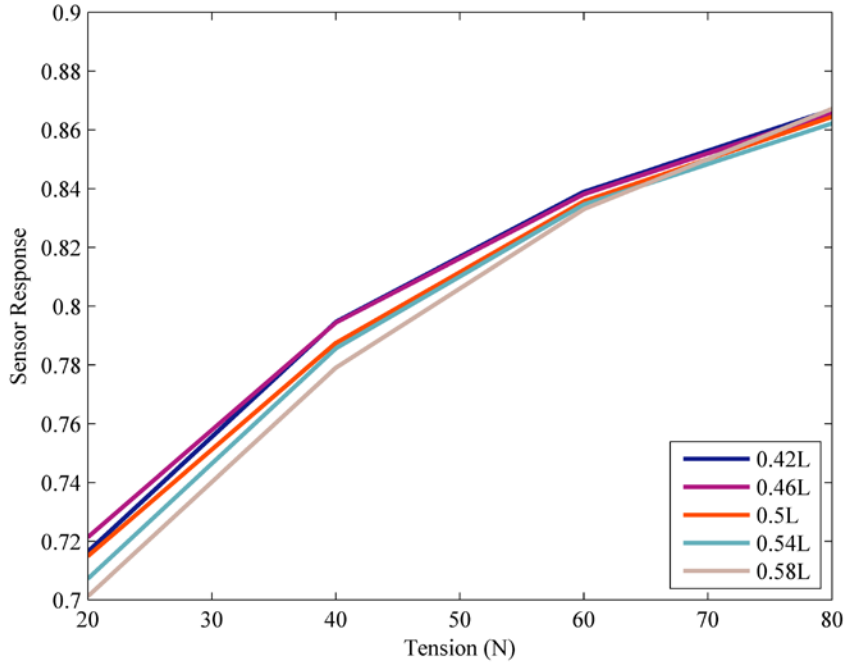

Figure 4-46: Experimental response for string of length 3” at five contact locations

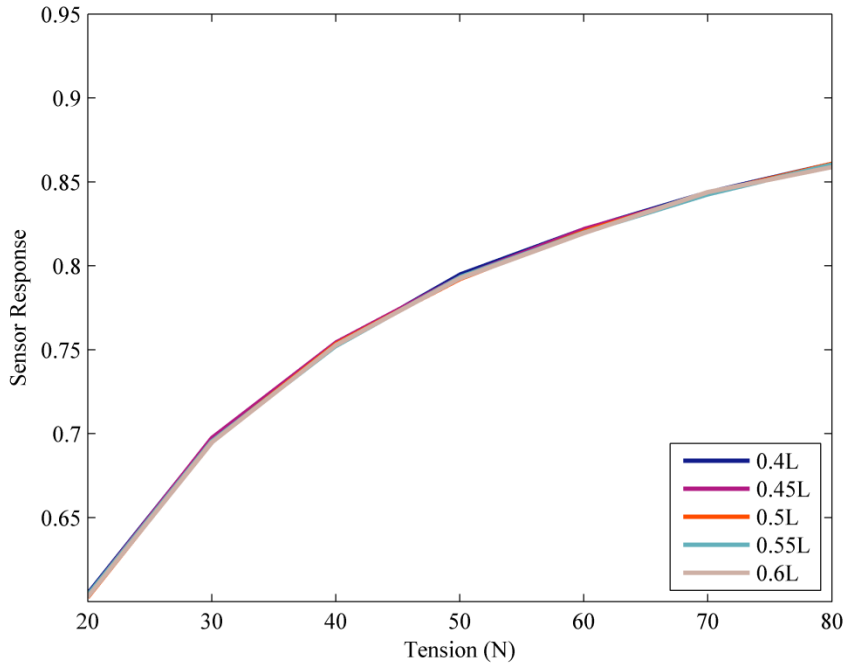

Figure 4-47: Simulated response for string of length 3" at five contact locations with $K_T = 0$

An experiment was conducted to verify the simulation. The mean of ten tests conducted at different tensions for five different contact locations are shown in Figure 4-46. Both experimental and theoretical response show a slight effect of position, however it is less pronounced as compared to length. This effect is again completely eliminated, as shown in Figure 4-47, if K_T is assumed to be zero.

4.8 DISCUSSION

The multi-probe sensor based on magnetic sensing principle addressed the shortcomings of the previously proposed sensors. It was experimentally demonstrated that the sensor could measure the tension in a string with a resolution better than 10 N for tensions values up to 80 N under controlled orientation.

The sensor was also able to measure tensions values up to 100 N in a handheld setting; however the resolution based on single test was worse than 10 N. It was established that the individual handheld tests could be considered as independent tests and a mean of

several handheld tests can be taken to estimate tension with a resolution of 10 N. It was further demonstrated that the standard deviation of the individual tests depends upon the experience of the user with the sensor technology.

A sensitivity analysis was then conducted to determine the effects of change in length and contact position on the sensor response. It was found that though the initial modeling suggested that the sensor response was independent of these two factors, they do affect the sensor response because of the change in tension that occurs due to the application of transverse force.

CHAPTER 5

OTHER POTENTIAL APPLICATIONS OF THE MULTI-PROBE MAGNETIC SENSOR

During the course of this dissertation, the multi-probe magnetic sensor developed in chapter 4 was also used for measuring properties other than tension in the string. This chapter discusses two such properties. A model for measuring a combined effect of elasticity and stiffness is presented in the first section. It is then shown that with a suitable reconfiguration, the sensor can be enabled to measure just the elasticity of the material and experimental results are presented. In the second section, it is shown that the same sensor can used for non-invasively measuring pressure inside a compartment, hence making it a viable sensor for diagnosis of compartment syndrome.

5.1 MODEL FOR MEASURING THE COMBINED EFFECT OF ELASTICITY AND TENSION

A homogeneous elastic material taut along x-axis under tension, T, is shown in Figure 5-1(a). When a transverse point force, F, is applied to the material, the material will deform as shown in Figure 5-1(b).

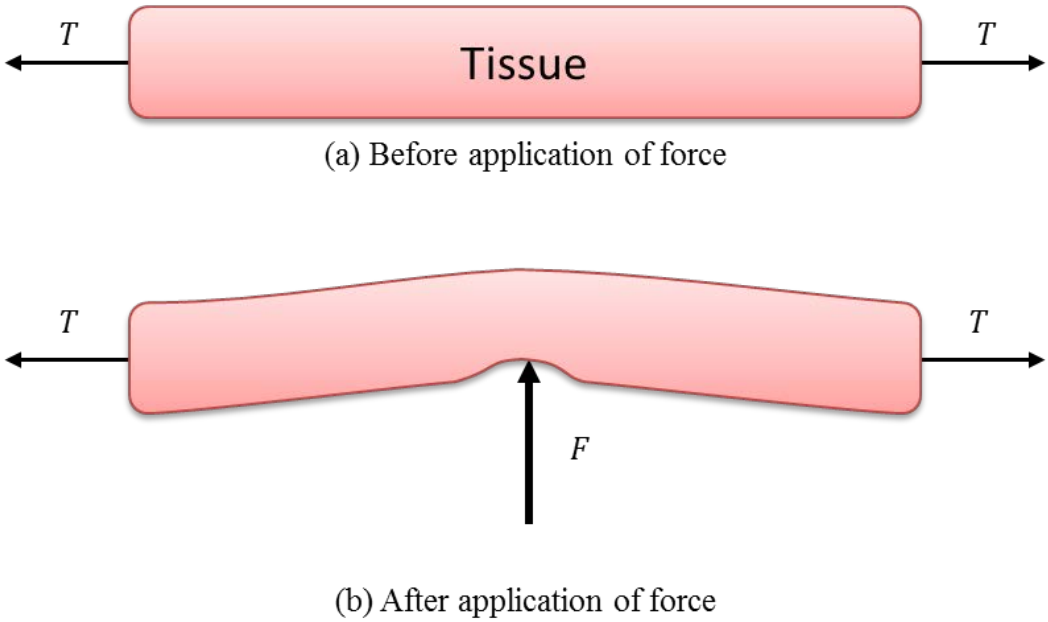

Figure 5-1: A homogenous elastic material under tension (a) with no force applied (b) with a point load applied

The total deformation in the material can be modeled as a combination of the buckling of the material due to boundary condition (tension) and the local deformation caused in the material due to its elasticity. The displacement due to the buckling of the material under tension can be modeled by modeling the material as an inelastic string, while the effect of local deformation can be modeled using a spring of stiffness k_t. Since the total deformation is the sum of both these deformations, the homogeneous elastic material can be modeled as a combination of these two elements as shown in Figure 5-2.

Figure 5-2: Model of the homogeneous model under a single transverse force

Figure 5-3 shows a schematic of the multi-probe magnetic sensor before and after being pushed against the material.

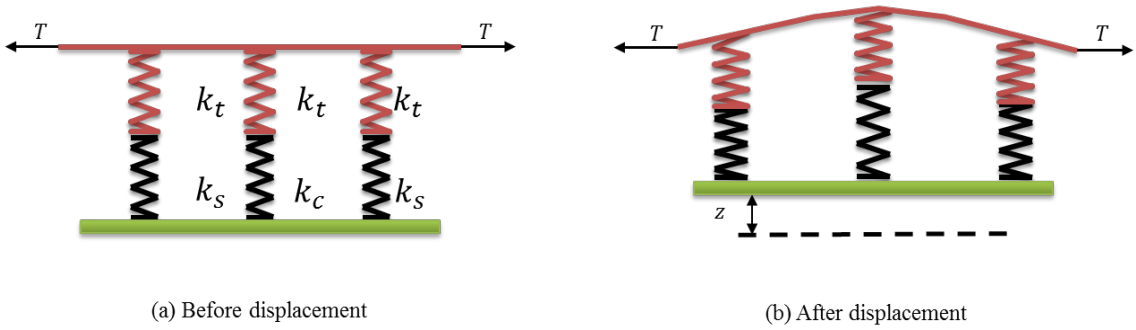

(a) Before displacement

(b) After displacement

Figure 5-3: Schematic of the multi-probe magnetic sensor before and after being pushed against the material

The displacement of three points on the inelastic string under the action of three point loads is still given by equation (3.6), which, for the sake of continuity, has been presented again as equation (5.1).

$$U = A_1(l, X_2, T) \times F \tag{5.1}$$

where,

$$A_1(l, x_2, T) = \frac{1}{T}\begin{bmatrix} \frac{(l-(x_2-d))(x_2-d)}{l} & \frac{(l-x_2)(x_2-d)}{l} & \frac{(l-(x_2+d))(x_2-d)}{l} \\ \frac{(l-x_2)(x_2-d)}{l} & \frac{(l-x_2)x_2}{l} & \frac{(l-(x_2+d))x_2}{l} \\ \frac{(l-(x_2+d))(x_2-d)}{l} & \frac{(l-(x_2+d))x_2}{l} & \frac{(l-(x_2+d))(x_2+d)}{l} \end{bmatrix} \tag{5.2}$$

Assuming that the local deformations at three points are independent of each other, the compression, ΔV, of the equivalent tissue spring of stiffness k_t at each of the locations is given by equation (5.3).

$$\Delta V = K_t^{-1} F \tag{5.3a}$$

where,

$$K_t = \begin{bmatrix} k_t & 0 & 0 \\ 0 & k_t & 0 \\ 0 & 0 & k_t \end{bmatrix} \tag{5.3b}$$

Also, the compressions, ΔY, in the three springs of the sensor are given by equation (5.4).

$$\Delta Y = K_s^{-1} F \tag{5.4a}$$

where,

$$K_s = \begin{bmatrix} k_s & 0 & 0 \\ 0 & k_c & 0 \\ 0 & 0 & k_s \end{bmatrix} \tag{5.4b}$$

Referring to Figure 5-3(b), under a normal contact assumption (equal displacements of the base of the three bumps) the compressions in the springs of the sensor, the compressions in equivalent tissue springs and the displacement of the inelastic string follows a relationship given by equation (5.5), where Z is the displacement of the base of three bump assemblies and for normal contact is given by equation (5.6).

$$U + \Delta V + \Delta Y = Z \tag{5.5}$$

$$Z = \begin{bmatrix} z \\ z \\ z \end{bmatrix} \tag{5.6}$$

A relationship between F and ΔY, given by equation (5.7), can be established by substituting equations (5.3), (5.4) and (5.5) in equation (5.1).

$$(K_s^{-1} + K_t^{-1} + A_1)\,\mathrm{F} = Z \tag{5.7}$$

Equation (5.7) can be solved to obtain the displacements of the three pistons and a ratio similar to one given in equation (3.13) can be constructed. For the model under consideration, this ratio is given by equation (5.8).

$$R = \frac{F_2}{(\mathrm{F}_1 + \mathrm{F}_3)/2} = \left(\frac{k_s}{k_c}\right)\left(\frac{k_s + k_t}{k_c + k_t}\right)\left(\frac{2T}{\left(2T + \left(\frac{k_c k_t}{k_c + k_t}\right) d\right)}\right) \tag{5.8}$$

This ratio consists of a product of two terms; the first term corresponds to the effect of the tissue elasticity, while the second term corresponds to effect of boundary conditions (tension). The sensor can be reconfigured to measure each term with a minimal influence of the other term.

5.1.1 Measurement of Tension

If the spring constants of the sensor are chosen such that, $k_s = k_c \ll k_t$, i.e. the side and the center spring constants are equal and the tissue material is much stiffer than the springs of the sensor then the ratio described in the equation (5.8) reduces to equation (5.9) which is the same as one expressed by equation (4.9) and has been discussed in detail in Chapter 4.

$$R = \left(\frac{2T}{2T + k_c\, d}\right) \tag{5.9}$$

5.1.2 Measurement of tissue stiffness

The knowledge of material properties for soft materials is vital for many applications including but not limited to fields of robotics and medical treatment. The knowledge becomes especially important in biomedical applications [40-51]. For instance it can be used for reliable diagnosis by palpation of the patient's tissue [44], for diagnosing breast cancers[52], to provide a tactile perception during minimally invasive surgery to distinguish between healthy and diseased tissues [43, 53], or for teleoperation [54].

If the tension in the string is very large then the second term of the product in the equation (5.8) will tend towards the unity and the ratio can be reduced to equation (5.10), which can used to estimate the stiffness of the soft materials.

$$R = \left(\frac{k_s}{k_c}\right)\left(\frac{k_s + k_t}{k_c + k_t}\right) \tag{5.10}$$

To evaluate the correctness of the equation (5.10), springs of different stiffness were procured from Lee Springs Inc. The sensor was configured with three distinct side and center spring combinations, listed in Table 5-1.

Table 5-1: Spring constants of side and center springs for different sensor configurations

Config. #	k_s (N/mm)	k_c (N/mm)	$r = k_c/k_s$
1	0.28	0.84	3.00
2	0.84	1.96	2.33
3	0.28	1.96	7.00

The sensor was tested by pushing it against sorbothane rubber specimens (Part No. 8450K3, McMaster-Carr) of hardness varying from Shore 30OO to Shore 80A. The Young's moduli of the target rubber specimens used are listed in Table 5-2 [46]. The target specimens have Young's modulus ranging from 0.14 MPa to 8.68 MPa.

Table 5-2: Young's Moduli of the sorbothane rubber specimens

Shore Scale	Young's Modulus (MPa)
30OO	0.14
30A	0.87
40A	1.54
50A	2.18
70A	5.48
80A	8.68

During experimentation, the sensor was mounted on a translation stage to prevent oblique contact. The rubber samples were mounted on an aluminum back plate fixed in front of the sensor using double sided tape, this can be considered as an equivalent of infinite tension as the aluminum plate would not allow any macro deformation, hence U, defined by equation (5.1), would be zero.

The translation stage was then moved forward till the average of forces experienced by the side bumps exceeded 1 N. Figure 5-4 shows a photograph of the experimental setup. Each rubber specimen was tested five times with each sensor configuration to evaluate the repeatability of the reading.

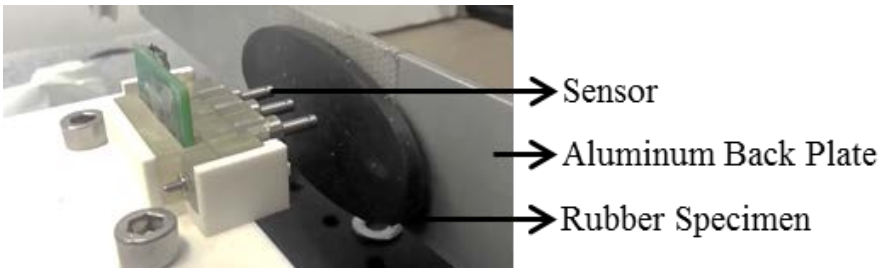

Figure 5-4: Photograph of experimental setup

Sample readouts for three different rubbers (30A, 40A and 80A) for the second sensor configuration (as shown in Table 5-1) are shown in Figure 5-5. As predicted by the equation (5.10), the plots between side and center forces are linear.

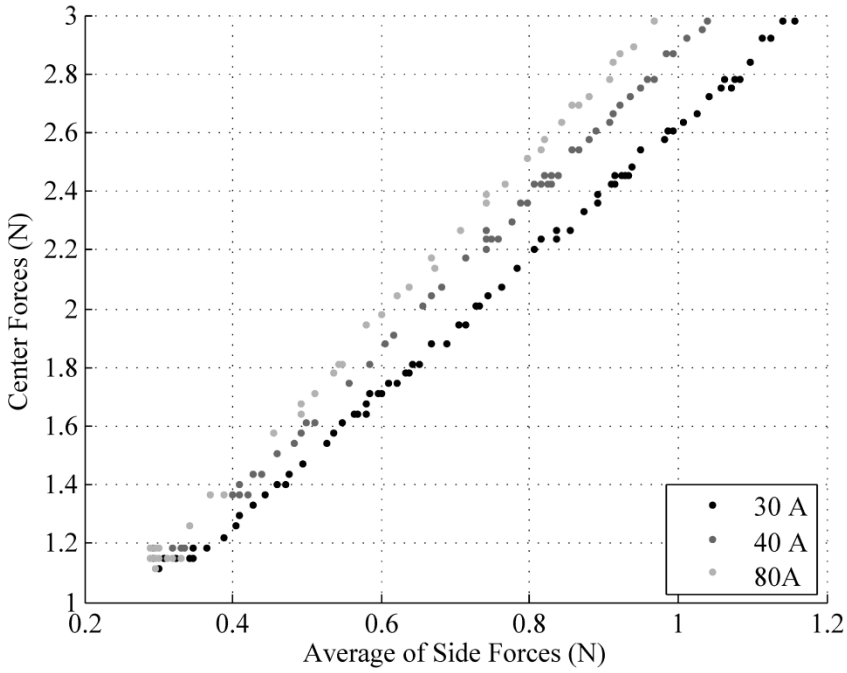

Figure 5-5: Sample readouts for different rubbers

An ordinary least square line (OLS) was then fit to this data and the slope of the line was calculated. The sensor response ($m(k_t)$), given by equation (5.11), was calculated by normalizing the slope value obtained by the OLS fit when the sensor was pushed against an aluminum plate ($k_t \to \infty$), so as to ensure that the sensor responses of all three configurations are upper bounded by unity.

$$m(k_t) = \left(\frac{k_s + k_t}{k_c + k_t}\right) \tag{5.11}$$

The sensor responses for the three configurations (listed in Table 5-1) for rubbers listed in Table 5-2 are shown in Figure 5-6 with the solid line representing the mean of the five responses and the error bars representing the range of response.

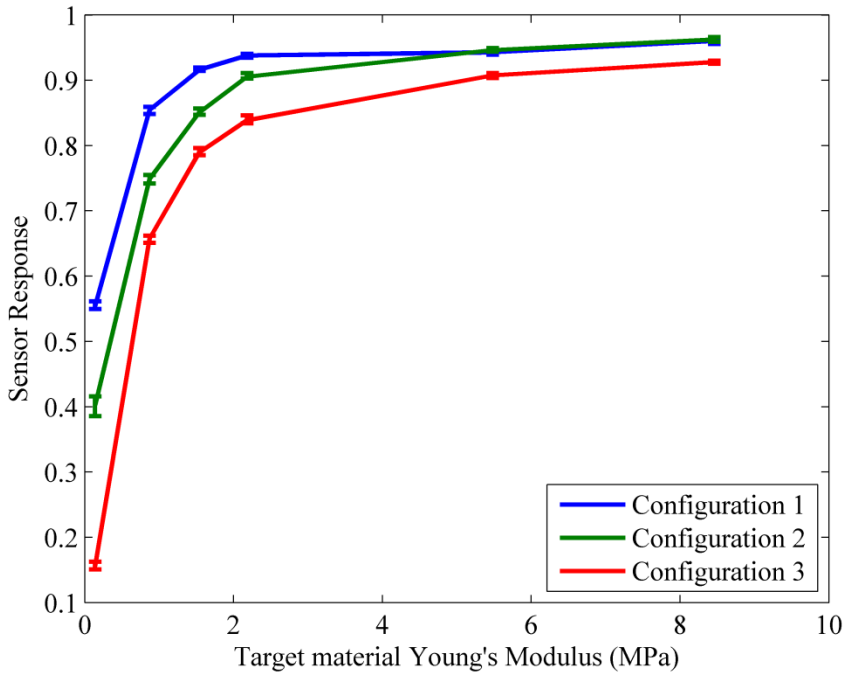

Figure 5-6: Experimental response of the sensor

The resolution of the sensor varies with the value of the target material's Young's modulus. However, the sensor response was found to be repeatable with the standard deviations for the three sensor configurations over repeated tests being 0.0032, 0.0054 and 0.0035 respectively. For a level of confidence of 95%, the expanded uncertainty (U) [39] for any particular range of Young's modulus can be calculated and is defined by equation (5.12).

$$U = 2 \times 1.96 \times \sigma \times \frac{\Delta E}{\Delta R} \tag{5.12}$$

where ΔE and ΔR are the changes in Young's modulus and mean sensor response in the range of interest respectively.

Using equation (5.12), for rubber of Young's modulus between 0.14 MPa – 0.87 MPa, the measurement uncertainties of the three sensor configurations are 0.03 MPa, 0.04 MPa and 0.02 MPa respectively, while between 0.87 MPa – 1.54 MPa, the measurement uncertainties of the three sensor configurations are 0.14 MPa, 0.14 MPa and 0.07 MPa respectively.

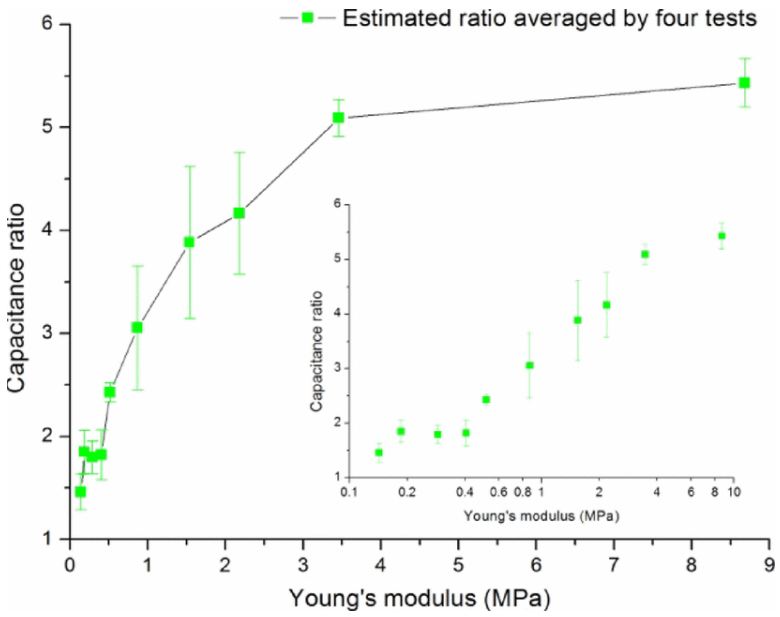

Figure 5-7: Estimated capacitance ratio versus Young's modulus of the rubber sample. Inserts: data plotted in lin-log scale.

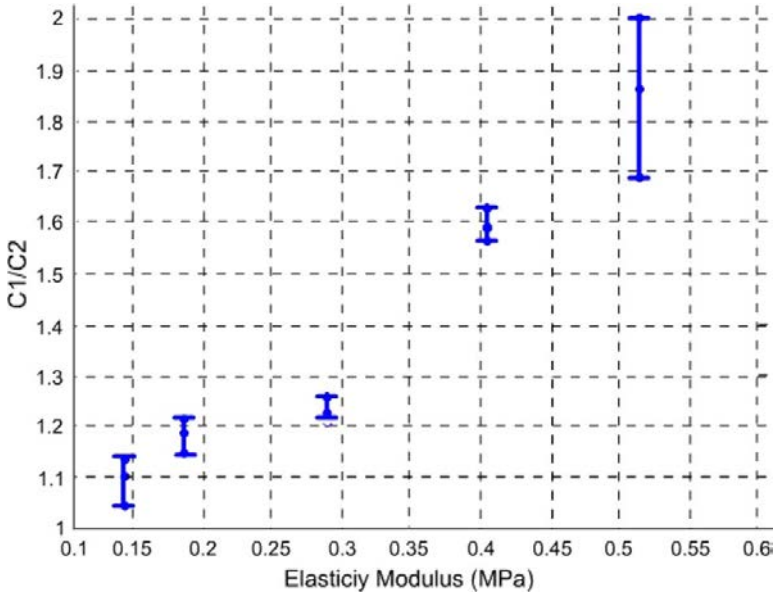

Figure 5-8: Ratio of capacitive change versus Young's modulus for flexible tactile sensors

A similar elasticity sensor was presented earlier by Peng et al . , Figure 5-7 and Figure 5-8 shows the results from two of their sensors. Comparing Figure 5-6 with these two, it can be clearly seen that the magnetic sensor developed in this dissertation has much better repeatability as compared to the sensors developed by Peng et al. The resolution of measurement for the flexible tactile sensor was reported as 0.1 MPa in the range of 0.1-0.5 MPa [45], which is approximately five times worse than the resolution of 0.02 MPa for the magnetic sensor presented in this section. However, the results of Figure 5-7 were obtained in a handheld mode of operation where significant orientation errors could have played a role in increasing variability of the sensor response.

5.2 COMPARTMENT PRESSURE MEASUREMENT

The diagnosis of compartment syndrome (CS) is difficult due to the limited number of measurement options available [55]. Compartment syndrome (CS) is a condition in which the intramuscular pressure (IMP) in a muscle compartment becomes elevated significantly above the arterial pressure, which leads to reduced flow to the muscle and nervous tissue. Without treatment, compartment syndrome can lead to paralysis, loss of

limb, or death. A fasciotomy, a surgical process in which the physician cuts open the skin and fascia covering the affected compartment, is typically recommended when the tissue perfusion pressure — mean arterial pressure minus IMP [56] — falls below 30-40 mmHg [57]. Fasciotomy also poses risk factors of development of chronic venous insufficiency (CVI) [58] and could potentially lead to physiological abnormalities of the lower extremity venous system [59]. Since fasciotomy has high morbidity and high rate of complications [59] and can lead to infections [60], a method of accurate measurement of IMP could be helpful in diagnosing CS. However a direct and accurate measurement of the IMP via catheter is invasive [55] and poses a potential risk of complications and infection to the patient.

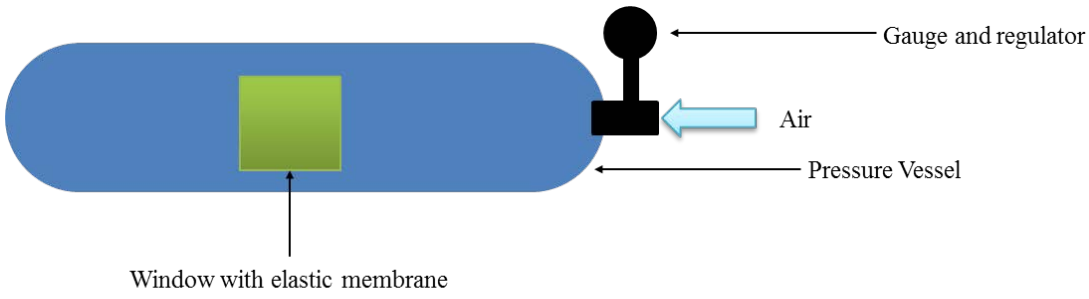

(a) Schematic

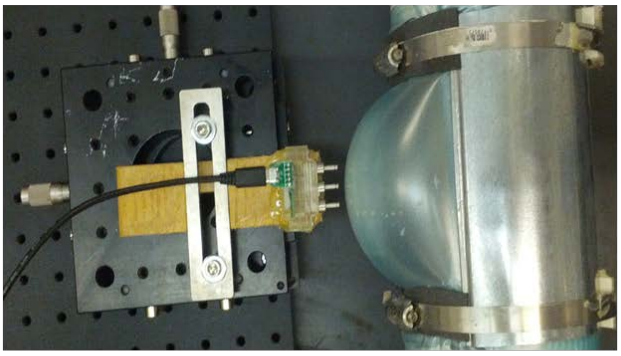

(b) Photograph

Figure 5-9: Pressure vessel used for measuring compartment pressure

Flegel et al. [61] presented a theoretical formulation to allow the use of the multi-probe magnetic sensor for measuring pressure in a compartment. It was shown that if the

magnetic sensor is configured with different side and center springs, then the pressure (P) in the compartment follows the relationship given by equation (5.13), where R_f is the ratio of force experienced by side springs to that experienced by center spring and is given by equation (5.14).

$$P \propto R_f - 1 \tag{5.13}$$

$$R_f = \left(\frac{(F_1 + F_3)/2}{F_2}\right) \tag{5.14}$$

A setup shown in Figure 5-9 was realized to evaluate the sensor's performance with regards to measuring pressure in a compartment. For a magnetic sensor with center spring stiffness of 1.96 N/mm and side spring stiffness of 0.88 N/mm, the experimental results obtained for different pressures are shown in Figure 5-10. As predicted by equation (5.13), the pressure was found to be proportional to the force ratio. The resolution of sensor was found to be 0.1 psi in the range of 0.75 psi to 2.5 psi (approx. 40-130 mmHg.)

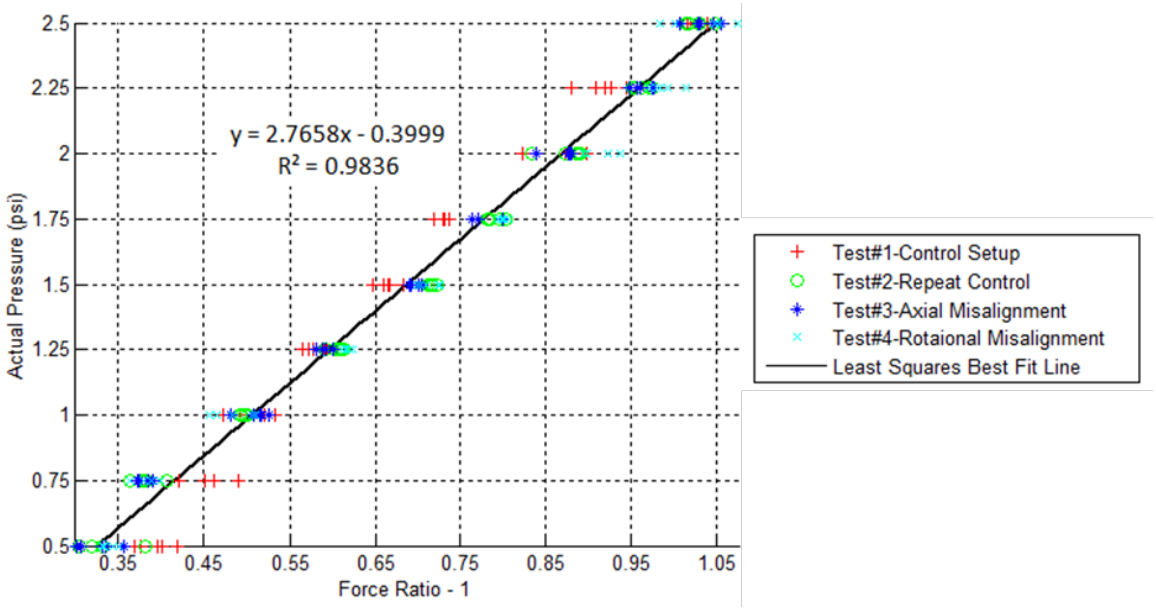

Figure 5-10: Linear correlation between pressure and sensor response

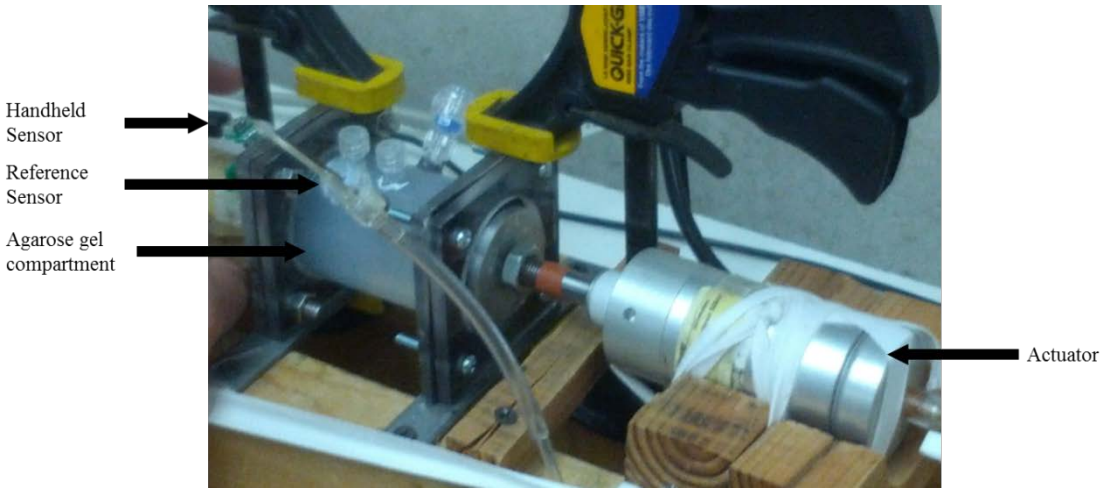

Figure 5-11: Experimental setup for measuring pressure with agarose gel compartment

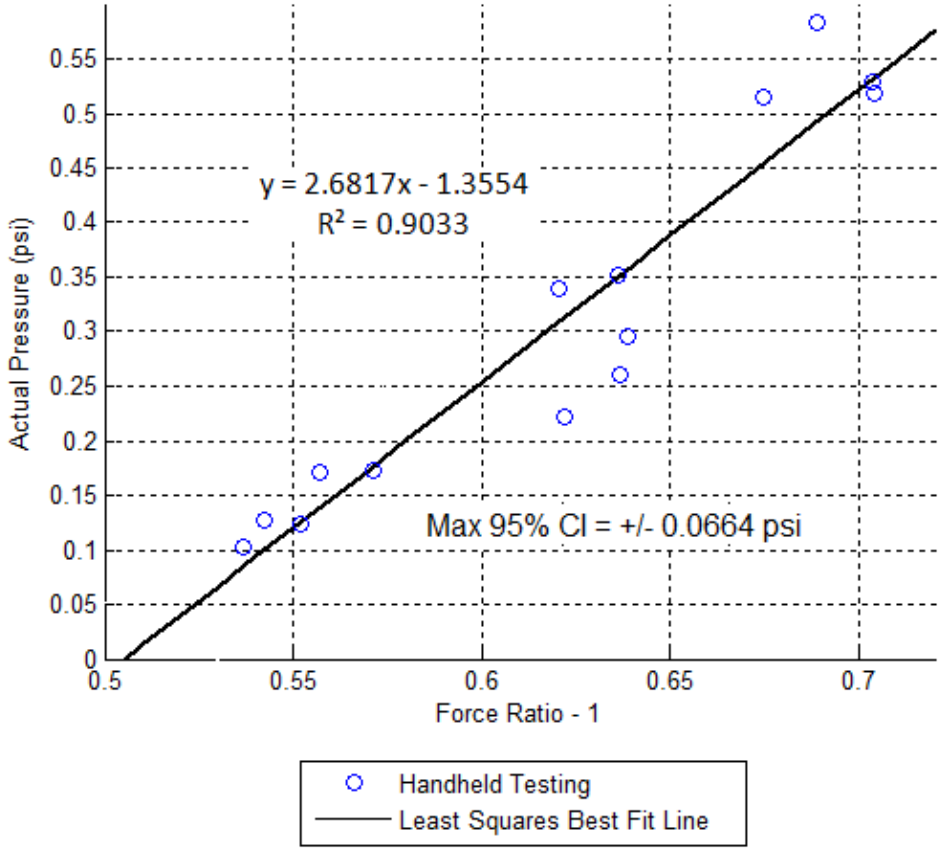

Figure 5-12: Comparison of catheter and magnetic sensor for pressure magnetic

The performance of the sensor was also evaluated during handheld operation and was compared to a catheter based commercial sensor from Twin Star medical, Minneapolis

MN USA. Figure 5-11 shows a photograph of the experimental setup. It consists of a 1.0% agarose gel contained in a compartment. A piston was used to apply pressure on one of the walls of the gel compartment. A catheter based reference sensor was inserted in the gel compartment and the magnetic sensor was pushed against the other wall of the compartment to non-invasively measure pressure in the compartment.

Figure 5-12 shows the response of the magnetic sensor (on x axis) plotted against the readout of the catheter sensor (on y axis.) The plot shows a good agreement between the readouts of the two sensors, making the sensor developed as a part of this thesis a non-invasive alternate to the catheter sensor.

CHAPTER 6

CONCLUSIONS

Balancing tension in soft tissues during various orthopedic procedures is crucial for good soft tissue healing, restoration of overall limb function in the patient, and a long lasting implant. However, there do not exist any easy to use devices which can measure tension in soft tissues without requiring significant tissue handling. This dissertation focused on developing such a handheld device which can non-invasively measure tension in ligaments by simply pushing against them.

The dissertation presented two main estimation methodologies - a single probe estimation technique and a multi probe estimation technique. A capacitive sensor based measurement was developed for the single probe sensor and its performance was demonstrated. Multi-probe sensors were implemented using both capacitive and magnetic sensing principles. Extensive characterization of the magnetic sensor was performed to evaluate the performance of the sensor both with controlled orientations and with handheld operation. The viability of the sensor to measure tension in biological tissues was also demonstrated using tendons extracted from a turkey leg. It was demonstrated that the developed sensors can successfully measure tensions values up to 100 N in both synthetic short strings and soft tissues.

Several other alternate applications of the multi-probe magnetic sensor for medical diagnosis were presented. The first alternate application for the sensor was measurement of tissue elasticity for diagnostics of tissue health. The resolution of the sensor developed

in this dissertation was found to be 0.02 MPa in the range 0.14 MPa – 0.87 MPa. This is a substantial improvement over the resolution of 0.1 MPa in the range of 0.1 – 0.5 MPa reported in the literature. In fact the resolution of the sensor developed in this dissertation was found to be better than the resolution reported in literature, even with the developed sensor having four times as much range.

A second alternate application for the sensor was diagnosis of compartment syndrome by non-invasively measuring pressure inside a muscle compartment. The sensor was found to have a 0.1 psi resolution for pressure between 0.75-2.5 psi. The readings of the handheld sensor were found to be in good agreement with a commercially available catheter sensor making it a viable non-invasive sensor for measuring pressures in compartments.

In conclusion, a non-invasive handheld sensor for performing multiple medical diagnoses was developed and the performance of the sensor was evaluated with synthetic and biological materials.

BIBLIOGRAPHY

[1] M. Matsueda, T. R. Gengerke, M. Murphy, W. D. Lew and R. B. Gustilo, "Soft tissue release in total knee arthroplasty: cadaver study using knees without deformities," *Clin. Orthop.,* vol. 366, pp. 264, 1999.

[2] D. D. D'Lima, S. Patil, N. Steklov and C. W. Colwell Jr, "An Abjs Best Paper," *Clin. Orthop.,* vol. 463, pp. 208, 2007.

[3] D. D. D'Lima, S. Patil, N. Steklov and C. W. Colwell, "The 2011 ABJS Nicolas Andry Award:'Lab'-in-a-Knee: In Vivo Knee Forces, Kinematics, and Contact Analysis," *Clinical Orthopaedics and Related Research®,* pp. 1-18, .

[4] D. H. Lee, J. H. Park, D. I. Song, D. Padhy, W. K. Jeong and S. B. Han, "Accuracy of soft tissue balancing in TKA: comparison between navigation-assisted gap balancing and conventional measured resection," *Knee Surgery, Sports Traumatology, Arthroscopy,* vol. 18, pp. 381-387, 2010.

[5] D. Longjohn and L. D. Dorr, "Soft tissue balance of the hip," *J. Arthroplasty,* vol. 13, pp. 97-100, 1, 1998.

[6] M. Arnold, N. Verdonschot and A. van Kampen, "ACL graft can replicate the normal ligament's tension curve," *Knee Surgery, Sports Traumatology, Arthroscopy,* vol. 13, pp. 625-631, 11/11, 2005.

[7] K. Hayes, M. Callanan, J. Walton, A. Paxinos and G. A. Murrell, "Shoulder instability: management and rehabilitation," *J. Orthop. Sports Phys. Ther.,* vol. 32, pp. 497-509, Oct, 2002.

[8] A. K. Franta, T. R. Lenters, D. Mounce, B. Neradilek and F. A. Matsen III, "The complex characteristics of 282 unsatisfactory shoulder arthroplasties," *Journal of Shoulder and Elbow Surgery,* vol. 16, pp. 555-562, 2007.

[9] K. Steven, O. Kevin, L. Edmund, M. Fionna and H. Michael, "Projections of primary and revision hip and knee arthroplasty in the United States from 2005 to 2030," *The Journal of Bone and Joint Surgery (American),* vol. 89, pp. 780-785, 2007.

[10] F. M. Griffin, J. N. Insall and G. R. Scuderi, "Accuracy of soft tissue balancing in total knee arthroplasty," *J. Arthroplasty,* vol. 15, pp. 970-973, 12, 2000.

[11] H. Bäthis, L. Perlick, M. Tingart, C. Lüring, C. Perlick and J. Grifka, "Radiological results of image-based and non-image-based computer-assisted total knee arthroplasty," *Int. Orthop.,* vol. 28, pp. 87-90, 2004.

[12] J. Mahaluxmivala, M. Bankes, P. Nicolai, C. Aldam and P. Allen, "The effect of surgeon experience on component positioning in 673 Press Fit Condylar posterior cruciate-sacrificing total knee arthroplasties," *J. Arthroplasty,* vol. 16, pp. 635-640, 2001.

[13] M. Sparmann, B. Wolke, H. Czupalla, D. Banzer and A. Zink, "Positioning of total knee arthroplasty with and without navigation support A PROSPECTIVE,

RANDOMISED STUDY," *Journal of Bone & Joint Surgery, British Volume,* vol. 85, pp. 830-835, 2003.

[14] J. B. Mason, T. K. Fehring, R. Estok, D. Banel and K. Fahrbach, "Meta-analysis of alignment outcomes in computer-assisted total knee arthroplasty surgery," *J. Arthroplasty,* vol. 22, pp. 1097-1106, 2007.

[15] R. C. Wasielewski, D. D. Galat and R. D. Komistek, "An intraoperative pressure-measuring device used in total knee arthroplasties and its kinematics correlations," *Clin. Orthop.,* vol. 427, pp. 171, 2004.

[16] C. B. Frank and D. W. Jackson, "The science of reconstruction of the anterior cruciate ligament." *The Journal of Bone and Joint Surgery.American Volume,* vol. 79, pp. 1556, 1997.

[17] C. S. Ahmad, V. M. Wang, M. T. Sugalski, W. N. Levine and L. U. Bigliani, "Biomechanics of shoulder capsulorrhaphy procedures," *Journal of Shoulder and Elbow Surgery,* vol. 14, pp. S12-S18, 2005.

[18] S. L. Brenneke, J. Reid, R. P. Ching and D. L. Wheeler, "Glenohumeral kinematics and capsulo-ligamentous strain resulting from laxity exams," *Clin. Biomech.,* vol. 15, pp. 735-742, 2000.

[19] P. A. Caprise, "Open and arthroscopic treatment of multidirectional instability of the shoulder," *Arthroscopy: The Journal of Arthroscopic & Related Surgery,* vol. 22, pp. 1126-1131, 2006.

[20] K. Krøner, T. Lind and J. Jensen, "The epidemiology of shoulder dislocations," *Arch. Orthop. Trauma Surg.,* vol. 108, pp. 288-290, 1989.

[21] B. Fleming, B. Beynnon, H. Tohyama, R. Johnson, C. Nichols, P. Renström and M. Pope, "Determination of a zero strain reference for the anteromedial band of the anterior cruciate ligament," *Journal of Orthopaedic Research,* vol. 12, pp. 789-795, 1994.

[22] B. C. Fleming and B. D. Beynnon, "In vivo measurement of ligament/tendon strains and forces: a review," *Ann. Biomed. Eng.,* vol. 32, pp. 318-328, 2004.

[23] T. Lyyra, I. Kiviranta, U. Väätäinen, H. J. Helminen and J. S. Jurvelin, "In vivo characterization of indentation stiffness of articular cartilage in the normal human knee," *J. Biomed. Mater. Res.,* vol. 48, pp. 482-487, 1999.

[24] S. Salmons, "The 8th international conference on medical and biological engineering–meeting report," *Bio Med Eng,* vol. 4, pp. 467-474, 1969.

[25] D. Barry and A. Ahmed, "Design and performance of a modified buckle transducer for the measurement of ligament tension," *J. Biomech. Eng.,* vol. 108, pp. 149, 1986.

[26] T. D. Brown, L. Sigal, G. O. Njus, N. M. Njus, R. J. Singerman and R. A. Brand, "Dynamic performance characteristics of the liquid metal strain gage," *J. Biomech.,* vol. 19, pp. 165-173, 1986.

[27] D. Glos, D. Butler, E. Grood and M. Levy, "In vitro evaluation of an implantable force transducer (IFT) in a patellar tendon model," *J. Biomech. Eng.*, vol. 115, pp. 335, 1993.

[28] B. Ravary, P. Pourcelot, C. Bortolussi, S. Konieczka and N. Crevier-Denoix, "Strain and force transducers used in human and veterinary tendon and ligament biomechanical studies," *Clin. Biomech.*, vol. 19, pp. 433-447, 2004.

[29] Mkandawire Chimba, Kristal Phyllis and Tencer Allan, "A technique for the measurement of tension in small ligaments," in *Musculoskeletal Models and Techniques*, C. T. Leondes, Ed. Boca Raton, Florida: CRC Press, 2000, .

[30] D. Glos, J. Holden, D. Butler and E. Grood, "Pressure vs deflected beam force measurement in the human patellar tendon," *Transactions of the 36th Orthopaedic Research Society*, vol. 15, pp. 490, 1990.

[31] A. Erdemir, S. J. Piazza and N. A. Sharkey, "Influence of loading rate and cable migration on fiberoptic measurement of tendon force," *J. Biomech.*, vol. 35, pp. 857-862, 2002.

[32] P. Kristal, A. Tencer, T. Trumble, E. North and D. Parvin, "A method for measuring tension in small ligaments: an application to the ligaments of the wrist carpus," *J. Biomech. Eng.*, vol. 115, pp. 218, 1993.

[33] L. Weaver, A. F. Tencer and T. E. Trumble, "Tensions in the palmar ligaments of the wrist. I. The normal wrist," *J. Hand Surg.*, vol. 19, pp. 464-474, 1994.

[34] H. Asano, T. Muneta and I. Sekiya, "Soft tissue tension in extension in total knee arthroplasty affects postoperative knee extension and stability," *Knee Surgery, Sports Traumatology, Arthroscopy*, vol. 16, pp. 999-1003, 2008.

[35] D. Mayman, C. Plaskos, D. Kendoff, G. Wernecke, A. D. Pearle and R. Laskin, "Ligament tension in the ACL-deficient knee: assessment of medial and lateral gaps," *Clinical Orthopaedics and Related Research*, vol. 467, pp. 1621-1628, 2009.

[36] I. Stakgold, *Boundary Value Problems of Mathematical Physics.* Philadelphia, PA: Society for Industrial and Applied Mathematics, 2000.

[37] D. J. Griffiths, *Introduction to Electrodynamics.* New Jersey: Prentice-Hall, 1999.

[38] B. H. McArdle, "Lines, models, and errors: regression in the field," *Limnol. Oceanogr.*, vol. 48, pp. 1363-1366, 2003.

[39] *NIST Reference on Constants, Units, and Uncertainty - Uncertainity of Meaurement Results* [Online]. Available: http://physics.nist.gov/cuu/Uncertainty/index.html.

[40] A. Samani, C. Luginbuhl and D. B. Plewes, "Magnetic resonance elastography technique for breast tissue in-vitro elasticity measurement," in *Biomedical Imaging, 2002. Proceedings. 2002 IEEE International Symposium on*, 2002, pp. 931-934.

[41] Junbo Li, Mingxi Wan, Ming Qian and Jingzhi Cheng, "Elasticity measurement of soft tissue using shear acoustic wave and real-time movement estimating based on PCA

neural network," in *Engineering in Medicine and Biology Society, 1998. Proceedings of the 20th Annual International Conference of the IEEE,* 1998, pp. 1395-1396 vol.3.

[42] D. Bridges, C. Randall and P. K. Hansma, "A new device for performing reference point indentation without a reference probe," *Rev. Sci. Instrum.,* vol. 83, pp. 044301, April 2012, 2012.

[43] P. Hansma, H. Yu, D. Schultz, A. Rodriguez, E. A. Yurtsev, J. Orr, S. Tang, J. Miller, J. Wallace, F. Zok, C. Li, R. Souza, A. Proctor, D. Brimer, X. Nogues-Solan, L. Mellbovsky, M. J. Pena, O. Diez-Ferrer, P. Mathews, C. Randall, A. Kuo, C. Chen, M. Peters, D. Kohn, J. Buckley, X. Li, L. Pruitt, A. Diez-Perez, T. Alliston, V. Weaver and J. Lotz, "The tissue diagnostic instrument," *Rev. Sci. Instrum.,* vol. 80, pp. 054303, May 2009, 2009.

[44] R. Aoyagi and T. Yoshida, "Frequency equations of an ultrasonic vibrator for the elastic sensor using a contact impedance method," *Japanese Journal of Applied Physics,* vol. 43, pp. 3204-3209, 2004.

[45] P. Peng and R. Rajamani, "Micro-tactile sensors for in vivo measurements of elasticity," in , D. Zhang, Ed. Springer New York, 2013, pp. 141-163.

[46] P. Peng and R. Rajamani, "Handheld Microtactile Sensor for Elasticity Measurement," *Sensors Journal, IEEE,* vol. 11, pp. 1935-1942, 2011.

[47] P. Peng, R. Rajamani and X. Yu, "Flexible micro-tactile sensor for normal and shear elasticity measurements," in *Solid-State Sensors, Actuators and Microsystems Conference (TRANSDUCERS), 2011 16th International,* 2011, pp. 1212-1215.

[48] P. Peng and R. Rajamani, "Capacitance ratio estimation on a novel MEMS tactile sensor for elasticity measurement," in *American Control Conference (ACC), 2011,* 2011, pp. 3459-3464.

[49] P. Peng, A. Sezen, R. Rajamani and A. Erdman, "Novel MEMS stiffness sensor for force and elasticity measurements," *Sensors and Actuators A: Physical,* vol. 158, pp. 10-17, 2010.

[50] P. Peng, R. Rajamani and A. G. Erdman, "Flexible Tactile Sensor for Tissue Elasticity Measurements," *J Microelectromech Syst,* vol. 18, pp. 1226-1233, 2009.

[51] P. Peng, A. S. Sezen, R. Rajamani and A. G. Erdman, "Novel MEMS stiffness sensor for in-vivo tissue characterization measurement," in *Engineering in Medicine and Biology Society, 2009. EMBC 2009. Annual International Conference of the IEEE,* 2009, pp. 6640-6643.

[52] J. Dargahi, S. Najarian, V. Mirjalili and B. Liu, "Modelling and testing of a sensor capable of determining the stiffness of biological tissues," *Electrical and Computer Engineering, Canadian Journal of,* vol. 32, pp. 45-51, 2007.

[53] G. Tholey, J. P. Desai and A. E. Castellanos, "Force feedback plays a significant role in minimally invasive surgery: results and analysis," *Ann. Surg.,* vol. 241, pp. 102, 2005.

[54] C. Bonomo, P. Brunetto, L. Fortuna, P. Giannone, S. Graziani and S. Strazzeri, "A Tactile Sensor for Biomedical Applications Based on IPMCs," *Sensors Journal, IEEE,* vol. 8, pp. 1486-1493, 2008.

[55] J. E. Lynch, J. S. Heyman and A. R. Hargens, "Ultrasonic device for the noninvasive diagnosis of compartment syndrome," *Physiol. Meas.,* vol. 25, pp. N1, 2004.

[56] R. M. Odland and A. H. Schmidt, "Compartment syndrome ultrafiltration catheters: report of a clinical pilot study of a novel method for managing patients at risk of compartment syndrome," *J. Orthop. Trauma,* vol. 25, pp. 358-365, 2011.

[57] C. Vaillancourt, I. Shrier, A. Vandal, M. Falk, M. Rossignol, A. Vernec and D. Somogyi, "Acute compartment syndrome: how long before muscle necrosis occurs?" *CJEM,* vol. 6, pp. 147-154, May, 2004.

[58] K. M. Bermudez, M. M. Knudson, N. A. Nelken, S. Shackleford and C. L. Dean, "Long-term results of lower-extremity venous injuries," *Archives of Surgery,* vol. 132, pp. 963, 1997.

[59] K. Bermudez, M. M. Knudson, D. Morabito and O. Kessel, "Fasciotomy, chronic venous insufficiency, and the calf muscle pump," *Archives of Surgery,* vol. 133, pp. 1356, 1998.

[60] G. Velmahos, D. Theodorou, D. Demetriades, L. Chan, T. Berne, J. Asensio, E. Cornwell III, H. Belzberg and B. Stewart, "Complications and nonclosure rates of fasciotomy for trauma and related risk factors," *World J. Surg.,* vol. 21, pp. 247-253, 1997.

[61] C. Flegel, K. Singal and R. Rajamani, "A handheld noninvasive sensing method for the measurement of compartment pressures ," in *ASME 2013 6th Annual Dynamic Systems and Control Conference, DSCC 2013*, 2013, .